NTNU

Norwegian University of
Science and Technology

Dynamic Response of Suspension Bridge with floating Towers

Sondre Halden

Department of Structural Engineering
Faculty of Engineering Science and Technology
NTNU- Norwegian University of Science and Technology

MASTER THESIS 2016

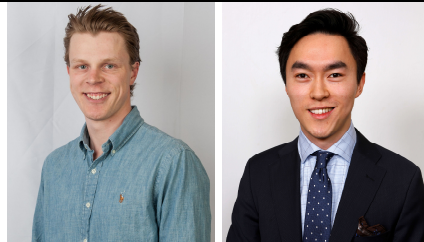| SUBJECT AREA:	DATE:	NO. OF PAGES:
Structural Dynamics	10.06.2016	151 (24+114+13)

TITLE:

Dynamic response of suspension bridge with floating towers

Dynamisk respons av hengebru med flytende tårn

BY:

Sondre Halden

Shun Wei Gong

SUMMARY:
The Norwegian Public Road Administration has been investigating the possibilities of crossing the fjords on the west coast of Norway for the coastal highway E39 project. For the 5 km wide Bjørnafjorden a floating three span suspension bridge with two pylons standing on tension leg platforms (TLP), is considered. A parametrized model of a floating multi-span TLP suspension bridge has been created, where the parameters have been given the planned geometry of the Bjørnafjorden bridge concept. A hydrodynamic analysis conducted on a FE-model of a pontoon where added mass, damping, restoring forces and the wave transfer function were obtained. Buffeting theory and aerodynamic derivatives were used to obtain the buffeting forces, stiffness and damping terms. A generalized method was developed to couple system matrices and forces from wind and waves in modal coordinates.

Modal-, response- and motion induced instability analyses, all accounting for hydrodynamic added mass, damping and restoring forces and aerodynamic damping and stiffness, have been conducted in the frequency domain. The environmental effects resulted in significantly lower eigenfrequencies. A response analysis was carried out for combinations of different stationary parameters for wind and waves. It was evident that wind governed the response in transversal- and waves for the vertical and rotational directions for modes with higher corresponding eigenfrequenciees. The most participating modes was the first mode in transversal direction and the first mode in vertical direction, obtained from the modal analysis, frequency response spectra and standard deviations. An aerodynamic motion induced instability limit was found to de 88 m/s at 1.5217 rad/s.

RESPONSIBLE TEACHER: Associate Professor Ole Øiseth

SUPERVISOR(S): Associate Professor Ole Øiseth, Phd. Candidate Yuwang Xu

CARRIED OUT AT: Department of Structural Engineering

Institutt for konstruksjonsteknikk
FAKULTET FOR INGENIØRVITENSKAP OG TEKNOLOGI
NTNU – Norges teknisk-naturvitenskapelige universitet

MASTEROPPGAVE 2016

for

Shun Wei Gong og Sondre Halden

Dynamisk respons av hengebru med flytende tårn

Dynamic response of suspension bridge with floating towers

I forbindelse med prosjektet ferjefri E39 har det blitt lansert et konsept for kryssing av Bjørnafjorden som består av en hengebru med tre spenn og to flytende tårn. De flytende tårnene settes på flytere som forankres til sjøbunnen ved hjelp av forankringsliner (TLP). Studentene skal ta utgangspunkt i det arbeidet som har blitt utført av TDA og Statens vegvesen

Oppgaven bør inneholde følgende temaer.
- Analyse av flyternes hydrodynamiske egenskaper i HydroD
- Etablering av en modell i programmet Abaqus der de hydrodynamiske effektene modelleres ved hjelp av fjærer, dempere og punktmasser.
- Analyse av statiske utbøyinger, egenfrekvenser og svingeformer.
- Kartlegging av den hydrodynamiske dempingens innflytelse på den totale dempingen av konstruksjonen.

Det legges vekt på at studenten må gjøre fornuftige forenklinger for å komme i mål med oppgaven

Besvarelsen organiseres i henhold til gjeldende retningslinjer.

Veileder(e): Ole Andre Øiseth, Yuwang Xu,

NTNU, 25.01.2015

Ole Andre Øiseth
faglærer

Sammendrag

Statens vegvesen utreder mulighetene for kryssing av fjordene på vestlandet i forbindelse med prosjektet Fergefri E39. For den 5 km brede Bjørnafjorden vurderes en flytende tre spenns hengebru hvor to tårn står på plattformer festet med strekkstag til bunnen (TLP). En parametrisert modell av en flerspenns hengebru har blitt utviklet, hvor dimensjonene fra konsepttegninger til den planlagte Bjørnafjord brua har blitt implementert. En generalisert metode for å finne systemmatrisene og last i modale koordinater, har blitt utviklet. Buffeting teori og lineær potensial teori har blitt brukt til å finne lastene fra vind og bølger på strukturen.

Modal-, response- og bevegelsesindusert ustabilitets analyser har blitt utført i frekvensplanet, hvor hydrodynamisk masse, demping og stivhet, og aerodynamisk demping og stivhet har blitt tatt høyde for. Miljøeffektene førte til betydelig lavere egenfrekvenser for systemet. Effekten av forskjellig kombinasjoner av stasjonære parametere for vind og bølger har blitt undersøkt. Vind ga størst bidrag på responsen i horisontal retning, og bølger i vertikal og torsjonell retning. Fra modal analyse, responsspektre og standardavvik ble det funnet at den første moden i horisontal og vertikal retning vil være den dominerende responsen i broen. Aerodynamisk bevegelsesindusert ustabilitet grense ble funnet til å være 88 m/s for 1.5217 rad/s.

Abstract

The Norwegian Public Road Administration has been investigating the possibilities of crossing the fjords on the west coast of Norway for the coastal highway E39 project. For the 5 km wide Bjørnafjorden a floating three span suspension bridge with two pylons standing on tension leg platforms (TLP), is considered. A parametrized model of a floating multi-span TLP suspension bridge has been created, where the parameters have been given the planned geometry of the Bjørnafjorden bridge concept. A hydrodynamic analysis conducted on a FE-model of a pontoon where added mass, damping, restoring forces and the wave transfer function were obtained. Buffeting theory and aerodynamic derivatives were used to obtain the buffeting forces, stiffness and damping terms. A generalized method was developed to couple system matrices and forces from wind and waves in modal coordinates.

Modal-, response- and motion induced instability analyses, all accounting for hydrodynamic added mass, damping and restoring forces and aerodynamic damping and stiffness, have been conducted in the frequency domain. The environmental effects resulted in significantly lower eigenfrequencies. A response analysis was carried out for combinations of different stationary parameters for wind and waves. It was evident that wind governed the response in transversal- and waves for the vertical and rotational directions for modes with higher corresponding eigenfrequenciees. The most participating modes was the first mode in transversal direction and the first mode in vertical direction, obtained from the modal analysis, frequency response spectra and standard deviations. An aerodynamic motion induced instability limit was found to de 88 m/s at 1.5217 rad/s.

Preface

This report is the result of 20 weeks work on our master thesis at The Norwegian University of Science and Technology (NTNU), at the institute of Structural engineering in Trondheim. It marks the completion our master's degree in engineering. We are Sondre Halden from the study programme Mechanical Engineering specialized in applied mechanics, and Shun Wei Gong in Civil Engineering specializing in computational mechanics. The process of working with this thesis has been very rewarding and educational. We have gained unique insight within bridge aerodynamics, hydrodynamics and bridge design. Leaping out in to new academic areas with long hours of tough and challenging discussions has resulted in a learning outcome and a thesis we have become very proud of.

We would like to thank Associate Professor Ole A. Øiseth, our supervisor for guidance and discussions to challenge our academic frontier. PhD-candidate and co-supervisor Yuwang Xu has been very helpful, and committed time and patience to guide us in the fundamentals in hydrodynamics and has been an important sparring partner throughout the project of writing the thesis. PhD-candidate Knut Andreas Kvåle has helped us with hydrodynamic software and provided us with case studies of floating bridges.

Lastly, we want to thank the guys at the office for the mid-night coffee breaks and good comradeship.

Shun Wei Gong   Sondre Halden

Contents

List of Tables

List of Figures

Notation

Abbreviations

EOM	=	Equation of motion
DOF	=	Degree of freedom
SDOF	=	Single degree of freedom
MDOF	=	Multi degree of freedom
CAD	=	Computer aided design
FE	=	Finite element
FEM	=	Finite element method
COB	=	Center of buoyancy
TLP	=	Tension leg platform
STD	=	Standard deviation
NPRA	=	Norwegian Public Road Administration
DNV	=	Det Norske Veritas
TDA	=	Teknisk data AS

Letters

A	=	Area
B	=	Height of girder
E	=	Modulus of elasticity
G	=	Shear modulus
I	=	Second order moment of area
n	=	Number of degrees of freedom
T	=	Temperature
V	=	Mean wind velocity
W	=	Width of girder
u, v, w	=	Wind velocity direction
x, y ,z	=	Cartesian coordinates
α	=	Scaling factor of eigenvector
μ	=	Real part of eigenvalue
v	=	Imaginary part of eigenvalue
λ	=	Eigenvalue
ω		Eigenfrequency

Matrices and vectors

$\mathbf{a}_r$	=	Spectral process of r vector
$\mathbf{C}$	=	Damping matrix
$\mathbf{H}$	=	Transfer function matrix
$\mathbf{K}$	=	Stiffness matrix
$\mathbf{M}$	=	Mass matrix
$\mathbf{Q}$	=	Wave transfer function
$\mathbf{R}$	=	External loading vector
$\mathbf{r}$	=	Response vector
$\mathbf{S}$	=	Spectral matrix
u, v, w	=	Wind velocity direction
x, y ,z	=	Cartesian coordinates
$\mathbf{\Phi}$	=	Eigenvector matrix
ϕ	=	Eigenvector

Symbols and subscripts

$\tilde{\mathbf{X}}$	=	Modal form of X
$\hat{X}$	=	Normalized from of X
$\overline{X}$	=	Average of X
X_f	=	relativ to wind direction

Chapter 1

Introduction

The Norwegian Public Road Administration (NPRA) is investigating the possibilities for crossing the fjords on the west coast of Norway for the ferry free E39 project, where the 5km wide Bjørnafjorden south of Bergen, being one of them. Several concepts are under development for this particular crossing such as submerged tunnel, floating bridge and floating suspension bridge, all with different possible sub solutions. In this thesis, the concept of a floating three span suspension bridge where two pylons stand on tension leg platforms (TLP) that are moored to the sea bed has been analysed. The technology has been used on oil rigs since the 1980s but has never before been used on a suspension bridge.

1.1 Scope of thesis

The scope of this thesis is to create a parametrized finite element model of a TLP moored floating suspension bridge and to conduct modal, response and instability analysis in the frequency domain. Environmental effects are to be accounted for from wind and wave loads.

This master thesis aims to create a parametrized model of a multi-span TLP bridge geometry. Since the model is parametrised the geometry and structural properties of the bridge can easily be changed, making the model relevant to use in other similar studies. In this thesis, the parameters will render the Bjørnafjorden TLP concept bridge. Environmental conditions of wind and wave loading are to be added to the model, i.e. motion induced hydrodynamic added mass damping and restoring force, and aerodynamic damping and stiffness. MATLAB will be used to write an input file to the finite element software, ABAQUS. Complex modal analysis will be conducted for the model, and a method has to be developed to handle the frequency dependent environmental effects on the eigenvalues

in a satisfying way.

Hydrodynamic effects on the pontoons will be obtained outside of ABAQUS. A CAD model of the pontoon in the software GeniE will be created. GeniE is compatible with the finite element software HydroD where a hydrodynamic analysis will be conducted. The hydrodynamic restoring force, the wave transfer function and the frequency dependent added mass and added damping will be output. A sea state representative for the fjord will be estimated. The sea state will be converted to load through the use of linear potential theory.

Aerodynamic coefficients, for the girder section planned to be used on the Bjørnafjorden bridge, is not available. Since aerodynamic wind tunnel tests all ready had been conducted for the Hardanger bridge girder it will be used instead. This girder cross section is smaller but shape wise similar. A wind field will be created in frequency domain. The wind spectrum will be the basis for the wind load, applied to the bridge through the use of the buffeting theory.

A response analysis of the bridge will be conducted in the frequency domain using MATLAB, where both hydrodynamic and aerodynamic effects will be accounted for. The response will be presented as spectral densities and standard deviation for selected nodes on the bridge. Wind and wave load participation on the response will be investigated.

Instability analysis due to aerodynamic motion induced self excited loading will be investigated. A methodology to find the critical mean wind velocity at the onset of an instability will be established and the mode shapes participating in the instability will be searched for. Hydrodynamic effects will also here be taken into account.

1.2 Structure of the report

Chapter 2 - Theory The theory describing the problem and solution strategies for the problem at hand. Basic structural dynamic theory, aerodynamic and hydrodynamic effects on a structure and motion induced instability limits are discussed in detail.

Chapter 3 - Initial design Initial design of the Bjørnafjorden concept bridge and its location based on reports from TDA is described.

Chapter 4 - Modelling A detailed description of the modelling of the parametrized bridge in ABAQUS and CAD modeling of the pontoon in HydroD/WADAM is presented. Hydrodynamic forces were obtained from WADAM for chosen sea parameters.

Chapter 5 - Analysis Eigenvalues and eigenvectors are obtained from the ABAQUS model. A generalized method for response analysis when accounting for both hydrodynamic and aerodynamic effects is developed. It is then applied on the case study of Bjørnafjorden. The algorithm from a MATLAB script is presented and applied for the Bjørnafjorden bridge.

Chapter 6 - Results and discussion A modal analysis is carried out with emphasis on the mode with significant pontoon motion. Results from the response analysis is discussed in detail. Motion induced instability conditions and instability modes from a 300 mode analysis is presented

Chapter 7 - Conclusion A summary of the main results and finding is presented.

Chapter 2

Theory

The theory chapter will present the fundamental theory of structural models coupled with forces from wind and waves in a finite element formulation. It is assumed the reader has basic knowledge in structural dynamics and statistics [8]. These topics are therefore only addressed in brief to identify the main ideas of this matter. A detailed description of wave theory, with modeling of a stochastic directional and frequency independent sea surface, is presented. Fluid structure interaction given a sea surface is thoroughly gone trough. Aerodynamic effects on a structure is derived for the buffeting theory and motion induced forces. A mathematical derivation of motion induced instabilities due to self exciting forces is given.

2.1 Dynamics

Response of large complicated structures are comprehensive to solve analytically and are therefore discretized in a finite element (FE) formulation describing the motion of the structure with a finite number n of degrees of freedom (DOF). The equation of motion (EOM) in time domain for such a discrete system is given as following:

$$\boldsymbol{M}\ddot{\boldsymbol{r}}(t) + \boldsymbol{C}\dot{\boldsymbol{r}}(t) + \boldsymbol{K}\boldsymbol{r}(t) = \boldsymbol{R}(t) \tag{2.1}$$

$\boldsymbol{M}, \boldsymbol{C}$ and $\boldsymbol{K}$ are the $n \times n$ mass stiffness and damping matrices and $\boldsymbol{R}$ is the $n \times 1$ loading vector. The left hand side of this equation consist of the forces related to the system motion, denoted r. $R(t)$ is the exciting forces independent of the system motion. Further in this thesis, the terms describing the right hand side will be referred to as the flow-induced forces, while the left hand side

As the damping force in equation of motion is difficult to describe for a coupled MDOF system, a frequently used method is to use the Rayleigh damping. Using a finite element program, representative matrices for M and K within the structure are developed.

$$\mathbf{C} = \alpha\mathbf{M} + \beta\mathbf{K} \tag{2.2}$$

where α and β are the Rayleigh coefficients determined from two eigenfrequencies of the system. The eigenfrequencies are determined from a solution were the damping is assumed to have negligible effect on the eigenfrequency.

The general solution to a homogeneous second order differential equation in matrix form, such as the homogeneous solution of Equation (2.1) for r is assumed to be

$$\mathbf{r}(t) = \sum_{i=1}^{n} \alpha_i \phi_i e^{\lambda_i t} \tag{2.3}$$

where α is a scaling factor between modes determined by the initial conditions. ϕ is the eigenvector and λ is the eigenvalue. Inserting Equation (2.3) back into the homogeneous form of the EOM an eigenvalue problem is obtained

$$\left(\mathbf{M}\lambda^2 + \mathbf{C}\lambda + \mathbf{K}\right)\mathbf{\Phi} = 0 \tag{2.4}$$

By using e.g. a state space method, n complex eigenvalues of the discrete system can be found.

$$\lambda_i = \mu_i + i\omega_i \tag{2.5}$$

An analytical system has infinitely many eigenfrequencies, and a discretised system has n number of eigenfrequencies concurrent with the number of DOFs in a FE representation. The number n number of eigenfrequencies of the system is the imaginary part of λ. From the n eigenvalues, n corresponding orthogonal eigenvectors can be determined.

The EOM matrix system becomes large when considering systems with many DOFs. Expressing Equation (2.1) in modal coordinates instead of DOFs is often computationally much more efficient, as the response is represented with a finite number n of eigenvectors. The response solution can be written as a superposition of mode shapes ϕ times a generalized displacement η. Thus,

$$\mathbf{r}(t) = \sum_{i=1}^{N_{mod}=n} \phi_i \eta_i(t) \approx \sum_{i=1}^{N_{mod}<n} \phi_i \eta_i(t) \tag{2.6}$$

By inserting (2.6) into EOM and pre-multiplying with $\boldsymbol{\Phi}$ transpose the EOM is obtained in its modal form.

$$\tilde{\mathbf{M}}\ddot{\eta}(t) + \tilde{\mathbf{C}}\dot{\eta}(t) + \tilde{\mathbf{K}}\eta(t) = \tilde{\mathbf{R}}(t) \tag{2.7}$$

where

$$
\begin{aligned}
\text{Modal mass matrix}: \quad & \tilde{\mathbf{M}} = \boldsymbol{\Phi}^T\mathbf{M}\boldsymbol{\Phi} \\
\text{Modal damping matrix}: \quad & \tilde{\mathbf{C}} = \boldsymbol{\Phi}^T\mathbf{C}\boldsymbol{\Phi} \\
\text{Modal stiffness matrix}: \quad & \tilde{\mathbf{K}} = \boldsymbol{\Phi}^T\mathbf{K}\boldsymbol{\Phi} \\
\text{Modal load vector}: \quad & \tilde{\mathbf{R}} = \boldsymbol{\Phi}^T\mathbf{R}
\end{aligned} \tag{2.8}
$$

The computational advantage lies in that a sufficient response analysis will be obtained by only superposing a small number of modes compared to the number of DOFs, n, depending on the frequency of the load. If the matrices for $\mathbf{M}$, $\mathbf{C}$ and $\mathbf{K}$ are symmetric, one will obtain diagonal matrices in modal form due to the properties of orthogonal eigenvectors. This will result in uncoupled equations of motions and the equations can be treated as N_{mod} SDOF systems.

The frequency domain representation of the equation of motion can be obtained by simply making a Fourier transform of the time-dependent processes. This implies taking the Fourier transform of Equation (2.1).

Where $a_r(\omega)$ is the Fourier amplitude to r(t) and $a_R(\omega)$ is the Fourier amplitude to the time dependent load R(t), the equation of motion in frequency domain can be expressed as following:

$$\left(-\omega^2\mathbf{M} + i\omega\mathbf{C} + \mathbf{K}\right)\mathbf{a}_\eta(\omega) = \mathbf{a}_r(\omega) \tag{2.9}$$

The content within the large paranthesis on the left hand side of equation 2.9 is the transfer function matrix, denoted $\mathbf{H}$.

$$\mathbf{H}(\omega) = \left(-\omega^2\mathbf{M} + i\omega\mathbf{C} + \mathbf{K}\right)^{-1} \tag{2.10}$$

Equation (2.9) can be reformulated to

$$\mathbf{a}_r(\omega) = \mathbf{H}(\omega)\mathbf{a}_R(\omega) \tag{2.11}$$

where the response is a function of the frequency dependent transfer function times the spectral load amplitude. The transfer function will give an indication on how a system react to unit loads and is the connection between load and response in frequency domain.

2.2 Wave theory

The objective of the following section is to mathematically model the wave surfaces, using traditional assumptions of the sea. A general wave surface is considered random in time and space and can be modeled as a stochastic process. Wave height, frequency of the waves and wave direction can be considered as random parameters that describe the random sea wave surfaces. A frequency domain formulation of wave height accounting for correlation between two arbitrary spatial points, randomness in wave direction, wave elevation and wave frequency will be derived.

Linear potential theory will briefly be applied in the description of added mass, hydrodynamic damping, restoring forces and wave transfer functions. These will be further assembled together with the stochastic wave surface description to obtain wave exciting forces. A frequency domain representation of hydrodynamic contribution in a system equation of motion can thus be derived and presented.

2.2.1 Sea surface as stochastic processes

Sea waves are essentially generated by wind and can be modelled as a physical surface with harmonically varying amplitude. Wave height, frequency of the waves, wave direction, crest length and wave surface location are often the key parameters that are needed to describe sea behavior; and are essential when considering wave interaction on structures. Traditionally, waves are modelled statistically using measured data of each key parameter for different sea locations. Sufficient measurements of the key parameters over time can give a clear notion of sea behavior for a specific sea location.

The amplitude of a sea wave surface is traditionally denoted η. This can be modeled as a function of time t, spatial location $r = [x, y]$ and wave number κ.

$$\eta(t) = a\cos(\omega t) \qquad\qquad \eta(x) = \cos(\kappa x + \varphi) \qquad (2.12)$$

Where a is the wave amplitude, φ is the wave phase, and κ is the wave number associated with the wave propagation direction and wave frequency; the two one-dimensional formulations for sea surface with elevation η can be assembled to a three-dimensional sea surface. A developed expression for a a single three-dimensional wave on a sea surface is expressed in Equation (2.13).

$$\eta(x, y, t) = a \cdot \cos(k \cdot r - \omega t + \varphi) \qquad (2.13)$$

κ is the wave number for two dimensions $[\kappa_x, \kappa_y]$ that accounts for directionality and wave frequency, phase angle, and time. Knowing that $\cos\alpha = \frac{1}{2}(\exp(i\alpha) + \exp(-i\alpha))$, the relation in 2.13 can be further developed and decomposed in to Equation (2.14).

$$\eta(x,y,t) = \{\frac{1}{2}a \cdot \exp(i\varphi)\}\{\exp(i(\kappa \cdot r - \omega t) + \exp(-i(\kappa \cdot r + \omega t))\} \qquad (2.14)$$

The first term $\{\frac{1}{2}a\cdot\exp(i\varphi)\}$ is often denoted the complex amplitude, here denoted c; as the wave amplitude a is found by Fourier transform, corresponding to κ_x, κ_y and frequency ω.

$$\eta(r,t) = \sum_{\kappa_x}\sum_{\kappa_y}\sum_{\omega_y} c(\kappa_x, \kappa_y, \omega)\{\exp(i(\kappa \cdot r - \omega t) - \exp(-i(\kappa \cdot r + \omega t)\} \qquad (2.15)$$

The linear superposition can be illustrated in Figure 2.1. The figure shows waves at a specified time t, propagating towards the same direction but with different scalar values of $\kappa = \kappa_y$ and using a random phase angle for each wave surface. The obtained expression in Equation (2.15) illustrates the randomness of the sea, having a random complex amplitude wrt. the wave directions and wave frequency. This expression can account for the varying elevation on the sea surface as a stationary and homogeneous stochastic process over the defined surface.
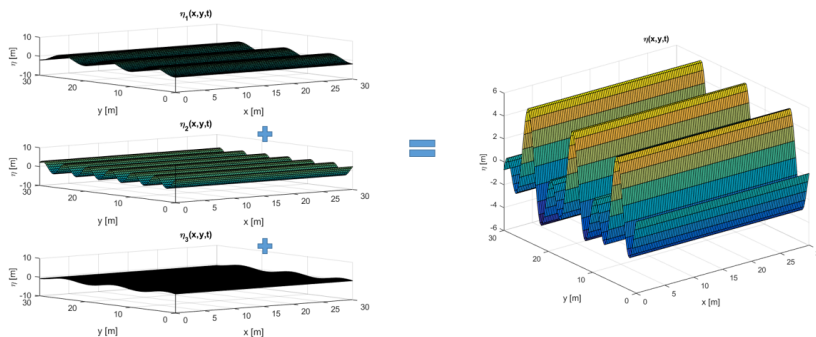
Figure 2.1: Harmonic wave surfaces with one-directional propagation

Using the assumptions that the wave surface is a stationary and homogeneous stochastic field with zero mean, Equation (2.15) can be written in a continuous form as in equatinon (2.16). The following formulation of the stochastic sea wave surface is based a paper from Ragnar Sigbjörnsson [6], for stochastic sea surface modeling, using higher order statistics.

$$\eta(r,t) = \int_{-\infty}^{\infty} \exp\{i(\omega t - \kappa \cdot r)\}dB(\kappa, \omega) \qquad (2.16)$$

where $B(\kappa, \omega)$ is the spectral process associated with wave elevation, including the com-

plex conjugates that have been written in the equations above. If one is to consider correlation in two points, e.g point n and m with corresponding x- and y-coordinates one can find the cross-correlation as shown in Equation (2.17

$$R_{\eta_r \eta_s} = E[\eta(r_r, t_r) \cdot \eta(r_s, t_s)^H] \tag{2.17}$$

To fulfil the assumptions of stationarity and homogeneity for the wave surface, Equation (2.18) and (2.19) need to be satisfied for the spectral process $dB(\kappa, \omega)$. The condition shown in Equation (2.18) describes zero correlation between the individual wave surfaces (e.g k and l) while Equation (2.19) is the condition of zero mean of spectral process associated with the wave elevation.

$$E(dB(\kappa, \omega)) = 0 \tag{2.18}$$

$$E\left[dB(\kappa_k, \omega_k) \cdot dB(\kappa_l, \omega_l)^H\right] = I_{kl} dG_{\eta\eta}(\kappa_l, \omega_l) \tag{2.19}$$

$G_{\eta\eta}(\kappa, \omega)$ gives the correlation function for the spectral process $B(\kappa, \omega)$ for two points k and l in a wave-number and-frequency space. I_{kl} in Equation (2.19) is the *Kronecker delta* ($k \times l$-matrix of 1's where $k = l$ and 0 elsewhere).

Where $G_{\eta_r \eta_s}(\kappa, \omega)$ is a three-dimensional wave spectral distribution, $S_{\eta_r \eta_s}$ is the corresponding cross-spectral density. The relation between the wave spectral distribution and corresponding wave cross-spectral density for two correlating points on the wave plane can be described as following:

$$G_{\eta_r \eta_s}(\kappa, \omega) = \int_\kappa S_{\eta_r \eta_s}(\kappa, \omega) d\kappa d\omega \tag{2.20}$$

When Equation (2.18) is fulfilled, the expression in (2.17) can be further developed by applying (2.19), and the correlation function can be expressed as following:

$$R_{\eta\eta}(\tau) = \int_\infty \int_\theta \int_\kappa S_{\eta\eta}(\kappa, \theta, \omega) \exp\left\{i\omega\tau\right\} \cdot \exp\left\{-i\kappa(\Delta x \cos\theta + \Delta y \sin\theta)\right\} d\kappa d\theta d\omega \tag{2.21}$$

where Δ denotes the distance between points m and n in x- and y- position between e.g distance points y_m and y_n on the wave surface plane. The time-variable τ denotes $t_m - t_n$ in time-space. Using the Wiener-Khintchine relation; one can express the cross-spectral density and the correlation function as a Fourier-transform pair. The Fourier transform of the correlation function gives the cross-spectral density

$$S_{\eta_r \eta_s}(\omega) = \frac{1}{2\pi} \int_{-\infty}^{\infty} R_{\eta_m \eta_n}(\tau) \exp\left\{-i\omega\tau\right\} d\tau \tag{2.22}$$

By substituting equation [2.21] into Equation (2.22), the following is obtained

$$S_{\eta_r \eta_s}(\omega) = \int_\theta \int_\kappa S_{\eta\eta}(\kappa, \theta, \omega) \exp\left\{ - i\kappa(\Delta x \cos\theta + \Delta y \sin\theta) \right\} d\kappa d\theta \qquad (2.23)$$

To account for, but simplifying the complexity of the three-dimensional spectral density function for wave elevation, the Dirac delta function can be used for a condition of when κ is equal to a one-to-one mapping of the absolute value of κ into frequency $f(\omega)$ for the three-dimensional $S_{\eta\eta}$ projection on the $\kappa - \omega$-plane. This implies that $S_{\eta_r \eta_s}(\kappa, \theta, \omega)$ will be zero for any $\kappa \neq f(\omega)$. The three-dimensional mathematical expression for spectral density can accordingly be reduced to two-dimensions for all $\kappa = f(\omega)$. If one is to assume that the wave directions are independent of the wave elevation, a two-parametric spectral density can be further expressed as a auto-spectral density function

$$S_{\eta\eta}(\omega, \theta) = S_{\eta\eta}(\omega) \cdot D(\theta) \qquad (2.24)$$

Equation (2.24) defines the two-dimensional spectral density function as two one-parametrized functions for respectively direction wrt. θ and a wave elevation wrt. ω. It is general practice to use the dispersion relation to determine κ from Airy wave theory and the second-order Stoke wave theory, given in Equation (2.25).

$$\omega^2 = g\kappa \tanh(\kappa h) \qquad (2.25)$$

h is here the water depth. For large h, i.e deep water waves, $\tanh(\kappa h) = 1$. Given that κ corresponds to value $f(\omega)$ on the $\kappa - \omega$ projection of the three-dimensional spectral density $S_{\eta_r \eta_s}(\kappa, \theta, \omega)$, the above relations can be used to derive a wave elevation spectrum that accounts for randomness of wave direction, two points with given spatial directions, and the extent of wave depth in the stochastic process. This can be shown in Equation (2.26).

$$S_{\eta_r \eta_s}(\omega) = S_{\eta\eta}(\omega) \int_\theta D(\theta) \exp\left\{ - if(\omega)(\Delta x \cos\theta + \Delta y \sin\theta) \right\} d\theta \qquad (2.26)$$

The cross-spectral wave elevation spectrum is accordingly obtained, assuming deep water wave and inserting $f(\omega) = \kappa(\omega) = \frac{|\omega|\omega}{g}$. The auto-correlation function $S_{\eta\eta}$ and $D(\theta)$ is obtained by measurements for the two given parameters done over time for specific sea locations and transformed into spectral densities. To summarize, the cross-spectral density function for wave elevation has been developed for two spatial points r and s on the surface, taking into account both the wave direction, single point wave elevation and water depth. Accordingly, the wave elevation function accounting for higher order statistics has been decomposed into components that usually are known or given for specific ocean locations.

2.2.2 Sea state parameters and wave spectra

Sea states define the stationary conditions for the sea and are often input data to e.g chosen directional distribution of $D(\theta)$ and auto-spectral density $S_{\eta\eta}$ that depend on sea locations. The traditional sea state parameters used to describe the wave surfaces as stochastic processes are significant wave height, mean zero crossing frequency/period, mean water level, mean wave propagation direction and crest length. The significant wave height is the mean of the 1/3rd highest wave heights that will occur in a time interval. The relevant statistical parameters for the stochastic process can be calculated assuming that the sea follows the behavior of a chosen auto-spectral wave elevation function $S_{\eta\eta}$. Expressions for variance, mean zero crossing period and the significant wave height are developed using the relations in Table 2.1. Tidal and current levels and swell are also stationary parameters that should be taken into account for wave loading.

Description	Relation
Spectral moments $(n = 0, 1, 2...)$	$m_k = \int_a^b f^n S(f) df$
Variance	$\sigma^2 = m_0$
Significant wave height	$H_s \approx 4\sigma$
Mean zero crossing period	$T_z = \sqrt{\frac{m_0}{m_2}}$

Table 2.1: Relations between stationary parameters and $S_{\eta\eta}$

As variance, significant wave height and mean zero crossing periods traditionally are derived using spectral moments, the choice of an auto-spectral wave elevation spectrum will affect the results using the given stationary parameters for simulation of waves. The cross-spectral density function, derived in Equation (2.26) is also directly dependent on this choice.

2.2.3 Auto-spectral density for wave elevation

The spectra that give the auto-spectral density function of wave elevation show how sea wave elevation energy is distributed over different frequencies for one arbitrary point on the homogeneous sea surface. These spectra are physically intuitive and obtainable as they in principle are the Fourier-transform of wave elevation measurements over a longer period of time. Over the last decade, several sea wave spectra have been developed for different oceans that directly depend on the mean zero wave period/frequency and a significant wave height.

One-parametric Pierson-Moskowitz spectrum
The one-parametric Pierson-Moskowitz spectrum is one of the auto-spectral wave elevation spectra that are derived using wave elevation measurements. It is based on measure-

ments in the North Atlantic from 1964 by Pierson and Moskowitz. The spectrum has how-ever been used for many other sea locations. A relation for a one-parametric PM-spectrum can be given as in Equation (2.27) with H_s as parameter.

$$S_{\eta\eta}(\omega) = \frac{\alpha g^2}{\omega^4} \cdot exp\big(\frac{-B}{\omega^5}\big) \tag{2.27}$$
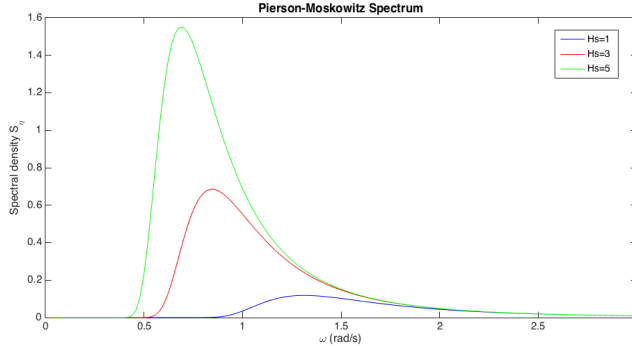
Figure 2.2: Pierson Moskowitz spectrum for different values of parameter significant wave height H_s

The components can be denoted $B = 3.11/H_s^2$, where $\alpha = 0.0081$, g is the gravitational acceleration and H_s the significant wave height. The relation in (2.27) is equivalent with the relation for wave spectral density in Table 2.1 by $S(\omega) = S(f)/2\pi$. It is evident from Figure 2.2 that the peaks are shifted wrt. different frequencies for higher H_s. There are many other spectra that take into account more parameters, such as the multi-parametrical spectra of Pierson-Moskowitz, Bretdtschneider, JONSWAP and Torsethaugen. These will not be emphasized for further analysis in this thesis.

2.2.4   Directionality function

As waves propagate in many different directions, wave spreading functions are developed. The directionality functions fulfil Equation (2.28).

$$\int_\theta D(\theta,\omega)d\theta = 1 \tag{2.28}$$

A traditional expression used for the directionality function has the stationary parameter mean wave direction. The Cos^{2s}-function is frequently used to express this spreading and is shown in Equation (2.29).

$$D(\theta) = C\cos^{2s}\big(\frac{\theta - \theta_0}{2}\big) \tag{2.29}$$

θ is the wave direction to a fixed referential axis in the sea, θ_0 is the angle of the mean

wave direction, while s is a parameter for the wave crest length. C is the constant such that Equation (2.29) will be fulfilled. Larger s gives a larger crest length and a more narrowly spread function around the mean wave direction. The effect of the directionality function will be evident when considering Equation (2.24) and (2.26).
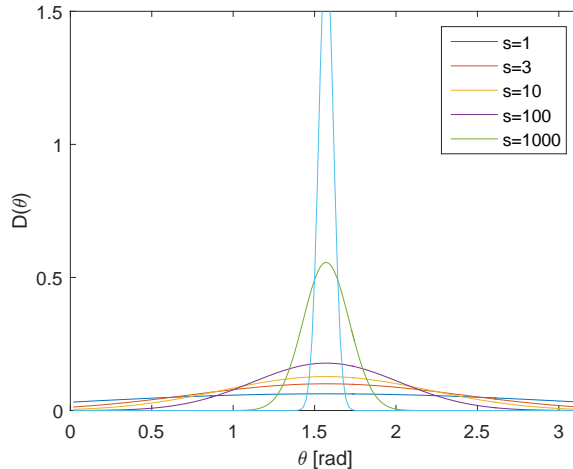
Figure 2.3: Directional spectrum for different values of crest length s

2.2.5 Wave forces

In the above sections, it has been shown that irregular seas can be modeled using a linear superposition of multiple waves. By using linear potential theory, one can obtain forces and response on a structure by taking the superposition of the force and response from multiple single waves. An approach of obtaining structure response using linear potential theory will be described in this subsection.

Obtaining wave forces for a structure requires mathematical models to describe the fluid and the fluid-structure interaction. These models can be obtained using potential theory where the water is assumed incompressible and the fluid motion is irrotational. The problem can be sub-divided into two problems. One of the sub-problems is to obtain the forces when the structure is fixed and restrained from oscillating. The second of the two sub-problems is to obtain the wave forces on the structure when it is forced to oscillate with the wave frequency. This is illustrated in Figure 2.4. Solving these two problems result in wave- and motion induced forces. The wave-induced forces acting on a submerged structure, can be described as a sum of incidential and diffractional wave effects. The incident wave effects are the wave forces from undisturbed waves, not accounting for the diffraction when waves hit the structure.

Hydrodynamic forces are usually calculated for a submerged reference node, e.g the *Center of buoyancy* for motion on the submerged structure; accounting for 3 translative and 3
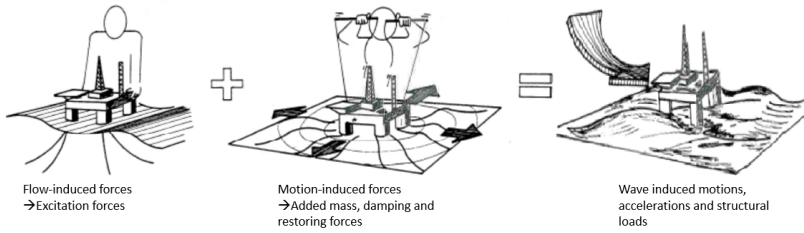
Figure 2.4: Flow/wave- and motion- induced forces

rotational DOFs, (x, y and z and rotation about corresponding axes for a fixed coordinate system). Each of these rigid body motions can be denoted η_j with j from 1 to 6.

2.2.6 General sea water assumptions, potential theory

Fluid particles in sea water can be described using velocity potential and Bernoulli's equation. Firstly, the conditions that all three conditions need to be explicitly satisfied for, will be denoted as ϕ.

It follows that assumptions of irrotational fluid motion, flat seabed, and sea water incompressibility are conditions that must be satisfied to make linear wave potential theory applicable. The two sub-problems of obtaining wave forces are to consider the forces when the structure is standing still and when it is forced to oscillate. The total potential considering linear wave potential can be expressed as following:

$$\phi(x, y, z, t) = \phi_0(x, y, z, t) + \phi_D(x, y, z, t) + \phi_R(x, y, z, t) \tag{2.30}$$

ϕ_0, ϕ_D and ϕ_R are respectfully the incidential, diffractional and radiational velocity potentials. ϕ_0 and ϕ_D assemble the wave excitation forces. The corresponding forces of these velocity potentials can be calculated separately.

2.2.7 Wave excitation forces

The wave excitation forces are results of forces from incident waves and from diffracted waves, whereas the velocity potentials to these can be denoted ϕ_0 and ϕ_D. The incidential velocity potential, based on assumptions of a sea without obstacles/structures can be expressed using Airy wave theory.

$$\phi_0 = -\frac{Ag}{\omega} \frac{\cosh(\kappa(z + h))}{\cosh(\kappa h)} \exp\left\{i\kappa(x\cos\theta + y\sin\theta)\right\} \tag{2.31}$$

In Equation (2.31), A denotes amplitude, κ the wave number, h the water depth, θ the wave direction and z the vertical direction with positive direction upwards. The diffractional velocity potential can be expressed as following:

$$V = \nabla \phi_D = i\frac{\partial \phi_D}{\partial x} + j\frac{\partial \phi_D}{\partial y} + k\frac{\partial \phi_D}{\partial z} \tag{2.32}$$

As sea water is assumed incompressible and irrotational, meaning $\nabla \cdot V = 0$ and $\omega = \nabla \times V = 0$, the governing equation for wave potential for radiation can therefore be expressed as following:

$$\nabla \cdot V = \frac{\partial^2 \phi_D}{\partial x^2} + \frac{\partial^2 \phi_D}{\partial y^2} + \frac{\partial^2 \phi_D}{\partial z^2} \tag{2.33}$$

Equation 2.33 is equivalent with showing that the equation needs to satisfy the Laplace equation. By applying Bernoulli's equation for constant fluid pressure and the dynamic free-surface condition, meaning that the water pressure is equal the atmospheric pressure on the free-water surface, and using only the linear terms, Equation (2.34) is obtained [2].

$$\frac{\partial^2 \phi_D}{\partial t^2} + g\frac{\partial \phi_D}{\partial z} = 0 \tag{2.34}$$

As incidential waves are traversing through a structure and the diffracted waves diffract from the structure, the following boundary condition is accordingly applied for the incidential and diffractional forces.

$$\frac{\partial \phi_D}{\partial n} = -\frac{\partial \phi_0}{\partial n} \quad \text{giving} \quad \frac{\partial (\phi_0 + \phi_D)}{\partial n} = 0 \tag{2.35}$$

By also assuming a horizontal sea bottom where h is the water depth:

$$\frac{\partial \phi_D}{\partial z} = 0 \quad \text{for} \quad z = -h \tag{2.36}$$

The diffractional potential is not always necessary to calculate explicitly for finding the total exciting force including the incidential and diffractional force effects. Industry software calculate the total exciting force using Haskind's relation by applying Green's second identity to calculate the total wave force [5]. The following relation can then be applied:

$$F_{exc,k} = -i\omega\rho \int_{S_B} (n_k \phi_0 - \frac{\partial \phi_+}{\partial n}\phi_R)dS \tag{2.37}$$

As Equation (2.37) often is calculated with a unit wave amplitude, one can simply denote

the total wave exciting force as the given relation times a wave amplitude. The wave transfer function F_{exc} can be further denoted as Q_r, for a wave surface position r.

2.2.8   Radiation forces

With radiation, one assumes a submerged structure forced to oscillate with the wave frequency. As a radiation force describes the forces in an oscillating system or a structure, it is reasonable to decompose the force into a mass, damping and stiffness force components. By applying the explicit boundary conditions for radiation, the radiation force can be expressed as a function of the obtained radiation velocity potential ϕ_R.

The radiation velocity potential ϕ_R needs to explicitly fulfil the conditions of free surface and a flat seabed with zero fluid motion at the water bottom, and structure oscillation towards wave direction. The radiation velocity potential is:

$$V = \nabla \phi_R = i \frac{\partial \phi_R}{\partial x} + j \frac{\partial \phi_R}{\partial y} + k \frac{\partial \phi_R}{\partial z} \qquad (2.38)$$

Moreover, the conditions of irrotationality and incompressibility needs also to be satisfied explicitly for the radiation potential, giving the governing equation:

$$\nabla V = i \frac{\partial^2 \phi_R}{\partial x^2} + j \frac{\partial^2 \phi_R}{\partial y^2} + k \frac{\partial^2 \phi_R}{\partial z^2} \qquad (2.39)$$

The dynamic free surface condition becomes

$$\frac{\partial^2 \phi_R}{\partial t^2} + g \frac{\partial \phi_R}{\partial z} = 0 \qquad (2.40)$$

Also, the radiation potential needs to be satisfied for the boundary condition on the water plane

$$\frac{\partial \phi_{R,k}}{\partial n} = n_k \qquad (2.41)$$

Equation (2.41) is given such that the structure motion is driven with the wave direction. Boundary values of zero water motion at the sea bottom and infinitely small waves at an infinitely long distance from the structure need to be considered, where the latter can be satisfied showing $\frac{\partial \phi_{R,j}}{\partial n} = 0$ at the sea bottom $z = -h$. The expression for the radiation velocity can be further derived as in the equation below, [3].

$$\phi_R(x, y, z, t) = Re\Big[\sum_{j=1}^{6} \frac{d\eta_j}{dt} \cdot \varphi_j\Big] \tag{2.42}$$

Using the boundary conditions Equation (2.42) can be obtained where j is the number of the motions in j-th degree of freedom, where $\frac{d\eta_j}{dt}$ denotes the velocities of these, while φ denotes the potential per unit velocity of the structure. Each of the unit velocities needs to satisfy the body boundary condition $\frac{d\varphi_j}{dn} = n_j$. The motion induced force can hence be derived as a function of the time-derivative of the velocity potential times the water density, integrated over the wetted surface of the structure as shown below.

$$F_{rad,k} = -\int_{S_{0B}} \rho \frac{\partial \phi_R}{\partial t} n_k dS \tag{2.43}$$

Equation (2.43) can be further decomposed as matrices times the double and single derivative wrt. time with two matrices with equivalent composition as one has in EOM.

$$F_{rad,k} = \sum_{j=1}^{6} \Big\{ -A_{kj} \frac{d^2 \eta_j}{dt^2} - B_{kj} \frac{d\eta_j}{dt} \Big\} \tag{2.44}$$

k denotes the force direction where the added mass and damping coefficients are denoted A_{kj} and B_{kj} with 6x6 coefficients of j, k. One obtains accordingly the heave damping and heave inertia force (z-direction) when the force direction k equals the motion direction j using derivations from [2] and [3].

$$A_{kj} = Re\Big[\rho \int_{S_{0B}} \varphi_j n_k dS\Big] \qquad B_{kj} = -\omega Im\Big[\rho \int_{S_{0B}} \varphi_j n_k dS\Big] \tag{2.45}$$

The motion induced forces are accordingly obtained using relation (2.45). Matrices A and B will account for each regular wave with a frequency ω.

2.2.9   Restoring forces

There is also a hydrodynamic stiffness in the water, meaning that a rigid body motion of a structure will cause a force striving to keep the structure in original position, as shown in Figure 2.5. The hydrostatic force and moment can be derived by integrating along the time-dependent submerged surface as shown in Equation (2.46). This is illustrated in Figure 2.5.
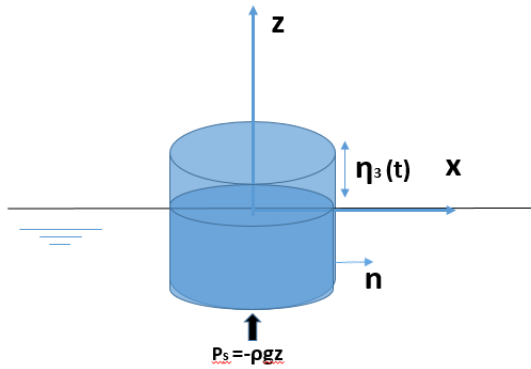
Figure 2.5: Hydrostatic restoring force in body motion.

$$F_k = -\int_{SB(t)} P_k \cdot n_j dS \qquad M_k = -\int_{SB(t)} P_k(x \times n_j)dS \qquad (2.46)$$

Where P_k is the hydrostatic pressure $P_k = -\rho g z$. Using relation (2.46), one can decompose the force in motion η_j and a matrix with hydrostatic stiffness coefficients C_{kj} as in the equation below. It is necessary to define the the wetted sea surface differently as the restoring force in the floating equilibrium position should be zero, and displacements from this position to restoring force lead to

$$F_{restoring,k} = -\sum_{j=1}^{6} C_{kj}\eta_j \qquad (2.47)$$

If one is to show the restoring force when displacing the structure in downwards negative direction for a structure as in Figure 2.5 with k and $j = 3$, the restoring force in heave direction will be

$$F_{restoring,3} = C_{33}\eta_3 = \rho g A_{wp} \qquad (2.48)$$

A_{wp} will be the cross sectional area at the water plane. For e.g a cylinder, this area will be the circular area of the cylinder.

2.2.10 Total wave force

The coefficients obtained for A_{kj}, B_{kj} and C_{kj} have the same dimensions as the matrices in mass, damping and stiffness matrices in equation of motion and are valid for one single

sea state. If one is to sum up all the waves and the corresponding force components, these three matrices can accordingly be denoted $M_h(\omega)$, $C_h(\omega)$ where M_h and C_h are time/frequency dependent while C_{kj} can be denoted K_h and only depends on the structure geometry submerged under water as a linear superposition of multiple sea states. Using the linear potential theory to develop expressions for these three terms, the developed matrices will only in special cases be symmetrical. It is worth noting that the formulation follows that added mass and damping should not be physically interpreted as added mass on the structure and added damping. It will follow that the pressure fields (considering the integrals) between fluid and structure generates propagating forces over the whole sea.

$$F_{tot}(\omega) = F_{exc}(\omega) - \big(\big(-\omega^2 M_h(\omega) + i\omega C_h(\omega) + K_h\big) \cdot B_u(\omega) \quad (2.49)$$

These forces are decomposed such that they can be integrated in a FE formulation for EOM; where added mass, damping and stiffness in practice can be added to obtain a resultant mass, damping and stiffness from both the structure and the force effects from the water.

In a frequency domain formulation, cross-spectral wave exciting forces between two spatial points can be formulated as following, taking into account the cross correlation function for wave elevation:

$$S_{p_r p_s}(\omega, \theta) = \lim_{T \to \infty} \frac{1}{T\pi} \big[Q_r(\omega, \theta) \cdot Q_s(\omega, \theta)^H\big] \cdot S_{\eta_r, \eta_s} \quad (2.50)$$

$S_{\eta_r \eta_s}$ is the same function as derived in Equation (2.26). The expression in Equation (2.50) needs to be integrated over the possible wave direction angles, and the resulting exciting force of waves is obtained in the following formulation.

$$S_{p_r p_s}(\omega) = \int_\theta Q_r(\omega, \theta) S_{\eta_r \eta_s} Q_s(\omega, \theta)^H d\theta \quad (2.51)$$

Q_r and Q_s will be the wave transfer function for two submerged structures or objects in position r and s, the two points of which wave elevation correlation is accounted for.

2.3 Aerodynamic theory

The objective of the following sections is to give a mathematical description of the wind field and how it affects the response on line like structures [7]. The theory is focused on slender bridges but is also applicable on other structures e.g. tall towers. The wind field is first presented in the time domain before it is assumed a stochastic process and transformed to the frequency domain. Interaction between the response of the bridge girder and the oncoming flow is worked out in detail using quasi-static buffeting theory. A finite element formulation will be obtained from buffeting forces. Moreover, motion induced aerodynamic instability will be addressed

2.3.1 The wind field

The wind field is considered random in time and space. The wind direction is assumed to be perpendicular to the bridge longitudinal direction,consisting of a mean and a fluctuating part where the mean wind velocity is constant. The mean wind velocity profile varies with height above ground, z. It is assumed zero at the ground due to friction and is increasing and converging when z is large enough, z_c. For bridges with girders high above the water plane and the entire girder is at approximately the same height, such that V_{mean} is considered constant.

$$U(x,t) = V_{Mean} + u(x,t) \tag{2.52}$$

u is time and positional time dependent fluctuating part of the wind field and is assumed much smaller than V_{mean}. By Equation (2.52) the wind field is only varying along the longitudinal direction x of the bridge and in time. $u(x,t)$ is the turbulent part of the wind field with randomly fluctuating wind velocity and zero mean value. The fluctuating part is split into three orthogonal components, u in the main flow direction, v in the bridge direction and w in the vertical direction. The wind field has also its own coordinate system where u, v, is parallel with x_f, y_f, z_f

$U(x,t)$ in Equation (2.52)is from wind measurments at the site. Measurements are typically done for short term, with 10 minutes intervals. For such a short time interval, the stochastic wind field is assumed to be statistically stationary and homogeneous. By computing the mean wind velocity and standard deviation, a Gaussian probability distribution of the short term time series can be obtained. Having a large set of short term measurements one can combine them and find the probability distribution for long term mean wind velocity and standard deviation at the site. Investigating the maximum value from each short term time series and create a probability distribution of maximas. Both the mean and maxima long term probability distributions can be fitted to a Weibull or a Rayleigh distribution [1]. The probability distribution of maximas is used when calculating extreme response. When doing response simulations of a structure its impossible to test for all stationary short term conditions, so one should choose cases from around the conditions

with highest probability and from the extreme conditions.

Doing correlation and covariance calculations between two processes at different time and/or space, or on the process itself at different time, will provide information about relationships in the short term time domain ensemble data. The cross spectral density of the wind can then be calculated from the covariance. Wind measurements for two different point, a and b, separated in space and time, i.e

$$
\mathbf{U}_a = \begin{bmatrix} u(s,t) \\ v(s,t) \\ w(s,t) \end{bmatrix} \qquad \mathbf{U}_b = \begin{bmatrix} u(s+\Delta s, t+\tau) \\ v(s+\Delta s, t+\tau) \\ w(s+\Delta s, t+\tau) \end{bmatrix} \qquad (2.53)
$$

where $\Delta s = [\Delta x, \Delta y, \Delta z]$ is the spatial separation and τ is the time lag between the measurements. u and w are in the wind directional coordinate system. The covariance of the two wind measurements is given as

$$
\mathbf{Cov}(\Delta s, \tau) = \begin{bmatrix} Cov_{uu} & Cov_{uv} & Cov_{uw} \\ Cov_{vu} & Cov_{vv} & Cov_{vw} \\ Cov_{wu} & Cov_{wv} & Cov_{ww} \end{bmatrix} = E\left[\mathbf{U}_a \cdot \mathbf{U}_b^T\right] = \frac{1}{T}\int_0^T \left(\mathbf{U}_a \cdot \mathbf{U}_b^T\right) dt
$$

$$(2.54)$$

where an element in the covariance matrix can be written as

$$
Cov_{mn}(\Delta s, \tau) \qquad\qquad m, n = u, v, w
$$
$$
\Delta s = \Delta x_f, \Delta y_f, \Delta z_f
$$

where subscript f refers to the coordinate system of the oncoming flow. If only considering wind on the girder of a bridge it can only be spatial separation in the $x(= y_f)$ direction. Covariance for y and z can be omitted for simplicity, i.e. $s = x = y_f$. The ratio between the covariance and the product of the standard deviation of the to time series in direction n and m is

$$
\rho_{mn}(\Delta y_f, \tau) = \frac{Cov_{mn}(\Delta y_f, \tau)}{\sigma_m \sigma_n} \qquad (2.55)
$$

Where σ_k is

$$\sigma_k = \sqrt{\int_0^T m(t)^2 dt} \tag{2.56}$$

where $k = m, n$. For $\rho_{mn}(\Delta y_f = 0, \tau = 0) = 1$. The ratio is decaying for both increasing τ and Δy_f. Equation (2.54) gives 27 components of $Cov_{mn}(\Delta s, \tau)$. The wind in the along bridge deck direction, v, is of little interest in wind loading analysis and is therefore omitted. By also assuming only $\Delta s = \Delta y_f$ Equation (2.54) is therefor reduced to

$$\mathbf{Cov}(\Delta y_f, \tau) = \begin{bmatrix} Cov_{uu}(\Delta y_f, \tau) & Cov_{uw}(\Delta y_f, \tau) \\ Cov_{wu}(\Delta y_f, \tau) & Cov_{ww}(\Delta y_f, \tau) \end{bmatrix} \tag{2.57}$$

Cross covariance of two processes is equal to cross correlation if the mean part of both the processes are zero. Equation (2.57) can therefor be inserted into Equation (A.2), defining the cross spectral density for wind velocities.

$$\mathbf{S}(\Delta y_f, \omega) = \begin{bmatrix} S_{uu}(\Delta y_f, \omega) & S_{uw}(\Delta y_f, \omega) \\ S_{wu}(\Delta y_f, \omega) & S_{ww}(\Delta y_f, \omega) \end{bmatrix} \tag{2.58}$$

Equation (2.58) is the cross spectral density of the wind field in any two point along the girder in wind directions u and w (global coordinate directions, x and z).

2.3.2 Wind Loading - Buffeting theory

Different types of wind forces dominate the response at different mean wind velocities for slender structures. The static response is due to the mean wind velocity for low to high mean wind speeds. At very high mean wind velocity (depending on the structure) motion induced loads will dominate the response. The standard deviation of the response is govern by vortex shedding at fairly low mean wind velocities, buffeting forces at intermediate wind speeds and motion induced loads at high wind velocities. This is illustrated in Figure 2.6.[7]

Buffeting forces and motion induced forces will be derived in the following. Vortex shedding is not within the scope of this thesis.

Wind loading is the sum of two main contributions

$$q_{tot} = q(x, t) + q_{ae}(x, t, r, \dot{r}, \ddot{r}) \tag{2.59}$$
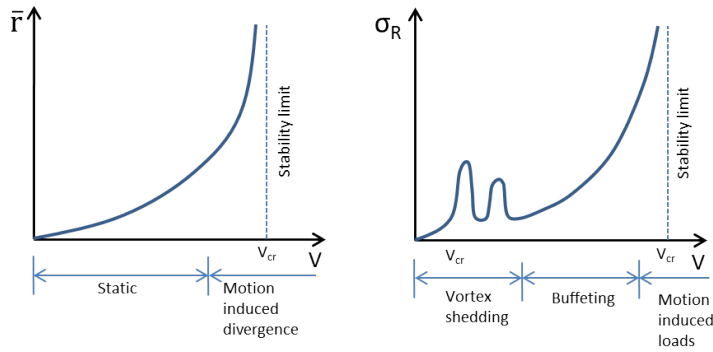
Figure 2.6: Typical response variation with mean wind velocity

where q_{ae} are the motion induced forces, and $q(x,t)$ is the flow induced forces due to the instantaneous wind velocity pressure at a point. The buffeting wind load includes the load by the mean and fluctuating part of the wind field on a structure. The oncoming flow is given in Equation 2.52). The mean height of the bridge is assumed large and constant along the span. Additional wind felt by the structure comes from the movement of the structure relative to the oncoming flow. It is in the following assumed that the response in the x direction of the structure due to wind loading is small compared to the y and z direction, and is therefor neglected. The buffeting theory is based on the use of the instantaneous velocity pressure, using Bernoulli's equation

$$q(t) = \frac{1}{2}\rho[U(t)]^2 \tag{2.60}$$

where ρ is the air density. Furthermore, load coefficients obtained from static wind tunnel tests and the linearization of nonlinear phenomena will render satisfyingly accurate results. It is further assumed that V_{mean} is much larger than $u(x,t)$ and $w(x,t)$ and that the cross sectional displacement and rotations are small, and can be split into a mean and fluctuating part. The structure is assumed to be approximated as a line-like structure. A bridge will have response in the vertical, translational and torsional direction of the girder.

Figure 2.7 shows the displacements and rotations done by a cross section due to: 1. $U = 0$ still air (zero displacement and rotation), 2. $U = V_{mean}$ mean wind velocity and 3. $U = V_{mean} + u(t)$ mean wind velocity and fluctuating wind. The instantaneous forces and moments are by definition in flow axis given by
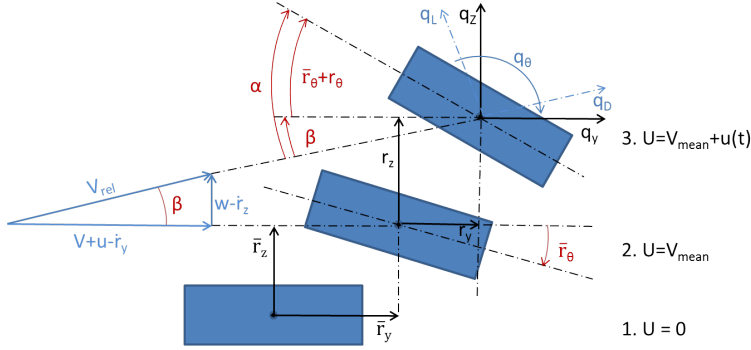
Figure 2.7: Displacements and rotations of cross section at position x

$$
\begin{bmatrix} q_D(x,t) \\ q_L(x,t) \\ q_M(x,t) \end{bmatrix} = \frac{1}{2}\rho V_{rel}^2 \cdot \begin{bmatrix} D \cdot C_D(\alpha) \\ B \cdot C_L(\alpha) \\ B^2 \cdot C_M(\alpha) \end{bmatrix} \tag{2.61}
$$

where C_D, C_L and C_M are the drag coefficients in drag, lift and moment, respectfully, V_{rel} is the instantaneous relative velocity and α is the angel between V_{rel} and the bridge relative y directional cross section. B and D is the width and thickness of the girder section, respectfully. The dimensions are newton (or newton meters for q_M) per unit length. Transforming the equating above into structural axis gives

$$
\mathbf{q}_{tot}(x,t) = \begin{bmatrix} cos\beta & -sin\beta & 0 \\ sin\beta & cos\beta & 0 \\ 0 & 0 & 0 \end{bmatrix} \cdot \begin{bmatrix} q_D \\ q_L \\ q_M \end{bmatrix} \tag{2.62}
$$

where

$$
\beta = arctan\left(\frac{w - \dot{r}_z}{V + u - \dot{r}_y}\right) \tag{2.63}
$$

Linearizing the system by making two assumptions.

1. The fluctuating flow component u(x,t) and w(x,t) are much smaller than V_{mean}, and that crossection rotation and displacement are small. i.e. (See Figure 2.7)

$$cos\beta \approx 1$$

$$sin\beta \approx tan\beta \approx \beta \approx \frac{w - \dot{r}_z}{V + u - \dot{r}_z} \approx \frac{w - \dot{r}_z}{V}$$

$$V_{rel}^2 = (V + u - \dot{r}_y) + (w - \dot{r}_z)^2 \approx V^2 + 2Vu - 2V\dot{r}_y$$
$$\alpha = \overline{r_\theta}r_\theta + \beta \approx \overline{r_\theta} + r_\theta + \frac{w}{V} - \frac{\dot{r}_z}{V} \tag{2.64}$$

2. Linearizing the nonlinear flow coefficients around an average rotational angle of the cross section. This angle is set to rotation done by the mean wind conditions. $\overline{\alpha} = \overline{r}_\theta$
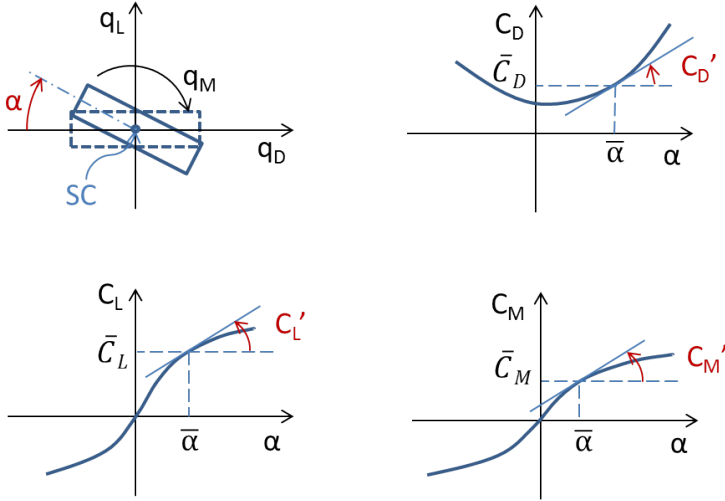
Figure 2.8: Linearization of drag, lift and moment coefficients

$$\begin{bmatrix} C_D(\alpha) \\ C_L(\alpha) \\ C_M(\alpha) \end{bmatrix} = \begin{bmatrix} C_D(\overline{\alpha}) \\ C_L(\overline{\alpha}) \\ C_M(\overline{\alpha}) \end{bmatrix} + \alpha_f \begin{bmatrix} C'_D(\overline{\alpha}) \\ C'_L(\overline{\alpha}) \\ C'_M(\overline{\alpha}) \end{bmatrix} \tag{2.65}$$

where $C'_D(\overline{\alpha}), C'_L(\overline{\alpha})$ and $C'_M(\overline{\alpha})$ are the slopes at $\overline{\alpha}$, and $\alpha_f = r_\theta + \frac{w}{V} - \frac{\dot{r}_z}{V}$ is the fluctuating part of the angel incidence. In the further we set $C_i(\overline{\alpha}) = \overline{C}_i$ and $C'_i(\overline{\alpha}) = C'_i$, $(i = D, L, M)$ for simplicity.

Combining Equation 2.61 - 2.65) gives

$$
\begin{bmatrix} q_y \\ q_z \\ q_\theta \end{bmatrix}_{tot} = \rho V \left(\frac{V}{2} + u - \dot{r}_y \right) \left\{ \begin{bmatrix} D\overline{C}_D \\ B\overline{C}_L \\ B^2\overline{C}_M \end{bmatrix} + \left(r_\theta + \frac{w}{V} - \frac{\dot{r}_z}{V} \right) \begin{bmatrix} DC'_D \\ BC'_L \\ B^2C'_M \end{bmatrix} + \frac{w\dot{r}_z}{V} \begin{bmatrix} -B\overline{C}_L \\ D\overline{C}_D \\ 0 \end{bmatrix} \right\}
$$

$$(2.66)$$

Rearranging Equation (2.66) and disregarding higher over terms of quantities assumed small, the following is obtained

$$
\mathbf{q}_{tot} = \begin{bmatrix} \overline{q}_y(x) \\ \overline{q}_z(x) \\ \overline{q}_\theta(x) \end{bmatrix} + \begin{bmatrix} q_y(x,t) \\ q_z(x,t) \\ q_\theta(x,t) \end{bmatrix} = \overline{\mathbf{q}} + \mathbf{B}_q \cdot \mathbf{v} + \mathbf{C}_{(ae)} \cdot \dot{\mathbf{r}} + \mathbf{K}_{ae} \cdot \mathbf{r} \qquad (2.67)
$$

where

$$
\mathbf{v}(x,t) = \begin{bmatrix} u & w \end{bmatrix}^T \qquad (2.68)
$$

$$
\overline{\mathbf{q}}(x) = \begin{bmatrix} \overline{q}_y \\ \overline{q}_z \\ \overline{q}_\theta \end{bmatrix} = \frac{\rho V^2 B}{2} \begin{bmatrix} (D/B) \cdot \overline{C}_D \\ \overline{C}_L \\ V\overline{C}_M \end{bmatrix} = \frac{\rho V^{"} B}{2} \cdot \hat{\mathbf{b}}_q \qquad (2.69)
$$

$$
\mathbf{B}_q(x) = \frac{\rho V B}{2} \begin{bmatrix} 2(D/B)\overline{C}_D & ((D/B)C'_D - \overline{C}_L) \\ 2\overline{C}_L & (C'_L + (D/B)\overline{C}_D) \\ 2B\overline{C}_M & BC'_M \end{bmatrix} = \frac{\rho V B}{2} \cdot \hat{\mathbf{B}}_q \qquad (2.70)
$$

$$
\mathbf{C}_{ae}(x) = -\frac{\rho V^2 B}{2} \begin{bmatrix} 2(D/B)\overline{C}_D & ((D/B)C'_D - \overline{C}_L) & 0 \\ 2\overline{C}_L & (C'_L + (D/B)\overline{C}_D) & 0 \\ 2B\overline{C}_M & BC'_M & 0 \end{bmatrix} \qquad (2.71)
$$

$$\mathbf{K}_{ae}(x) = \frac{\rho V^2 B}{2} \begin{bmatrix} 0 & 0 & (D/B)C'_D \\ 0 & 0 & C'_L \\ 0 & 0 & BC'_M \end{bmatrix} \tag{2.72}$$

Equation (2.69) represents the time invariant part of the load vector. This part gives rise to the mean cross sectional displacements and rotations. The remaining part of Equation (2.67) is the fluctuating, time varying part. Calculating deformatings or cross sectional stress due to the constant $\bar{q}$ is assumed trivial and is left out for the rest of the derivations, reducing Equation (2.67) to

$$\mathbf{q}(x,t) = \begin{bmatrix} q_y(x,t) \\ q_z(x,t) \\ q_\theta(x,t) \end{bmatrix} = \mathbf{B}_q \cdot \mathbf{v} + \mathbf{C}_{ae} \cdot \dot{\mathbf{r}} + \mathbf{K}_{ae} \cdot \mathbf{r} \tag{2.73}$$

$\mathbf{B}_q \cdot \mathbf{v}$ is the dynamic loading from the turbulence in the oncoming flow. $\mathbf{C}_{ae} \cdot \dot{\mathbf{r}}$ and $\mathbf{K}_{ae}\mathbf{r}$ are the loads associated with the motion and displacement of the cross section. Linearity has been obtained so the theory is applicable also in the frequency domain. By taking the Fourier transform of Equation (2.73) the frequency domain amplitudes of the loads are obtained.

$$\mathbf{a}_q = \mathbf{B}_q \cdot \mathbf{a}_v + (i\omega \mathbf{C}_{ae} + \mathbf{K}_{ae})\mathbf{a}_r \tag{2.74}$$

where

$$\begin{aligned} \mathbf{a}_f(x,\omega) &= \begin{bmatrix} a_{q_y} & a_{q_z} & a_{q_\theta} \end{bmatrix}^T \\ \mathbf{a}_r(x,\omega) &= \begin{bmatrix} a_{r_y} & a_{r_z} & a_{r_\theta} \end{bmatrix}^T \\ \mathbf{a}_v(x,\omega) &= \begin{bmatrix} a_u & a_w \end{bmatrix}^T \end{aligned} \tag{2.75}$$

where i is the imaginary unit. The structural model is easiest to handle in frequency domain in modal coordinates. Introducing two adjustments to equation [2.75],

1. Introduce frequency dependent flow induced dynamic loads to $\mathbf{B}_q(x)$, i.e.

$$\mathbf{B}_q(x, \omega) = \frac{\rho V B}{2} \begin{bmatrix} 2(D/B)\overline{C}_D A_{yu} & ((D/B)C'_D - \overline{C}_L)A_{yw} \\ 2\overline{C}_L A_{zu} & (C'_L + (D/B)\overline{C}_D)A_{zw} \\ 2B\overline{C}_M A_{\theta u} & BC'_M A_{\theta w} \end{bmatrix} \quad (2.76)$$

where A is a suggested cross sectional admittance functions.

$$A_{mn}(\omega) = \frac{1}{(1 + a_{mn} B\omega/V)^{b_{mn}}} \quad (2.77)$$

where $m = y, z, \theta$ and $n = u, w$. Equation [2.77] is equal to one for $\omega = 0$ and diverges towards zero when ω goes towards infinity. The function acts as a filter to zero out loads at high frequencies. The admittance function is in general determined from wind tunnel test of the cross section, and the one given above is an approximation. As the Fourier transform of the flow induced wind load can be denoted $B_q(x, \omega) \cdot a_v(\omega)$, the spectral density of the force becomes:

$$S_Q(\omega) = \lim_{T \to \infty} \frac{1}{\pi T} \left[B_q \cdot a_v \cdot a_v^* \cdot B_q^* \right] \quad (2.78)$$

As $a_v = [a_u a_w]$, the cross spectral density function for wind velocity for wind in vertical and translative direction.

2. The coefficients in the $\mathbf{C}_{ae}$ and $\mathbf{K}_{ae}$ matrices are in reality frequency dependent. The coefficients in Equation (2.71-2.72) are determined from the quasi static buffeting theory and doesn't consider changes in C_D, C_L and C_M due to vibration of the cross section. To get more accurate coefficients, doing wind tunnel tests of a cross section turns out to give better results. These coefficients are called the aerodynamic derivatives and are discussed below.

2.3.3 Aerodynamic derivatives

The frequency dependent versions of Equation (2.71-2.72) are [7]

$$\mathbf{C}_{ae} = \begin{bmatrix} P_1 & P_5 & P_2 \\ H_5 & H_1 & H_2 \\ A_5 & A_1 & A_2 \end{bmatrix} \qquad \mathbf{K}_{ae} = \begin{bmatrix} P_4 & P_6 & P_3 \\ H_6 & H_4 & H_3 \\ A_6 & A_4 & A_3 \end{bmatrix} \quad (2.79)$$

The coefficients in Equation (2.79) are experimentally determined by wind tunnel test of the cross section and are function of mean wind reduced velocity and cross sectional properties. The matrices become significant to the system at high wind velocities in the case of unstable motion. The testes are therefor only tested thereafter. The reduced wind velocity is given as

$$\hat{V} = \frac{V}{\omega_i(V)B} \tag{2.80}$$

where V is the mean wind velocity, $\omega_i(V)$ is the executed free vibrating eigenfrequency due to the mean wind velocity and B is the width of the cross section. From the wind tunnel test one will get several sets of experimentally determined aerodynamic derivatives for the different reduced velocities. It is common to normalize $\mathbf{C}_{ae}$ with $\rho B^2 \omega_i(V)/2$ and $\mathbf{K}_{ae}$ with $\rho B^2 [\omega_i(V)]^2/2$, where $\omega_i(V)$ is the mean wind velocity dependent resonance frequency associated with mode shape i from from which the coefficients have been extracted. Non-dimentionalizing of the coefficients, gives

$$\mathbf{C}_{ae} = \frac{\rho B^2}{2} \cdot \omega_i(V) \cdot \hat{\mathbf{C}}_{ae} \qquad \mathbf{K}_{ae} = \frac{\rho B^2}{2} \cdot [\omega_i(V)]^2 \cdot \hat{\mathbf{K}}_{ae} \tag{2.81}$$

where

$$\hat{\mathbf{C}}_{ae} = \begin{bmatrix} P_1* & P_5* & BP_2* \\ H_5* & H_1* & BH_2* \\ BA_5* & BA_1* & B^2 A_2* \end{bmatrix} \qquad \hat{\mathbf{K}}_{ae} = \begin{bmatrix} P_4* & P_6* & BP_3* \\ H_6* & H_4* & BH_3* \\ BA_6* & BA_4* & B^2 A_3* \end{bmatrix} \tag{2.82}$$

The coefficients $(P_j, H_j, A_j, j = 1...6)$ are known as the aerodynamic derivatives. For $V \neq 0$, K_{ae} will change the EOM system matrix. The eigenfrequencies will change and so will the response. The effect of C_{ae} is most significant for wind velocity close to instability. For lower velocities it is the K_{ae} that has the largest effect on the EOM and the response. Because of the presents of K_{ae} and C_{ae} the eigenfrequencies must obtained by iteration when accounting for aerodynamic effects.

2.3.4 Motion induced instabilities

Motion induced instabilities response occur when a small increase in mean wind velocity generates a large increase in structural response, and at the limit, an infinite response, like illustrated in figure (2.6). The instability will occur for a critical response frequency, ω_{cr}, at a critical velocity, V_{cr} [7].[12]

There are four types of response instabilities. 1) Stability limit for $\omega_{cr} = 0$ is a static instability identified for V_{cr}. 2) Dynamic instability in the z direction, called galloping, 3) Dynamic instability in the θ_x direction, and 4) Dynamic instability as a coupling of z and θ_x direction response, called flutter.

When doing aerodynamic instability analysis the only forces considered are the self exited forces induced by the flow for relatively high mean wind velocities, .i.e the $\mathbf{B}_q$ is neglected.

$$\mathbf{F} = \mathbf{C}_{ae}\dot{\mathbf{r}} + \mathbf{K}_{ae}\mathbf{r} \tag{2.83}$$

Note that $\mathbf{C}_{ae}$ and $\mathbf{K}_{ae}$ are rarely symmetric matrices. These asymmetric matrices enable unstable response to be coupled among natural modes of the considered structure. Moving the motion induced forces over to the left hand side of the EOM, the homogeneous second order differential equation is obtained as described in section 2.1. By again assuming the solution from Equation (2.3) for the homogeneous EOM, repeated here, the eigenvalue problem is obtained.

$$\mathbf{r}(t) = \sum_{j=1}^{n} \alpha_j \phi_j e^{\lambda_j t}$$

Solving the quadratic eigenvalue problem will give $2n$ eigenvalue solutions(where n is the number of DOFs). Complex conjugate eigenvalues $\lambda_j = \mu_j \pm iv_j$ render complex eigenvectors of the form $\phi_j = \xi_j \pm i\zeta_j$. One of the assumed solution from the superposition of Equation (2.3) gives

$$r_j = (\alpha_j + i\beta_j)e^{(\mu_j + iv_j)t}(\xi_j + i\zeta_j) + i(\alpha - i\beta_j)e^{(\mu_j - iv_j)t}(\xi_j - i\zeta_j) \tag{2.84}$$

where α_j and β_j are arbitrary constants. If all the roots of the eigenvalue problem are complex conjugates, there will be n solutions of the form in Equation (2.84). Equation (2.3) can then be written as

$$r_j = \sum_{j=1}^{n} e^{\mu t} \left[-2(\beta_j \xi_j + \alpha\zeta_j)sin(\omega_j t) + 2(\alpha_j \zeta_j - \beta_j \xi_j)cos(\omega_j t) \right] \tag{2.85}$$

where $v_j \equiv \omega_j$. If $\mu_j < 0$ Equation (2.84) and (2.85) will render a converging oscillatory solution, implying damping dissipates energy from the system. If $\mu > 0$ the response will have diverging oscillatory behavior with frequency ω_j. Recalling that μ originated from the complex conjugate solution of the eigenvalue problem, its value is determined by the coefficients in the system matrix. It is when $\mathbf{C}_{ae}$ becomes larger than $\mathbf{C}$ due to increasing mean wind velocity μ becomes negative.

To better understand the physical meaning of μ, a one DOF system is used as an exam-

ple. The eigenvalue problem in Equation (2.4) can then be solved using normal quadratic function solution solver. The following is obtained

$$\lambda = \frac{-C \pm \sqrt{C^2 - 4MK}}{2M} \qquad (2.86)$$

where $C = C_s - C_{ae}(V)$. Again complex conjugate solutions are assumed. The real part is then, $\mu = -(C_s - C_{ae})/2M$. Because C_{ae} is increasing with increasing V, μ becomes negative when $C_{structural} < C_{ae}$ for the sDOF system.

Chapter 3

Initial Design

The object of this chapter is to give an overview of the design of the Bjørnafjorden bridge concept, with focus on the main structural components for the bridge that will be modeled in chapter 4. Bridge components with the assumed largest mass and stiffness contributions will be considered.

3.1 Overview

The Bjørnafjorden crossing is part of the Norwegian Public Road Administration's (NPRA) project for a ferry free E39 highway from Kristiansand to Trondheim. Bjørnafjorden is south of Bergen and partially protected from the North Sea by island groups around the fjord. A TLP-anchored floating suspension bridge to cross the 5 km wide fjord was one of three concepts that were proposed for the Bjørnafjorden crossing, where the pontoon solutions were developed by Teknisk Data (TDA). [10].
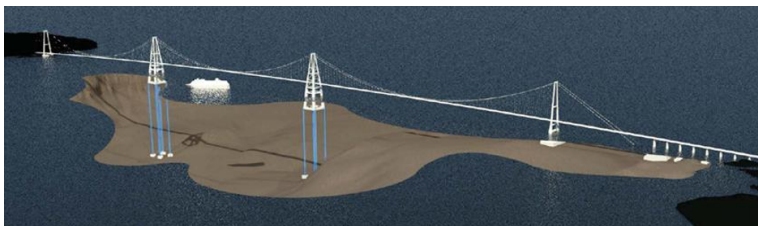
Figure 3.1: Overview of the entire TLP concept bridge
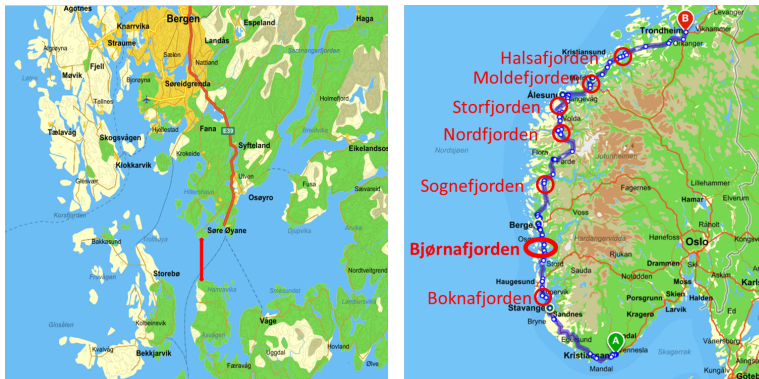
Figure 3.2: Left: map of Bjørnafjorden, Right: map of planed E39

3.2   General arrangement

The planed bridge concept consists of three spans, each being 1385 meters long. There will be two fixed concrete towers and two floating tension leg moored pontoons with pylons. There will also be a 600 meter concrete ramp onto the bridge from the north approach due to the shallower water, and a short ramp from the south. The water depths beneath northern- and southern pontoon are 450 and 550 meters, while the height of the towers above sea level is 198 meter The floating pontoons are submerged 65 meters under water.

Floating towers

Several designs for the towers have been suggested. The design presented in this thesis is the four legged tower. The floating towers consist of a 75 meter steel pontoon and a 188 meter steel pylon. The total height will be 263m and the bottom footprint, 96 by 75 meters. The total weight of a single tower are designed to 27000 tons. Figure 3.3 can be seen for further details.

Fixed Towers

The fixed towers will be made of concrete with a hollow rectangular cross section. The towers will be fixed to the ground out in the water. Detailed drawings of the fixed towers have not been available other than the conceptual overview drawing given in figure 3.1.

Girder

The concept bridge girder is an aerodynamic steel box. The trapezoidal cross section gives the girder high torsional stiffness and has advantageous aerodynamic properties against motion induced instabilities, with wind conducted wind tunnel tests. The girder has a radial curvature of 70'000m and will be a class H8 with two traffic lanes and one pedestrian lane. It was changed from class H9 to H8 in February 2016 and was not available when writing the thesis. In Figure 3.4, the class H9 section is presented. The H8 is very similar, but narrower. [9]

Figure 3.3: Sketch of floating towers

Figure 3.4: Cross section of class H9 design

Cable systems

The two main cables will be prefabricated parallel wire strand (PPWS) cables. The changing of the girder box from class H9 to a narrower and lighter class H8 changed the required cable strength from 1770 MPa to 1860 MPa when giving a reduction of the cross 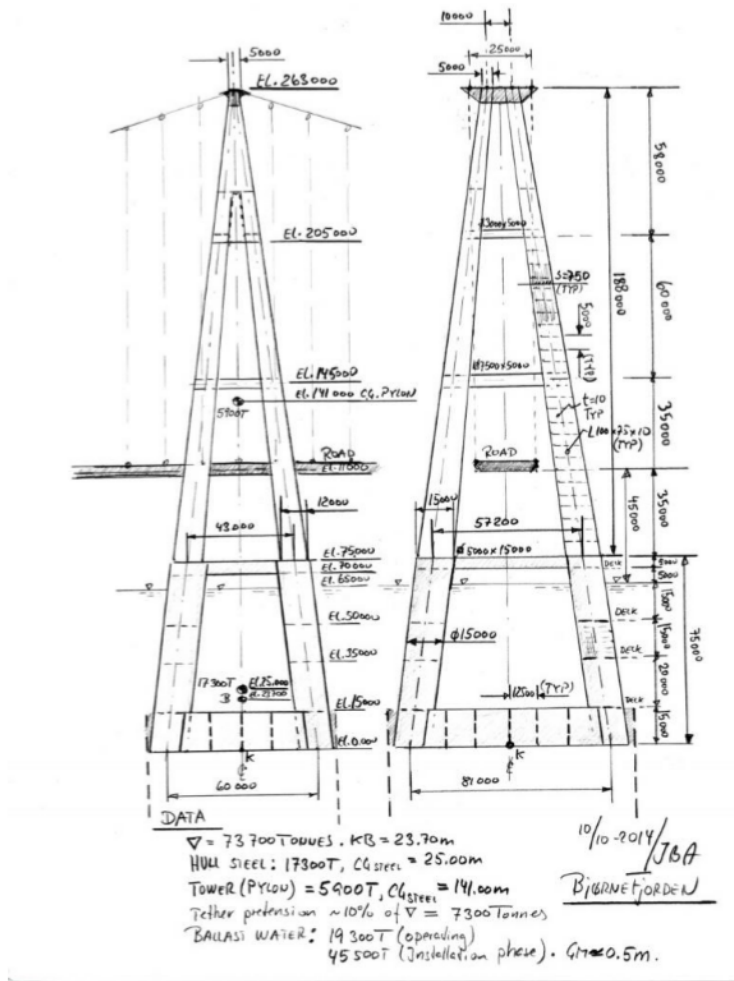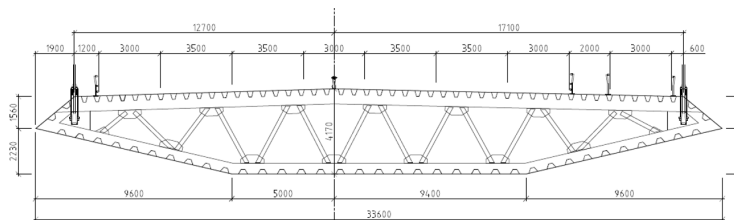section needed for the cables. The cross section of the cable will be a hexagonal shape as shown in figure 3.5. The main cable geometry corresponding to the new H8 girder was not applicable at the time of the writing of the thesis. The previously planned H9 cable consisted of 94 strands of 127 wires with a nominal diameter of 5.96 mm. The total number of wires would then be 11938. The sectional area of one main cable was then 0.333 m^2. To avid corrosion the cable is covered with elastomeric wrapping, making it airtight, also around the hangers, so its possible to perform dehumidification. The cable has also been compacted with hot galvanized s-shaped wrapping wires. The main cables will not hang vertically. The top of the towers are narrower than the girder so the cable plane will be tilted outwards at the mid-span to reach the width of the girder. [9]
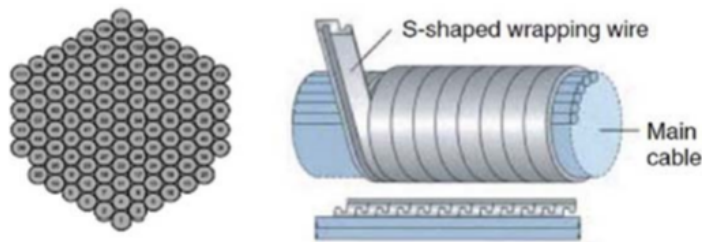
Figure 3.5: Cross section of main cable and wrapping

Hangers

There should be a hanger every 24 meters along the girder, i.e. 57 hangers on each side per span. The hanger ropes are designed as parallel wire strand (PWS). They are coated with high-density polyethylene (HDPE) sheath or locked coil with HDPE sheath. The hanger is fastened to sockets that are pin connected to the cable clamp and anchored with a cylindrical socket in the the bridge deck.

Tension legs

The purpose of the tension legs is to pull the floating towers lower than there natural height of buoyancy. This increases the stability of the bridge in all directions and maintains the strong tensioning in the thether, which as a consequence could lead to jerks and possible failure. The total tendon force at mean sea level is approximately 190MPa at each tower. At each of the four corners of the base of the floating towers three tethers are are mounted, each with a cross section area of $0.1239m^2$. The tension legs (tethers) will be tubular steel sections with outer diameter of 1118mm and thickness of 38mm. The considered steel yield limit is 420MPa. The length of the tethers are 550 and 450 meter for the south and north tower, respectfully.

Chapter 4

Modelling

This chapter gives a detailed description of the development of the parametrized TLP multispan suspension, what assumptions have been made and the limitations of the model.

This chapter gives a detailed description of the process of developing and parametrizing a TLP-based multi-span suspension bridge. The model is given the input parameters for the dimensions, cross sectional and material properties of the Bjørnafjorden bridge, outlined in 3. All the dimensioning input parameters can be seen in Table 4.1. The cross section of the girder and its properties from the Hardanger bridge was used for convenience as aerodynamic data and derivatives were available.

The submerged part of the floating towers, the pontoon, have been modeled using the softwares GeniE and HydroD from the DNV Sesam package for hydrodynamic analysis of the floating pontoons.

Moreover, the environment has been modeled using environmental data gathered by NPRA and TDA and by using appropriate spectral models.

Figure 4.1: Numerical model of the Bjørnafjorden bridge

4.1 Bridge modeling

MATLAB was used to generate .txt files with node lists with corresponding node x,y,z coordinates and element lists with corresponding node numbers. An input f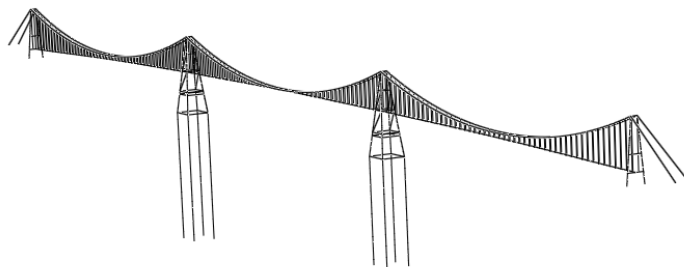ile (.INP) for ABAQUS was written in the language ABAQUS KEYWORDS using MATLAB to a text file. The node- and elements lists were imported to the .inp file when needed. The advantage of using MATLAB to generate the input file became evident for all iterative process, e.g when creating 34 element sets with different cross sectional properties for the tower legs.

```
444    % Tensionlegs and TLP
445    fprintf(fid,['** Constraining TLP and Tensionlegs \n']);
446    for i = 1:length(Coupling_Tensionlegs)
447        fprintf(fid,[ '*KINEMATIC COUPLING, REF NODE=%.0f \n'], Coupling_TLP(i));
448        fprintf(fid,[ '%.0f, 1, 3 \n'], Coupling_Tensionlegs(i));
449    end
450    fprintf(fid,['** \n']);
451    fprintf(fid,['** \n']);
```

(a) MATLAB code generating code for the .INP file for ABAQUS

```
646    ** Constraining TLP and Tensionlegs
647    *KINEMATIC COUPLING, REF NODE=16104
648    17100, 1, 3
649    *KINEMATIC COUPLING, REF NODE=16204
650    17200, 1, 3
651    *KINEMATIC COUPLING, REF NODE=16304
652    17300, 1, 3
653    *KINEMATIC COUPLING, REF NODE=16404
654    17400, 1, 3
655    *KINEMATIC COUPLING, REF NODE=26104
656    27100, 1, 3
657    *KINEMATIC COUPLING, REF NODE=26204
658    27200, 1, 3
659    *KINEMATIC COUPLING, REF NODE=26304
660    27300, 1, 3
661    *KINEMATIC COUPLING, REF NODE=26404
662    27400, 1, 3
663    **
664    **
```

(b) .INP file generated from MATLAB code

Figure 4.2: Sample of code generated for ABAQUS from a MATLAB file

Using an input file rather then a graphical interface was a more efficient way of creating the parametrized bridge model if changes to the bridge geometry were to be made.

The global origin of the model was set to the intersection of the girder and the fixed left tower; whereas the x-axis is along the girder, y-axis transversal to the girder and the z-axis were set in the vertical direction. All geometry was modelled as wire elements and assigned cross sections and material properties.

Table 4.1 shows the the input for the parametrized bridge, where all units are in meters. Behind the name of the parameter is the indicated direction of the component, denoted x,y or z. The program will return a node and element lists for a symmetric bridge about the longitudinal direction and about the midspan. The floating towers and fixed towers will be equal, and placed relative to the main cable given by the "Individual span length, x". "Crosser height, z" gives the height of the horizontal beams on the fixed and floating towers.

If adding another tower is desirable one only has to put in the parameters for the extra span, i.e. add an extra column to the main cable properties and "Number of hangers per span per side".

The model was put under gravity load and a temperature gradients on the main cables were used to restore the deformation. Three models were created accounting for respectfully structural properties, structural and hydrodynamic properties and structural, hydrodynamic and aerodynamic properties.

The parameters were given the values from the geometry, cross section and material properties of the Bjørnafjorden bridge concept, outlined in chapter 3. A complete table of cross sectional, material properties and element types used is given in the appendix, Table B.1.

All the components have been assigned material- and cross sectional properties. These parameters are easy to change in the script generating the input file for ABAQUS. In figure 4.3 is an example of what the code looks like for the left main cable.

```
% Main Cable
fprintf(fid,[ '*BEAM GENERAL SECTION, ELSET=MainCableElements_right, SECTION=GENERAL, DENSITY=8676  \n']);
fprintf(fid,[ '0.333, 6e-5, 0, 6e-5, 1.2e-4   \n']);  %A. Ixx, Ixy, Iyy, J
fprintf(fid,[ '0, 0, -1  \n']);
fprintf(fid,[ '200e9, 76.923e9, 1e-5  \n']); %E,G=E/(2(1+v)), alpha
fprintf(fid,['*DAMPING, ALPHA=0.0008, BETA=0.0307 \n']); % Rayleigh damping coefficients
```

Figure 4.3: Code defining the cross section and material properties for the left main cable

4.1.1 Main Cable

The two main cables consists of three spans and side cables from the fixed towers to ground. Each cable is sagging in the z direction and tilted outwards in the y direction, as illustrated in figure 4.4. The left cable for one span was created using a second degree polynomial functions in both the z-x plane and the x-y plane using the three point method. Tower height and mid span height was used in the x-z plane, and tower top width and girder width at mid span for the x-y plan. This is illustrated in figure 4.5. The procedure was repeated for the two other left spans before the right main cable was generated by mirroring the left cable over the z-x plane.
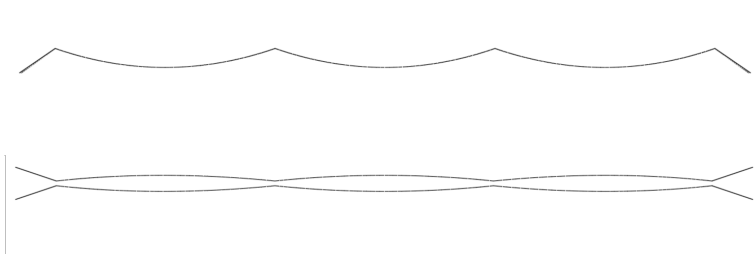
Figure 4.4: Shape of main cable in x-z plane (top) and x-y plane (bottom)

Table 4.1: Inputs to the parametrized model

Main Cable			[m]
Individual span length, x	1385	1385	1385
Main cable height at span midpoint, z	34	34	34
Main cable width at midpoint, y	10	10	10
Side cable on ground, x,y,z	-220	-20	0
Hangers			[-]
Number of hangers per span per side	57	57	57
Girder			[m]
Girder height at midpoint, z	32		
Connector node rel. girder, z	3		
Connector node rel. girder, y	9		
Floating tower			[m]
Width of tower top, y	20		
Width of base of tower, x	60		
Length of base of tower, y	80		
Tower height over water plan, z	188		
Tower depth under water plane, z	65		
Crosser height, z	95	35	-35
Center of buoyancy, z	-85.22		
Fixed tower			[m]
Tower top width, y	20		
Tower base width, y	58		
Crosser height, z	153	50	0
Tension legs			[m]
Water depth under tower, z	-550	-450	
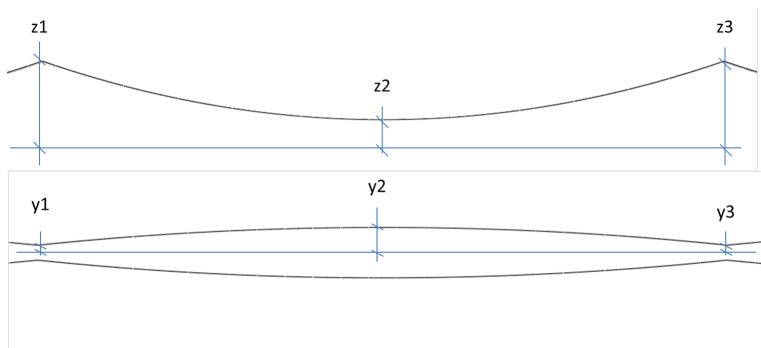
Figure 4.5: Distances used to calculate the cable shape in x-z plane (top) and x-y plane (bottom)

The side cables at one end of the bridge, are symmetric about the z-x plane. The input for one of the side cables were the x,y and z coordinate of the ground position, as illustrated in figure 4.6. The side cables at the other end are created by mirroring the first end.
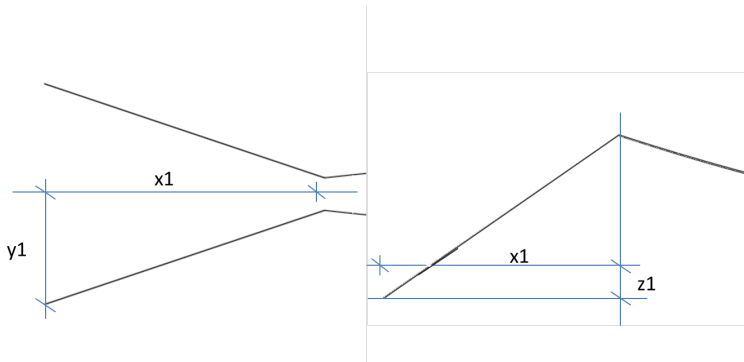
Figure 4.6: Distances used to calculate side cable shape in x-y-z plane

Since the nodes for the spans were generated separately, duplicate nodes between spans at the tower tops had occurred. They were deleted because it would be easier to handle one unique node list for the main cable later in the modeling. No data for the cable geometry was applicable i.e sag of the cables, so it was assumed to be close to tangential to the girder at middle span.

To avoid moment forces on the floating towers the three cable spans were given the same geometry. The distance from the cable at mid spans to the girder was therefore shorter for the center span than for the the side spans.

4.1.2 Girder

The girder was modeled using a second degree polynomial in the x-z plane to approximate the 70000m radius [9]. The girder was therefore 30m higher at midpoint than at the fixed towers. The mechanical properties and cross sectional area of the girder was set equal to the girder used on the Hardanger bridge. It was chosen because aerodynamic derivatives were available for the further aerodynamic analysis. When aerodynamic derivatives are available for the correct cross section one simply need to change the numbers in the code to initiate them.
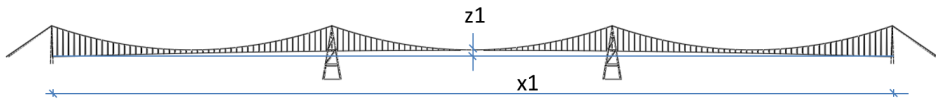
Figure 4.7: Distances used to calculate girder shape in the x-z plane

4.1.3 Connector nodes

Since the girder is modeled with a 1D wire element, it could not be able to represent torsional motion properly. Nodes relative to the girder nodes were added, called connector nodes, as shown in figure 4.8. Kinematic coupling constraints of the displacement and rotation between a girder node and the closes connector node was used.
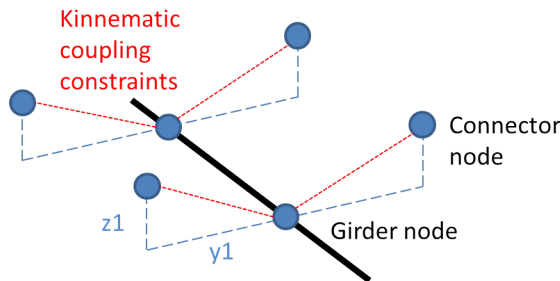
Figure 4.8: Connector nodes off sett to the girder by distances y1 and z1 with kinematic constraints

4.1.4 Hangers

The number of hangers per span is an input. With equal length of the spans it is reasonable to have equally many hangers, and was set to 57 per side per span for all spans with equal

24m spacing. A hanger is modeled as a single element between the connector nodes and nodes on the main cable, as illustrated in figure 4.9.
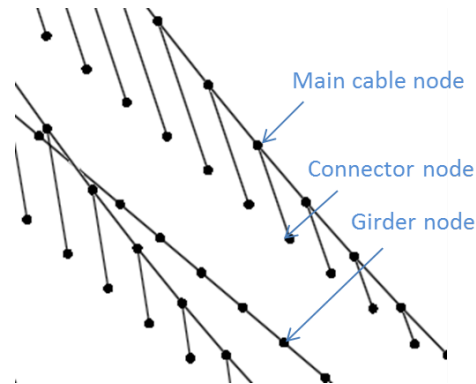
Figure 4.9: The hangers are single elements from the girder nodes to the connector nodes

4.1.5 Floating towers

The drawing in figure 3.3 is used as a basis for the modeling dimensions. Each floating tower consists of a pylon, pontoon-pylon connection and a pontoon, as shown in figure 4.10. The tower was created in a local coordinate system, making it easy to duplicate and transform to the right global coordinates, relative to the positions of the tops of the main cables. The tilting angle of one tower leg in the x-z and y-z plane is input, and is generated by first degree polynomial functions. It is then mirrored about the x-z and y-z plane to generate the three other legs. The number of horizontal beams on the pylon is input and the diagonal beams were generated automatically from the intersection of diagonal beams and tower legs. The diagonal beam are not part of TDAs tower design but were added for additional stiffness, with advice from Bjørnafjorden Expert Panel participant, Ole Øiseth. The pylon legs have a linearly varying cross section, and were modeled such that each element at each height on the leg is constant. The pontoon-pylon connector and pontoon have constant cross section. The cross section of the horizontal beams are each constant but different for each height. The X on the middle of the pontoon, seen in figure 4.10 is the center of buoyancy, 24.78m above the tower base, calculated with HydroD and is kinetically coupled in displacement and rotation to the base corners of the pontoon.

Due to the lacking information on cross sections of the components on the floating tower, these had to beestimated. The weight of the tower is important for the response analysis such that the density of the material would be adjusted to meet the weight of 27'000 tons.
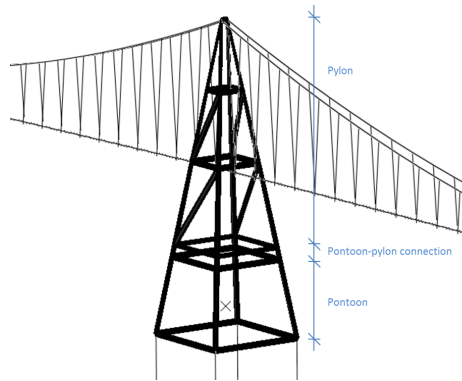
Figure 4.10: Floating tower

4.1.6 Tension legs

In the original design there are three tethers in each corner of the pontoon, but they have been modeled as one in each corner with the accumulated cross section. The corner nodes of the bottom of the towers are used as reference points when the tension leg nodes are created. The length of the tension legs are equal for each tower but can differ between towers. They are set to 550m and 450m as the original design is. 20 element per leg were considered enough.

4.1.7 Fixed tower

Since detailed drawings of the fixed towers were not available, they are modeled as the Hardanger bridges towers. The towers are created in a local coordinate system making it easy to translate to the beginning and end of the main cable. The leg angle in y-z plane is generated by first degree polynomial function. The second leg is mirrored about the x-z plane, see figure 4.11. The pylon legs have a linearly varying cross section. This was modeled by each separate element in the leg had constant cross section but decaying for each element closer to the top of the pylon. The placement height and cross section of each horizontal beam are also input. The tower is given the same width as the floating towers at the top.

4.1.8 Component interaction

Since the geometry of the components described above were created separately, these have to be connected in a way that models the real world interaction. The ABAQUS function "*KINEMATIC COUPLING" was used, to specify which DOFs that would be constrained between a reference node and a surface. Table 4.2 shows which DOFs that are constrained between which sections.
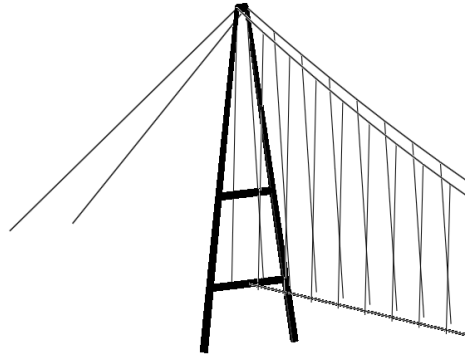
Figure 4.11: Fixed concrete tower based on the Hardanger bridge design

Table 4.2: Component interaction

Interacting components	Constrained DOFs
Girder-Fixed tower	x, y, z, θ_x, θ_y, θ_z
Girder-Floating tower	x, y, z, θ_x, θ_y, θ_z
Main cable - Towers	x, y, z
Pontoon - Tensionlegs	x, y, z
Connector nodes - Girder	x, y, z, θ_x, θ_y, θ_z

The rigid connections between the girder and the towers add stiffness to the system. A translation or rotation in a tower would directly result in corresponding movements in the girder. A displacement and rotational damper system has been suggested for the connection but is not considered here for simplicity. The cable saddles are not modeled but the main cables are free to rotate from the tower tops.

4.1.9 Boundary conditions

The boundary conditions set on the model are shown in Table 4.3.

In addition to the boundary conditions in Table 4.3 the floating towers were initially fixed in all directions and rotations, so the tensioning of the tethers and correct bouncy force could be applied. More about this in section 4.1.12.

Table 4.3: Boundary conditions on the model

Components	Constrained DOFs
Fixed Tower legs	x, y, z, θ_x, θ_y, θ_z
Side Cabels	x, y, z, θ_x, θ_y, θ_z
Tensionlegs at sea bed - Towers	x, y, z

4.1.10 Structural damping

Rayleigh damping was used for structural damping on the model. The complete model ran a frequency analysis and the two first eigenfrequencies where used to calculate the Rayleigh damping coefficients, α and β.

$$\beta = \frac{2\zeta}{\omega_i + \omega_j} \qquad\qquad \alpha = \omega_i \omega_j \beta$$

where ζ is the critical damping ratio, set to 0.005 here. The calculation resulted in $\alpha = 0.3076$ and $\beta = 0.008$

4.1.11 Environmental effects

The bridge concept in Bjørnafjorden is subjected to both varying wind and sea waves. To see environmental effects on the eigenfrequencies, both aerodynamic and hydrodynamic properties were added to the finite element model by applying *USER ELEMENTS. It was first attempted to use springs and dash pods, but ABAQUS did not give the option of coupling directional response (for the off diagonal terms in the added mass, damping, aerodynamic stiffness and damping matrices) so user elements were used instead. Three models were created for modal analyses

1. Only structural properties and the average buoyancy force were included. This model was the basis for all the other models. In the further this model will be refereed to as the structural model.

2. Two pontoon reference nodes were chosen and specified to apply the hydrodynamic added mass, damping and restoring forces. This was consistently chosen as the center of buoyancy, where the properties were added using the ABAQUS feature *USER ELEMENT. The user element does not have the option to specify damping. Hydrodynamic damping was added to the model by use of a wire element, connected to a fixed point in space, referred to as "ground" in ABAQUS. The wire elements

were assigned coupled damping coefficients of the added damping matrix for the given degrees of freedoms.

3. Structural, hydrodynamic and aerodynamic effects. Hydrodynamic effects were modeled as described in the hydro model. Aerodynamic damping- and stiffness were added to the girder nodes, the same way the corresponding hydrodynamic effects, added damping and restoring force, were added to the pontoon reference nodes with *USER ELEMENTS. The aerodynamic effects are given per unit length and was therefore multiplied with the girder element length. This model will further be referred to as the coupled model.

4.1.12   Loading the model

The model was put under load and final geometry was restored after deformations due to gravity in the steps described below. The steps listed below correspond to the steps performed in ABAQUS.

Initial Conditions: The complete geometry of the bridge was set up, with all material and cross sectional properties. BCs were added to the tension legs, side cables and fixed towers, and component interactions were put i place. The floating towers where also held in place by fixed translational and rotational BCs at the nodes in the pontoon reference node at each tower. The temperature on the whole model was set to 0.

Step 1, Pre- tensioning of main cables: A temperature change of -25 was set on the main cables to increase initial tension, because ABAQUS struggled to find a solution if gravity load was the fist loading step. This temperature was changed in step 3, so it would not affect the geometry, loading or stress on the final model.

Step 2, Gravity load: Gravity was added to all structural components of the model. The deformed shape of the girder and main cables was after this step sagging several meters below the desired geometry of the bridge.

Step 3, Temperature: A change in temperature was put on the main cables to restore the geometry to its initial shape. The temperature was different for each span to get the most accurate restored shape. It resulted in lifting the girder back up, close to its original position. The maximum deviation of the girder, from the perfect second degree curve to the deformed under gravity and restored with temperature, was 0.6m at about 200 meters from each of the fixed towers. This was considered acceptable for the purpose of frequency response analysis when considering the bridge length of 4155 meters The correct temperature of -260,-205 and -260 for each span respectfully was found by iteration. A temperature of -60.85 was also set on the tension legs calculated by Equation (4.1) to get the right tensioning of the tethers of 190MPa per tower.

$$\sigma = E\alpha\Delta T \qquad (4.1)$$

σ is the stress, E is youngs modulus and α material temperature coefficient.

Step 4, Removing BCs: The first three steps were run once. The force in the z-direction at the BCs on the floating towers were read from the resulting .dat file from ABAQUS. This force corresponded to the average buoyancy force at each tower, equal to the downward force from the tension legs and gravity load of the bridge. The BCs at the floating towers were replaced with a concentrated force in the vertical direction in the pontoon reference node node, representing the buoyancy force. The towers were then free to move.

Step 5, Frequency analysis: A modal frequency analysis was performed, giving the eigenfrequencies of the system and showing the eigenmodes in ABAQUS viewer. Output for node displacement and rotation of the girder nodes and the pontoon reference nodes were obtained, giving the eigenmodes, used for further analysis in MATLAB.

Step 6, Complex frequency analysis: The same was done as in step 5, but now the complex eigenvalues were collected, accounting for damping in the system.

4.2 Pontoon modeling

To model the fluid-structure interaction for the two pontoons, the proposed concept of a 4-legged steel floater from the TDA reports was used. The modeled draft for the given structure was 65 meters. When modelling the submerged floating structure, it was therefore only necessary to include the bottom 65 meters of the structure as shown in figure 3.3. The frequency dependent added mass, added damping, hydrodynamic restoring force and the transfer function of the wave exciting forces was numerically obtained using the hydrodynamic analysis software WADAM, integrated in HydroD. A computer-aided drawing (CAD) with finite element properties was input, created using the software GeniE. As the pontoons were double symmetric, $1/4^{th}$ of the model could be created and mirrored as a part of the panel FEM method used in HydroD/WADAM.

4.2.1 Modeling in GeniE

From the drawings from figure 3.3, the center-to-center distance for the elliptical legs were 60 meters in the x-direction and 81 meters in y-direction. TDA proposed a constant diameter of 15 meter for the tilted circular steel legs, and were connected to the bottom frame, consisting of 4 parallelepiped (3D- paralellogram) crossers in x- and y-direction as one can see in figure 4.12. Both the crosser panels and the circular legs were tilted. The crosser panels were tilted towards, in either the zx- or yz-plane, while the cross sectional circular legs were tilted in three-dimensions as shown in figure 4.12.

The model was created using guiding planes in GeniE. This technique is simply to create drawings on 2D planes with defined grids and sweep shell elements between 1- and 2D lines to obtain 3D-shell-like structures. Using boolean operations and creating intersecting geometries followed by deleting the unwanted parts caused errors and geometrical discon-
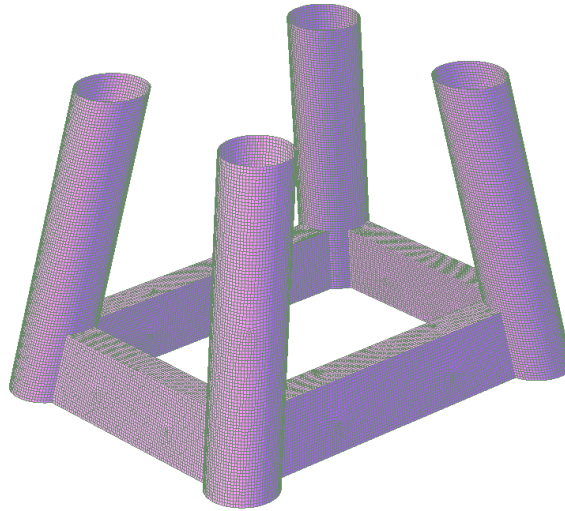
Figure 4.12: Full CAD model of the pontoons, extracted from HydroD

tinuities in the model and was therefore avoided. Using guiding planes resulted also in a good mesh using the mesh generator in GeniE.

As the legs were drawn with a constant diameter of 15 meters in figure 3.3 and the modeling technique was using guiding planes, it became necessary to draw ellipses in the xy plane. The ellipses corresponded to the projection of the cross section of the legs in the x-y plane at three z plane heights. The leg shell was created by sweeping through the ellipses. Two planes were created to obtain the tilted crosser panels at (z=0 and z=15).

Design assumptions

The designed model was based on the data given in figure 3.3. Where the drawing was insufficiently accurate design assumpions were made. Figure 4.13 and 4.14 illustrate the design assumptions in detail.

Ellipses were drawn on the guiding planes and the necessary calculations for rotating the ellipses about the vertical axis and obtaining the major diameter is evident in the right sub figure in figure 4.13. The rotational angle was obtained by finding the x- and y-direction distance from the leg center in xy-plane (elliptical center) for the leg at z=0 and z=65 meters; obtaining 8.5 and 11.9 meters as shown in the left sub figure of figure 4.14.

Creating the FEM-file

The GeniE-model consisted of $1/4^{th}$ of the final geometry, with meshed shells of the structure. After the geometry was made, the wet surface was to be defined. The wet surface would be the whole outer surface of the created structure as the draft was 65 meters. As GeniE does not allow meshes with more than 15000 elements, the mesh size 0.63 meters was chosen, giving 14900 elements. Different mesh sizes were however also tested and
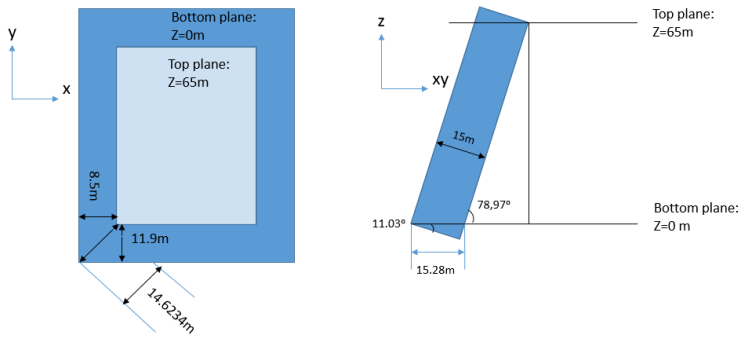
Figure 4.13: Pontoon design, bottom plane
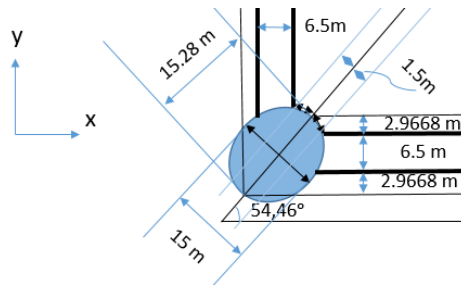
Figure 4.14: Pontoon design, bottom plane

convergence was seen by plotting added mass coefficients wrt. frequency for mesh sizes of 0.63, 1, 1,2 and 2 with 25 frequencies from 0.2 to 5 rad/s as shown in figure 4.15 for the results that were to be obtained. Convergence for these results meant that the FEM model was valid and viable for further analysis. The convergence test was done for a vertical DOF. Dummy hydrodynamic pressure was then applied on the meshed wet surface. The hydrodynamic pressure was necessary for a hydrodynamic analysis in HydroD where a panel FE-model would be used.
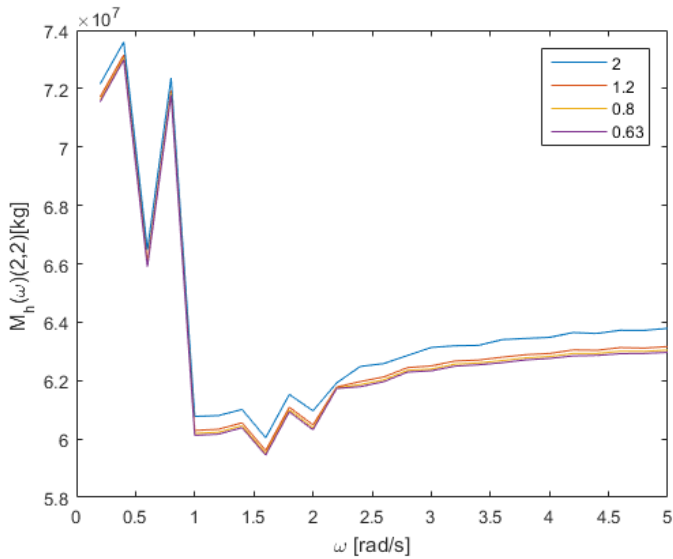
Figure 4.15: M_{h22}

4.2.2 Hydrodynamic analysis in WADAM

In HydroD, the hydrostatic and hydrodynamic forces were to be calculated in frequency domain for different directions and frequencies using the sub program WADAM. In WADAM, a panel method was used, exploiting the dummy hydrodynamic pressure and the mesh for a hydrodynamic FE method using linear potential theory. The panel method will be used in WADAM for numerical execution of the linear potential theory shown in section 2.2.

The wave frequencies were defined from 0.02-6 rad/s with a 0.02 rad/s step between 0.02 and 3.6 and a 0.04 rad/s between 3.64 and 6 rad/s; with 240 frequencies in total. Wave directions were chosen from 0-90 degrees with a 5 degrees increment. The model had a direction such that 0 corresponded to a direction parallel to the x-axis (corresponding to the global x-axis of the ABAQUS model). 90 degrees would accordingly mean a force parallel to the y-axis. The water depth was defined to be 550 meters, as is for the tower position with the deepest water beneath. Test analyses showed that the difference in water depth under the two towers ($550m - 450m = 100m$) had no impact on the obtained results.

HydroD through WADAM found the center of buoyancy (COB) given a defined water line relative to the figure. As the whole hydrodynamic model in figure 4.12 was modeled as the part submerged under water, the water line was defined at the very top of the structure. The Center of buoyancy could then be calculated in WADAM. The COB-position was used as a user-specified motion reference position with 6 DOFs representing 3 translational and 3 rotational DOFs. The position of this node would be used consistently for the total bridge model and is referred to as pontoon reference node. Added mass and hydrodynamic

damping, were as known from potential theory frequency dependent. The restoring force was dependent on the area in water plane and the submerged surface. Wave excitation forces included the force due to frequency dependent incidential waves, and would be both wave frequency and directional dependent. As of data described in this section, the results would give 240 results for frequencies and for the hydrodynamic damping and added mass and $[6 \times 72 \times 240]$ results for the wave transfer function. The output from WADAM was a text file, so a MATLAB script was created extract the matrices.

4.3 Environmental modeling

Standards for environmental load modeling [1], recommends environmental measurements for key parameters over 20 years for long term analyses. As Bjornafjorden is a new bridge concept, it has a limited amount of measurements for modeling the coupled environmental loads with a longer return periods or extreme responses. From the engineering reports [11] and [10], environmental data for wind is taken from SINTEF, "Bridge across Bjørnafjorden Metaocean conditions, version 2". The engineering reports from TDA in [11] and [10] refer moreover to the DNV Recommended Practices as references, e.g DNV RP-C205 that is frequently used for ocean-based structures.

TDA has however assembled sea states with 100 year return period, a 100 year mean wind velocity and a coupled extreme response for a coupled 100 year return period environmental loading (wind and wave), using environmental contours, as mentioned briefly in [10]. If one is to assume that industry methods from e.g the RP-C205 have been used, it seems that the DNV models for long-term distributions of key parameters such as H_s and V_{mean} and then joint probability distributions of these have been used to obtain the environmental contours.

In the TDA reports, environmental data were used to apply environmental loads on the modeled bridge for a dynamic response analysis. Of the data TDA have gathered, the extreme response from 100 year return period environmental loading has been used for the modeled bridge.

4.3.1 Chosen parameters

By using relations from section 2.2 about wave theory, the environmental conditions in figure 4.4 are directly related to the short-term stationary environmental conditions. This means that these data can be used as direct inputs for chosen spectra of direction, auto-spectral density for wave elevation and for aerodynamic load analysis of the bridge in frequency domain. To simplify the environmental model, tidal levels and current speed have been negliged and wave- and wind direction directed towards the same direction. for a $\cos^{2s}$-directional spectrum.

An auto-spectral wave elevation spectrum should reflect the energy content of wave heights

wrt. frequencies in a ocean location. Lack of data and no suggestions of an auto-elevation spectrum has lead to choosing the one-parametric Pierson-Moskowitz spectrum, not accounting for swell. Moreover, the directional distribution function is not same as the one recommended by RP-C205 that is used in the engineering reports. The $\cos^{2s}$-distribution was used instead, as it was convenient.

Environmental load 100 year return period	
U_{mean}	29 [m/s]
Wind and wave direction	West, 90° to girder
$H_s[m]$	3.75
Crest length parameter s	5

Table 4.4: Chosen environmental parameters

Chapter 5

Numerical Analysis

Generalized procedures for obtaining modal analysis, response analysis and for motion induced instability of a multi-span suspension bridge with floating towers have been created [4]. The procedures will account for hydrodynamic and aerodynamic coupling with a structure. Three flowcharts have been made for this purpose, in Figures 5.1, 5.2 and 5.6. These procedures assume the use of buffeting theory to obtain wind forces, accounting only for wind forces on the girder, and linear wave potential theory for properties for fluid-structure interaction.

A case study is then considered for the Bjørnafjorden bridge model to apply the generalized assumptions for both a coupled modal analysis, response and for motion induced instabilities. The flowcharts related to the modal analysis can be converted to a MATLAB script running ABAQUS iteratively for frequencies and solving the complex eigenvalue problem, when iterating to obtain converged eigenvalues. Another MATLAB procedure will follow the flowchart in 5.2 created to modalize and couple the load contributions with the structure and to obtain the spectral response of the bridge. 5.6 will search for the lowest mean wind velocity that will govern self excited instabilities.

5.1 Generalized method for modal analysis of a coupled system

As the environmental terms for mass, damping and stiffness are frequency dependent, an iterative procedure is necessary for conducting the modal analysis of a coupled model. Frequency dependent hydrodynamic added mass, damping and restoring forces in addition to velocity- and frequency dependent aerodynamic damping and stiffness need to be considered. Accordingly, a modal analysis has to be made such that the corresponding fre-

quencies of the given environmental terms will correspond to an eigenfrequency solution. The iterative procedure would require a fixed mean wind velocity.

The step by step iterative procedure can be described in a flowchart as in 5.1. Hydrodynamic and aerodynmic environmental effects are found for an initial guess of frequency ω. The procedure was made for the Bjørnafjorden case, and requires a program such as MATLAB to generate frequency dependent mass and stiffness terms to the user defined elements in ABAQUS as referred to in the previous chapter. Damping would be added using the technique of using wire elements as mentioned in the previous chapter for modelling.
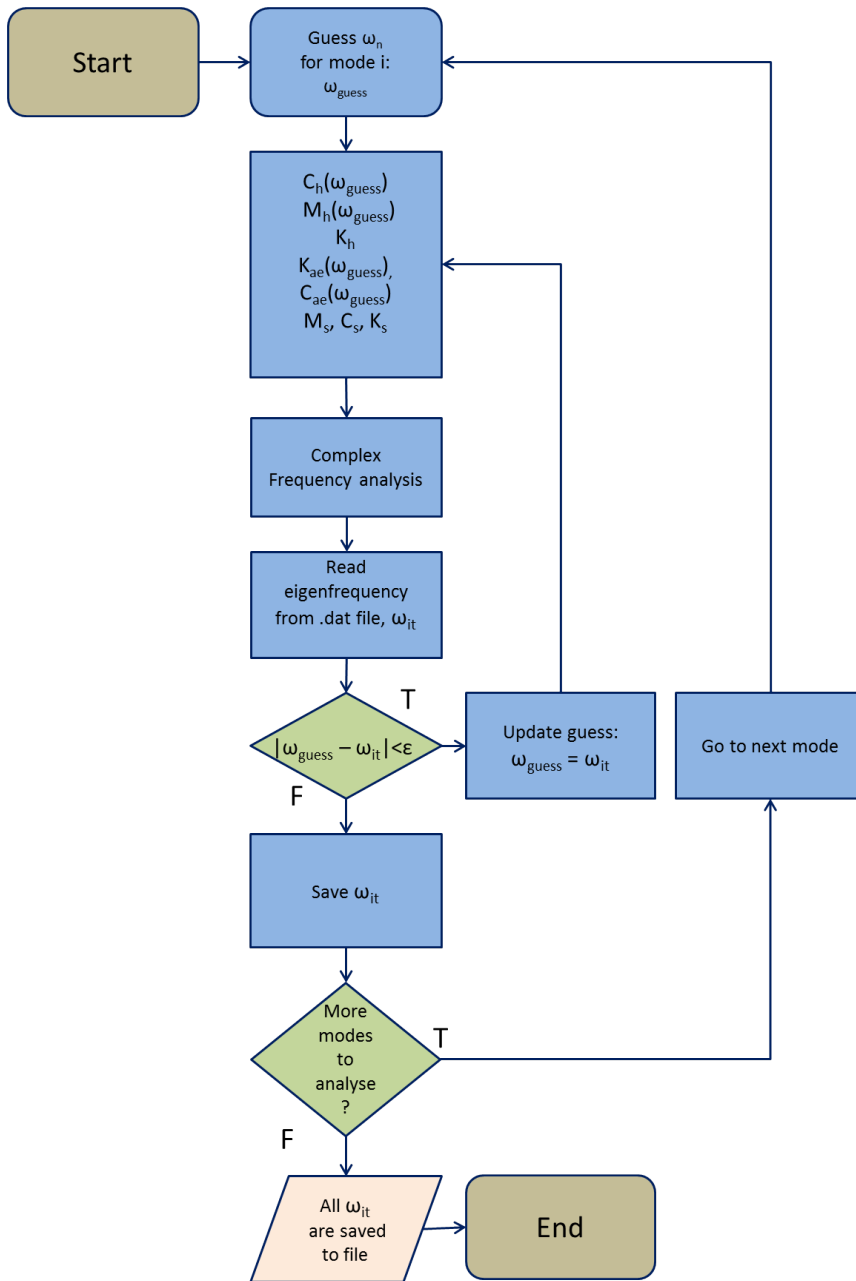
Figure 5.1: Algorithm for obtaining ω_n when accounting for hydrodynamic and aerodynamic effects

5.1.1 Generalized method for response analysis

The flowchart in Figure 5.2 shows a generalized procedure for calculating the spectral response of a bridge subjected to wind and wave load. The boxes in the flowchart are numbered and will be referred to in the following

The procedure uses input from a FE model analysis, $\Phi, \omega, \tilde{M}$, as shown in box number (1). Hydrodynamic mass, damping and restoring forces from a hydrodynamic analysis program and aerodynamic stiffness and damping terms should be obtained from aerodynamic derivatives from conducted wind tunnel testing, assuming buffeting theory (6)

The flow induced forces are determined statistically based on measurements at the site. The procedure assumes coupling of aerodynamic buffeting theory and linear wave theory in frequency domain in modal coordinates. The analysis depends on auto correlation spectra for wave elevation, directional spectrum and reasonable buffeting coefficients and aerodynamic derivatives given from wind tunnel testing.

1. Where the subscript notation s denotes structural, the eigenmodes $\mathbf{\Phi_s}$, eigenfrequencies $\omega_\mathbf{s}$, and modal mass $\tilde{\mathbf{M}}_\mathbf{s}$, are the result of a modal analysis in a finite element software. $\mathbf{\Phi}_s$ includes the modes from the girder, $\mathbf{\Phi}_G$, and k pontoons so that $\mathbf{\Phi} = [\mathbf{\Phi}_G \mathbf{\Phi}_C]$ and $\mathbf{\Phi}_C = [\phi_{C,1}, \phi_{C,2}, ...\phi_{C,k}]$.

2. $\tilde{\mathbf{K}}_s$ can often be obtained as a relation of $\tilde{\mathbf{M}}_s$ and ω while $\tilde{\mathbf{C}}_s$ can be calculated using the critical damping factor ζ, modal mass and frequency.

3. Hydrodynamic added mass, damping and restoring forces are obtained through a hydrodynamic analysis using linear potential theory, for frequency domain. The pontoon numbers are in the figure denoted k, where k=(1,2,3,$n_{Pontoons}$). Two pontoons would give k=2.

4. $\mathbf{M}_k$, $\mathbf{C}_k$ and $\mathbf{K}_k$ are modalized for each pontoon k using the obtained pontoon eigenvectors $\Phi_{C,k}$, for the different pontoon reference nodes.

5. The modal contributions from $\tilde{\mathbf{M}}_k$, $\tilde{\mathbf{C}}_k$ and $\tilde{\mathbf{K}}_s$ from the pontoons and can be added together to account for the hydrodynamic mass, damping and restoring force in the pontoons.

6. By applying buffeting theory and assuming a line-like structure, the wind velocity and frequency dependent $\mathbf{K}_{ae}(\omega, V)$ and $\mathbf{C}_{ae}(\omega, V)$ can be obtained using aerodynamic derivatives from conducted wind tunnel testings for a given bridge section.

7. The aerodynamic derivatives are defined for each unit length. Modalizing and integrating $\mathbf{K}_{ae}(\omega, V)$ and $\mathbf{C}_{ae}(\omega, V)$ over the longitudinal girder distance the total contribution of modal motion induced aerodynamic $\tilde{\mathbf{K}}_{ae}$ and $\tilde{\mathbf{C}}_{ae}$ are obtained.

8. The wave transfer function $Q_r(\omega, \theta)$ for a submerged pontoon can be obtained from the same hydrodynamic analysis by using linear potential wave theory.
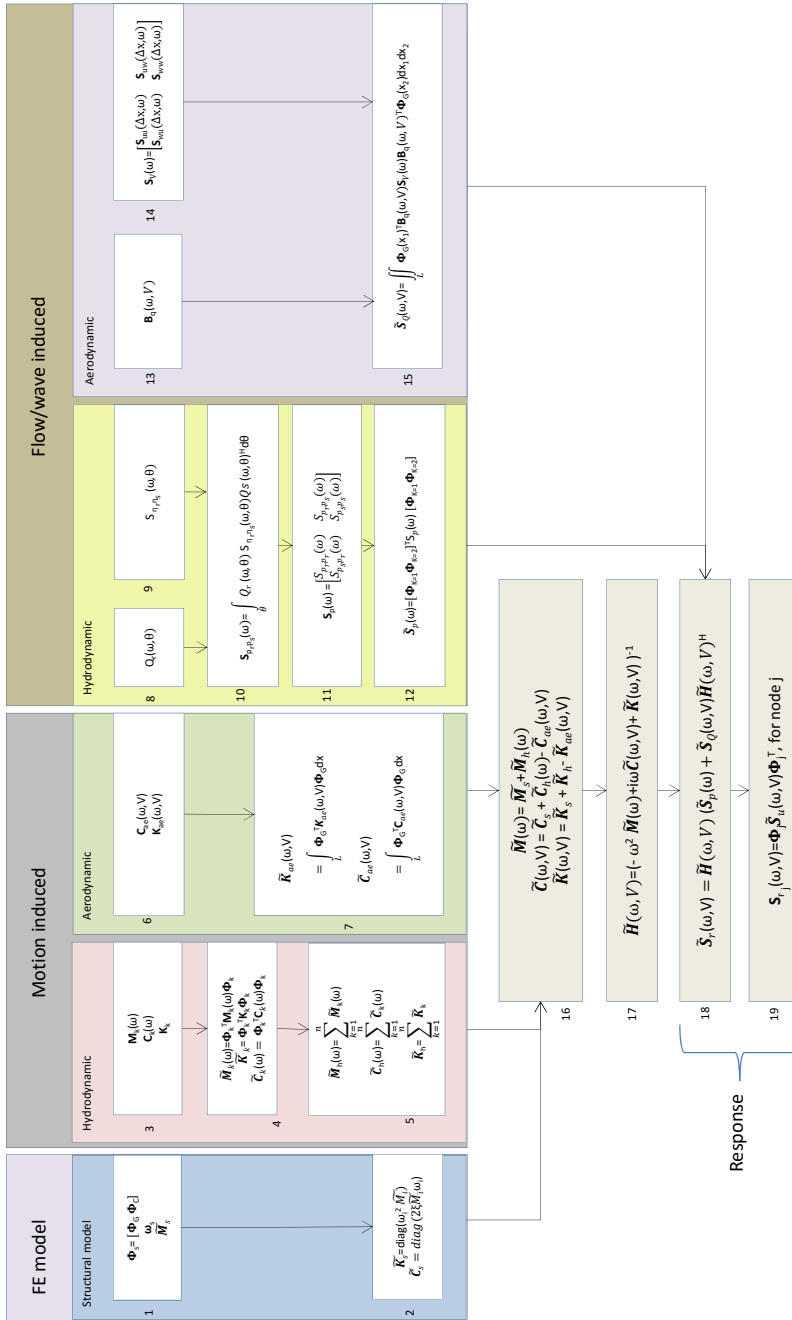
Figure 5.2: The flow chart shows how the spectral response is calculated

9. An expression for the cross spectral density function $S_{\eta_r \eta_s}(\theta, \omega)$ is either the auto- or cross spectral density of wave elevation. If cross correlation is not considered, the expression will be equivalent with e.g $S_{\eta_r \eta_r}(\theta, \omega) = S_{\eta_r \eta_r}(\omega) \cdot D(\theta)$. Accounting for cross correlation between pontoons, the relation $D(\theta)$ is nonetheless composed of auto-spectral density function $S_{\eta\eta}$, and Equation 2.26 from theory Section 2.2. Stationary input for this function will be e.g stationary inputs H_s, mean wave direction θ_0; depending on the chosen wave models for direction and wave elevation.

10. The wave force spectra are developed using the relation that wave transfer function from potential theory times wave amplitude gives wave force in frequency domain. The relation between spectral process and spectral density, integrated over the angles gives the wave force as in equation (10) in the flowchart.

11. If cross correlation is considered and 6 DOFs are taken into account for each tower, a three dimensional matrix with $[6 \cdot n_{towers} \times 6 \cdot n_{towers}]$ wrt. frequencies will be assembled.

12. The modal transfer function is obtained by using cross multiplication of the set of eigenmodes to the cross correlation spectrum for wave force elevation.

13. From buffeting theory, the buffeting matrix $\mathbf{B}_q$ contains the cross sectional and velocity dependent coefficients in frequency domain.

14. The cross spectral density function is established for wind velocity for transversal and vertical fluctuating wind $\mathbf{v} = [u \quad w]$, based on measurements at site.

15. The modal wind force spectrum is obtained by integrating twice over the length of the girder to account for correlation between points on the girder. The modal contributions are added together using the double integral.

16. All the modal contributions for mass, damping and stiffness in the system are added together using correct signs.

17. The modal transfer function of the whole system is obtained from total $\tilde{\mathbf{M}}$, $\tilde{\mathbf{C}}$ and $\tilde{\mathbf{K}}$.

18. Recalling theory, spectral process of force times transfer function gives the response. The spectral response is calculated in frequency domain by adding up the modal contributions of spectral forces and multiplying with the pair of the modal transfer function and the Hermittian conjugate of the modal transfer function.

19. The response in real coordinates can be obtained by de-modalizing the spectral response with the eigenfrequency matrix for a specific node.

Table 5.1: Input parameters

Input parameters	Value range
Wave angles θ	[5:5:360] degrees
Wave frequencies ω_w	$\{[0.02:0.02:3.6],[3.64:0.04:6]\}$ rad/s
Interpolated frequencies ω	[0:0.006:6] rad/s
Specified number of modes	70

5.2 Case: Dynamic response in frequency domain for the Bjørnafjorden bridge

A coupled dynamic frequency domain response analysis was created in MATLAB by using a case study for the Hardanger bridge [13] to obtain the aerodynamic damping and stiffness as well as the buffeting forces. The scripts calculating the aerodynamic theory was solely based on this, including the wind field velocity spectrum for the Hardanger Bridge site. The hydrodynamic mass, damping, restoring force and wave transfer function were calculated in HydroD/WADAM, assuming linear potential theory. Output from a modal analysis of the modeled ABAQUS bridge without environmental properties from chapter 4 would then be used to modalize the system and to obtain the modal system matrices. Input for generating response would be V_{mean}, significant wave height H_s. mean wave direction θ_0 and crest length s, given cos^{2s} directional spectrum, and the one-parametric Pierson-Moskowitz spectrum. Table 5.1 shows input parameters for the model. *Interpolated frequencies* is the frequency interval accounting for 1000 frequencies between 0 and 6 and is the chosen frequency axis. The response analysis was conducted using the first 70 modes.

5.2.1 Modal analysis for a coupled system

The parameters for (1) was obtained from the ABAQUS model described in section 4.1. The ABAQUS model was set up in three different ways. The first accounted only for structural components, the second for structural and hydrodynamic contributions and the third for structural, hydrodynamic and aerodynamic contributions. For all three cases the model returned 70 eigenvalues. ABAQUS' output was a text file (.dat file) so a MATLAB script was created to read the text file and collect the data in matrices, for further use.

Structural model

The structural finite element bridge was modeled as described in section 4.1. No environmental effects were added to the model except a static buoyancy force. This model also

returned 70 generalized masses ($\tilde{\mathbf{M}}$), 70 eigenmodes for the girder and 70 eigenmodes for the two pontoons, respectfully.

$\tilde{\mathbf{C}}$ and $\tilde{\mathbf{K}}$ was not returned from ABAQUS. Since $\tilde{\mathbf{M}}$ is a diagonal matrix and the effects of damping on the eigenfrequencies are assumed negligible the following expression was used to obtain the diagonal matrices $\tilde{\mathbf{K}}$ and $\tilde{\mathbf{C}}$.

$$\tilde{K} = diag(\omega_i^2 \tilde{M}_i) \tag{5.1}$$
$$\tilde{C} = diag(2\tilde{M}_i \omega_i \zeta_i) \tag{5.2}$$

where ζ is the eigenfrequency dependent critical damping ratio. ζ was set to 0.005 for all modes in this calculation.

Coupled model

The iteration procedure for modal analysis of the coupled system was carried out as following in the MATLAB procedure; following the procedures of the generalized method displayed in 5.1.

An initial frequency guess corresponding to the first eigenfrequency of the structural model was used and denoted ω_{guess}. Added damping and added mass matrices for frequencies $[0.02 : 0.02 : 3.6]$ and $[3.64 : 0.04 : 6.00]$ was obtained from HydroD. Because $\mathbf{C}_h$ and $\mathbf{M}_h$ matrices were for discrete frequencies, the matrices were linearly interpolated to get more exact values for ω_{guess}. A MATLAB function calculated the $\mathbf{K}_{ae}$ and $\mathbf{C}_{ae}$ for ω_{guess}, from the mean wind velocity and curve fitted aerodynamic derivatives from the Hardanger bridge. The mean wind velocity was set to 40 m/s so the effects of the aerodynamic contributions would be significant. A complex eigenfrequency analysis was run in ABAQUS and returned a resulting .dat file. ω_{it} was read from the .dat file only for the specific mode. When $|\omega_{it} - \omega_{guess}|$ is equal to or smaller than the tolerance value, denoted $\epsilon = 0.001$, ω_{it} had converged. ω_{it} was updated as the next eigenfrequency and the next mode would be handled. If the absolute difference was larger than ϵ, the iteration would continue. No more than two iterations were usually necessary for each mode. When all 70 modes had ran through the 70 complex eigenvalues were saved to file. The process took approximately 10 hours.

The complex eigenmodes accounting for the environmental damping effects were difficult to obtain from the ABAQUS. This is left for further work.

5.2.2 Motion induced hydrodynamic forces

The hydrodynamic added mass, damping and restoring forces were obtained from HydroD/WADAM based on linear potential theory using panel method of a FE-model cre-

ated in GeniE. The frequency dependent added mass and damping were simulated for 240 wave frequencies between 0.02 and 6 rad/s. To make these matrices adaptable for more frequencies, a linear interpolation was made to obtain added mass and damping for 1000 frequencies rather than 240. The three motion induced terms were modalized using structural eigenvectors for the pontoons. The modalized terms were subsequently added together for each pontoon to account for two towers in the modal formulation.

5.2.3 Motion induced aerodynamic forces

Aerodynamic contributions on the model (6), was only accounted for on the girders, not on the towers or cables. Aerodynamic derivatives were obtained from conducted wind tunnel tests of the Hardanger bridge girder section. 18 derivatives for 21 discrete reduced velocities, for the range $[0.5411 : 4.429]$, were curve-fitted such that an analytical function was obtained, applicable for all reduced velocities within the range. Plots of $\tilde{\mathbf{C}}_{ae]}$ and $\hat{K}_{ae}$ are found in the appendix (C.4 C.5).

In (7) the integration was done numerically, because Φ_G is node wise discrete, by first modalizing $\tilde{C}_{ae]}$ and $\tilde{K}_{ae}$ at node $1...N$. This resulted in $[N_{mod} \times N_{mod}]$ matrix for one node. The node by node modal $\tilde{\mathbf{C}}_{ae}$ and $\tilde{\mathbf{K}}_{ae}$ matrices where then multiplied with the length between the nodes, Δx and then added together to obtain $\tilde{\mathbf{K}}_{ae}$ and $\tilde{\mathbf{C}}_{ae}$.

5.2.4 Flow induced hydrodynamic forces

The hydrodynamic wave transfer function (8) was obtained in HydroD for 240 frequencies and 72 angles. The transfer function in tower 1 was set equal to the transfer function at tower two. The 100 meter difference from 550 to 450 meters in water depth made no difference for the transfer function coefficients. As 1/4th of the double-symmetric FE-model was created, 18 angles were simulated for, and the wave transfer function values were assembled for 72 angles; exploiting the double-symmetry of the structure. This saved computation time. Surface plots of these are given in the appendix. The function for the cross spectral density for wave elevation, S_η, with derivation and equation as shown in Equation (2.26) in the wave theory section. Directionality and wave elevation are assumed statistically independent, so the auto-spectral density function can be multiplied with the one-parametric Pierson Moskowitz spectrum and the $\cos^{2s}$ directionality function for the wave frequencies.

The cross correlation function for wave elevation was applied to the case of having two submerged floating towers for Bjørnafjorden[4]. The wave transfer function and the spectral density functions accounted for wave elevation at two towers, the spectral forces $S_{p_r p_s}$ could accordingly be calculated. The expression from Equation (2.26) integrates over wave directions θ. As the water depth of Bjørnafjorden for 450 and 550 meters for each of the respective towers can be considered deep, the wave number $\kappa = \frac{\omega|\omega|}{g}$. The numerical procedure is described briefly

Numerically, the wave transfer function Q for each θ_n and ω becomes a $[6 \times 1]$ vector, as 6 DOFs were accounted for. S_η is a $[1 \times N_\theta]$-vector, while the complex conjugate of Q becomes a $[6 \times 1]$ vector. The numerical integral is carried out by adding the each resulting $[6 \times 6]$ matrix multiplied by the angular step 5, for all frequencies along a dimension representing the angular dependency of S_{η_r, η_s}. The wave force spectrum for each ω and θ at positions r and s could be expressed as follows.

$$S_{P_r P_s}(\omega, \theta_n) = \mathbf{Q}_r(\omega, \theta_n) \mathbf{S}_\eta(\omega) \cdot D(\theta_n) \cdot \exp\left(G(\omega)\right) \mathbf{Q}_s(\omega, \theta_n)^H$$

Where G is the content in the exponential of equation of the cross correlating wave spectral density function from Equation (2.26)

$$G(\omega) = -i\frac{\omega|\omega|}{g}(\Delta x \cos\theta + \Delta y \sin\theta)$$

Such that

$$S_{P_r P_s} = \sum_{n=1}^{N_\theta} S_{P_r P_s}(\omega, \theta_n) d\theta$$

For the Bjornafjorden bridge, Δy will be 0 as the bridge is assumed to be aligned with the defined x-axis. Δx is the distance between the towers in x-direction and will be zero for the auto spectral terms S_{η_r, η_r} and S_{η_s, η_s}, the auto spectral relations for each tower, but equal the span length, $\Delta x = 1385$ for the cross spectral terms.

The wave force spectra was numerically integrated by multiplying pairs of wave transfer function, where one is complex conjugate, with a unit of $S_{\eta\eta}(\omega, \theta)$ for a corresponding θ, multiplied with the unit angle. As the Δx and Δy were integrated in the formulation of spatial point correlation for wave elevation, there would be 4 sets of cross/auto spectral density $[6 \times 6]$ matrices for the wave force (11). Since $Q_r = Q_s$ it follows that the auto spectral density for each tower will be equal each other and same for the two cross spectral densities, i.e $S_{p_r p_r} = S_{p_s p_s}$, and $S_{p_r p_s} = S_{p_s p_r}$.

A plot for the wave load spectrum was obtained, consisting of $[12 \times 12]$ matrix coefficients wrt. frequencies; accounting for cross correlation between towers and degrees of freedoms. The real values were plotted of stationary parameters of $H_s = 3.75$ and $H_s = 6m$ at s=5. These two significant wave heights are to be considered very conservative.

The spectral wave force peaks account for peak frequencies from the Pierson Moskowitz spectrum as well as the frequency dependent wave transfer functions obtained from Hy-droD. A general trend in the curve in Figure 5.3 is higher amplitudes for lower frequencies when H_s is bigger. The peak frequencies reside between 0.5 and 1.2 for most degrees of freedoms.
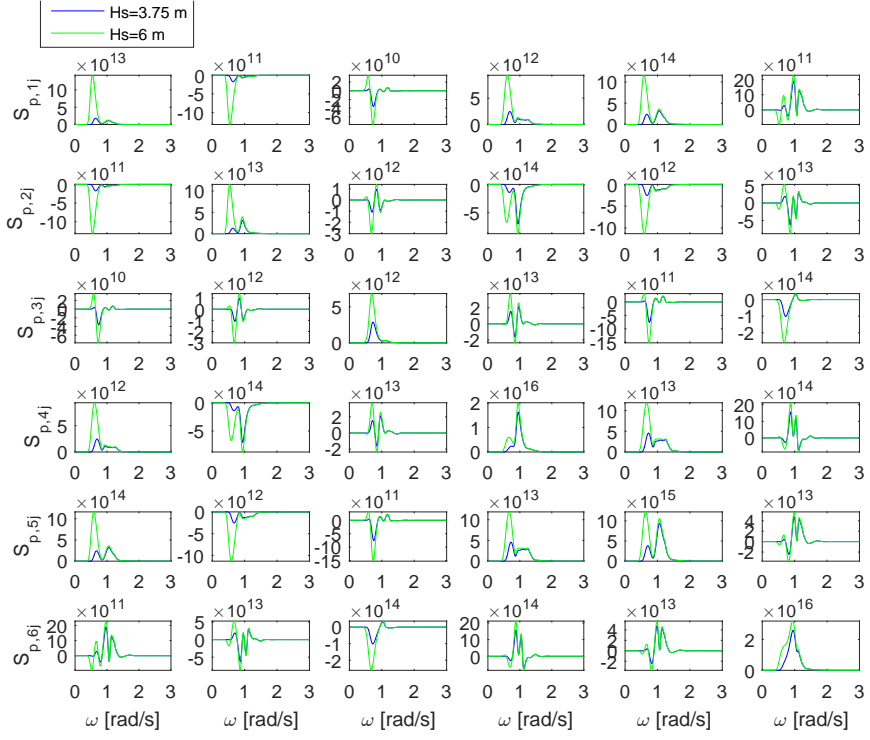
Figure 5.3: Hydrodynamic force spectrum for tower 1 for $H_s = 3.75$ and $H_s = 6$

$$\tilde{\mathbf{S}}_{p_r p_s}(\omega) = [\Phi_{C_r} \Phi_{C_s}]^T \begin{bmatrix} \mathbf{S}_{p_r p_r}(\omega) & \mathbf{S}_{p_r p_s}(\omega) \\ \mathbf{S}_{p_s p_r}(\omega) & \mathbf{S}_{p_s p_s}(\omega) \end{bmatrix} [\Phi_{C_r} \Phi_{C_s}] \qquad (5.3)$$

In the given equation, equivalent to (12) $\Phi_C k$ are the eigenvectors for the tower reference nodes of each tower. This would mean that the cross spectral terms were modalized using two different eigenmodes corresponding to tower reference node in position r and s. Plotting the cross-correlational coefficients between towers wrt. frequencies gave oscillating values with equal amplitudes in positive and negative amplitudes around zero, which were assumed to imply noise. Correlation could accordingly be assumed low for the given crest length.

5.2.5 Flow induced aerodynamic forces

Buffeting forces are modeled to only act on the girder. To obtain the buffeting forces matrix, Equation (2.76) was used, where $\mathbf{B}_q$ is dependent on mean wind velocity, cross section and oscillating frequency of the girder through admittance functions. [13]

Stationary wind conditions were taken into account for the flow induced wind force (14). Relations from a case study [13] of the Hardanger bridge were used to calculate the auto- and cross spectral density for the translative and vertical wind velocity

$$S_{uu}(\omega) = \frac{40.58Vz\kappa}{(1 + 9.74\omega z/V)^{5/3}} \exp\left(-1.4\frac{\Delta x\omega}{V}\right) \tag{5.4}$$

$$S_{ww}(\omega) = \frac{0.82Vz\kappa}{(1 + 0.79\omega z/V)^{5/3}} \exp\left(-1.4\frac{\Delta x\omega}{V}\right) \tag{5.5}$$

$$S_{uw}(\omega) = -\frac{2.23Vz\kappa}{1 + 1.67\omega z/V)^{7/3}} \exp\left(-1.4\frac{\Delta x\omega}{V}\right) \tag{5.6}$$

Assuming turbulence intensities and roughness of the Hardanger bridge site to be applicable for Bjørnafjorden. κ is the roughness coefficient assumed to be 0.0031.

(a) S_{uu} (b) S_{uw2}

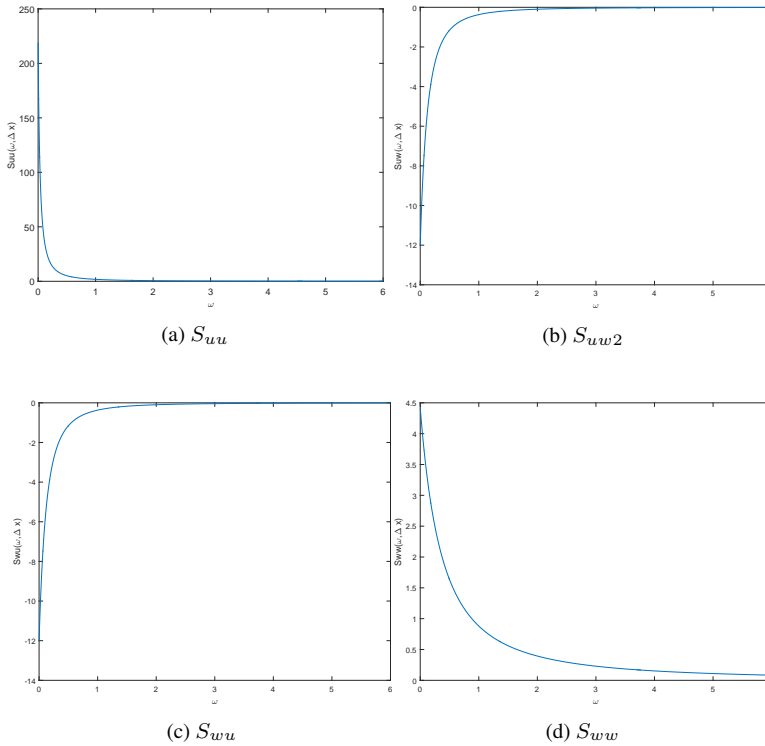(c) S_{wu} (d) S_{ww}

Figure 5.4: Auto- and cross spectral wind spectrum for horizontal and vertical wind direction on girder

The modal spectral wind forces, $\tilde{\mathbf{S}}_Q(\omega, V)$ were obtained by multiplying the cross spectral

wind densities with the buffeting matrices.These were again modalized, and the modal contributions were added up and assembled along the girder. The plotted wind velocity spectrum, using case data of the wind spectrum wrt. frequencies and for a wind velocity of 29 m/s gave the following wind spectrum as shown in Figure 5.4.

It is evident that the cross spectral functions of the wind velocity spectra have an exponential trend for both the cross- and auto-spectral density functions. S_{wu} is equal to S_{uw}, where the trend is an exponential growth, while the trend shows exponential stagnation for the auto-spectral functions wrt. frequencies. Very dominant values for S_{uu}, makes it reasonable to assume a similar decaying wind load spectrum.

$$\tilde{S}_Q(\omega) = \int_L \int_L \phi_{G_i}^T(x_1) B_q(\omega, V) S_v B_q(\omega, V)(\omega)^T \phi_{G_j}(x_2) dx_1 dx_2 \qquad (5.7)$$

$\phi_{G_{i,j}}$ becomes the eigenvector for each girder node i and j.

5.2.6   Transfer functions

As all the motion induced components were modalized, the modal components could be added together for respectively mass, damping and stiffness and the modal transfer function could be obtained. In an attempt of identifying eigenfrequencies, the absolute value of all modal transfer function coefficients were summed up to be one scalar for each frequency ω.

By plotting the sum of coefficients of the modal transfer function for all the mode $\times$ mode-coefficients, one could get a notion of which frequencies would govern the responses; i.e the eigenfrequencies. The figure, 5.5 shows the plot of sum of absolute values of modal coefficients including structural, hydrodynamic and aerodynamic motion induced forces wrt. frequencies against the same plot with modal coefficients only related to the structural coefficients.

If assuming that peak frequencies in the plot represent the eigenfrequencies with corresponding eigenmodes that will excite the highest response, general observations show that many of the first eigenfrequencies are shifted towards lower frequencies for a mean wind of 29 m/s.
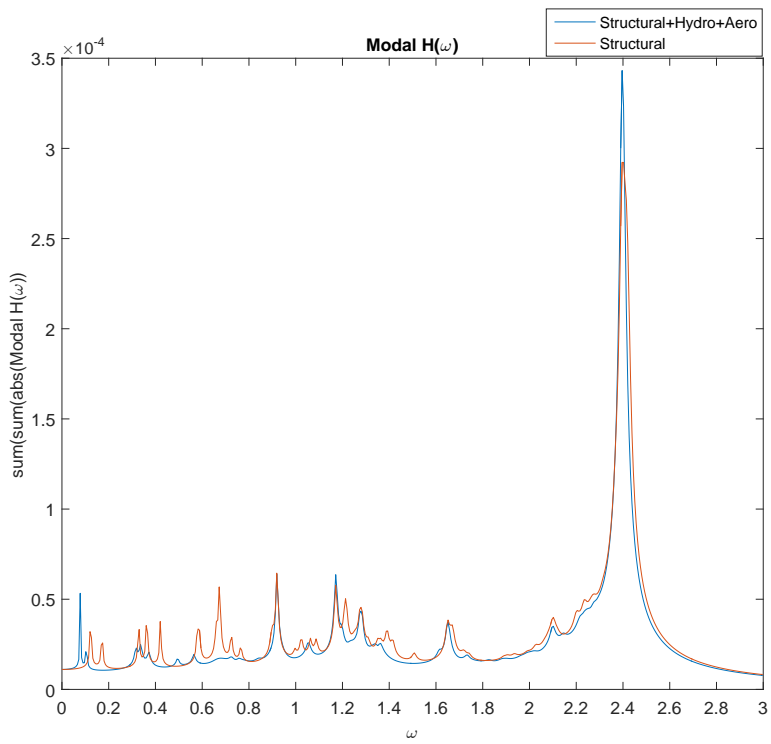
Figure 5.5: Absolute value of all modal Transfer functions

5.2.7 Response

The modal response spectrum was then obtained by adding together the two modal spectral force distributions multiplied the total modal transfer function (18). Demodalizing the spectral response could give the spectral response in the wanted nodes for e.g a specific eigenvector for a specific node (19).

$$\tilde{S}_r(\omega, V, H_s) = \tilde{H}(\omega, V) \cdot \left(\tilde{S}_Q(\omega, V) + \tilde{S}_P(\omega, H_s) \right) \tilde{H}(\omega, V)^H \qquad (5.8)$$

The MATLAB script generates response for short term stationary conditions, where H_s, s and the mean wave direction would define the stationary sea conditions, and the mean wind V. The cross-spectral density function for wave elevation $S_{\eta_r \eta_s}$ has been decomposed such that $S_{\eta\eta}$ and $D(\theta)$ with its stationary parameters H_s and s are input. The MATLAB script will use these parameters as input for the function.

5.3 Motion induced instability

Motion induced instability will be investigated for, on the modeled bridge. The procedure was based on the theory given in Section 2.3.4 from theory. MATLAB scripts developed for the Hardanger bridge (by Ole Øiseth) were further developed to account for frequency dependent hydrodynamic effects. The iterative process is described in the flowchart in Figure 5.6 to also account for the coupling of mass, damping and stiffness contributions from frequency dependent hydrodynamic and aerodynamic terms.

Obtaining instability limits for motion induced instability can be done in an iterative process. The objective of a motion induced instability analysis is to find the lowest mean wind velocity that would excite motion induced instabilities; theoretically meaning that $\mu > 0$ from theory in 5.3, and for what eigenmode it would be executed at. In further explaination of the iteration process, the flowchart in Figure 5.6 will be referred to.

Parameters are firstly set to initial values, where V and V_{Max} would be the lowest and maximum mean wind velocity that would be investigated for. ω_{guess} is set equal to the first eigenfrequency from the structural model, it_{max} is the maximum number of iterations for a converged eigenvalue a mode could be searched for, $diff$ is the initial value for the difference between ω_{guess} and ω_{it}, ϵ is the convergence criteria for the eigenvalues and μ can be set to a negative number. Moreover, a velocity step for the iteration procedure, dV needs to be defined and is set typically to lower values such as 1 or 2 m/s.
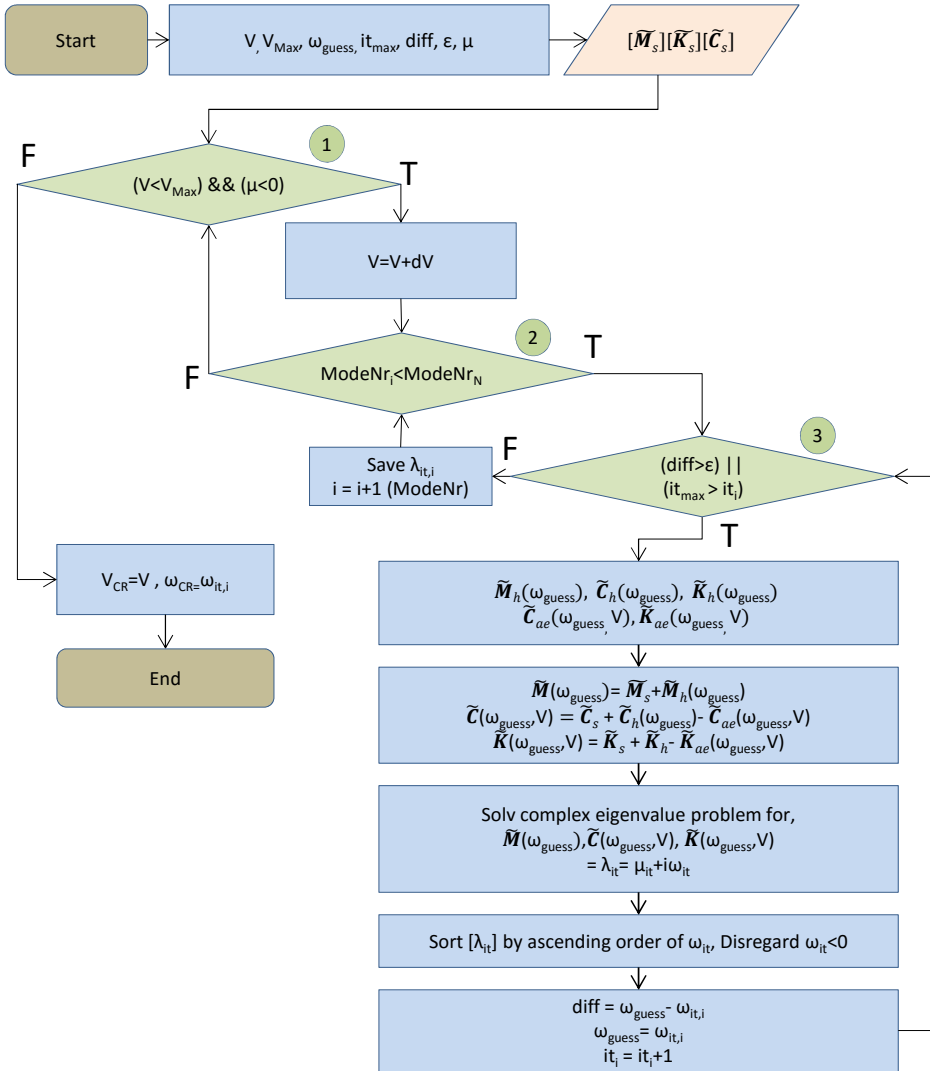
The modal mass, damping and stiffness can be obtained from ABAQUS. The third decision box (in Figure 5.6) initiates a while loop that searches for a converged eigenfrequency for mode i for a fixed mean wind velocity. The loop stops when $|\omega_{guess} - \omega_{it}| = diff < \epsilon$ or when convergence is not reached for it_{max} number of iterations. The real and imaginary part of the converged eigenvalue is saved, before one moves on to the the next mode, but

for the same mean wind velocity. When converged eigenvalues (or reached it_{max}) for all modes have been found, failing the second decision box, the first decision box checks if all of the real parts of the eigenvalues are negative, $\mu < 0$ and if $V < V_{Max}$. If both options are true, the mean wind velocity is increased and the entire process starts over. If $\mu > 0$ ($V < V_{Max}$) the program returns the mean wind velocity of which excites the motion induced instability, and a corresponding critical frequency and mode can be obtained.

Not shown on the flowchart for simplicity is the refinement step of dV. When the mean wind velocity is iterated to a value of which μ is positive, a refinement process is done to reduce the velocity step for obtaining a more exact critical mean wind instability limit. when reaching this condition, the iteration process will go one step back to previous V, and runs it again with dV=dV/2. This is done to find a more exact V_{CR}. The refinement of dV is done as many times as specified in an input parameter.

To account for frequency dependent hydrodynamic mass, damping and stiffness and aerodynamic damping and stiffness from aerodynamic derivatives, the matrices needed to be modalized before being coupled with the system to respectively $\tilde{\mathbf{M}}$, $\tilde{\mathbf{C}}$ and $\tilde{\mathbf{K}}$ as shown in the flowchart. To modalize these terms, the correct modes to use would be the modes from the coupled system, also accounting for a changing mean wind velocity. Modalizing using structural eigenvectors could instead be applied for modalization, reducing computational effort. As an evident consequence, the results would deviate from the real coupled system.

The correct modes could in principle have been found by repeating the iterative process for the fully coupled model from Section 5.2.1, but also iterated for mean wind velocity. Then eigenvalues and eigenmodes for all modes for all mean wind velocities up to V_{CR} could have been obtained. This process would however require a large computational effort.

Start

V, V_{Max}, ω_{guess}, it_{max}, diff, ε, μ

$[\widetilde{\boldsymbol{M}}_s][\widetilde{\boldsymbol{K}}_s][\widetilde{\boldsymbol{C}}_s]$

1

F $\quad$ (V<V_{Max}) && (μ<0) $\quad$ T

V=V+dV

2

F $\quad$ ModeNr$_i$<ModeNr$_N$ $\quad$ T

Save $\lambda_{it,i}$
i = i+1 (ModeNr)

F

3

(diff>ε) ||
(it_{max} > it_i)

T

V_{CR}=V , ω_{CR}=$\omega_{it,i}$

End

$\widetilde{M}_h(\omega_{guess})$, $\widetilde{C}_h(\omega_{guess})$, $\widetilde{K}_h(\omega_{guess})$
$\widetilde{C}_{ae}(\omega_{guess},$ V), $\widetilde{K}_{ae}(\omega_{guess},$ V)

$\widetilde{M}(\omega_{guess})= \widetilde{\boldsymbol{M}}_s+\widetilde{M}_h(\omega_{guess})$
$\widetilde{C}(\omega_{guess},$V) = $\widetilde{\boldsymbol{C}}_s + \widetilde{C}_h(\omega_{guess})$- $\widetilde{\boldsymbol{C}}_{ae}(\omega_{guess},$V)
$\widetilde{K}(\omega_{guess},$V) = $\widetilde{\boldsymbol{K}}_s + \widetilde{\boldsymbol{K}}_h$- $\widetilde{\boldsymbol{K}}_{ae}(\omega_{guess},$V)

Solv complex eigenvalue problem for,
$\widetilde{M}(\omega_{guess})$,$\widetilde{C}(\omega_{guess},$V), $\widetilde{K}(\omega_{guess},$V)
= λ_{it}= μ_{it}+iω_{it}

Sort [λ_{it}] by ascending order of ω_{it}, Disregard ω_{it}<0

diff = ω_{guess}- $\omega_{it,i}$
ω_{guess}= $\omega_{it,i}$
it_i = it_i+1

Figure 5.6: Flow chart showing algorithm used to find V_{CR} for motion induced instability

Chapter 6

Results

In this chapter, results will be presented based on the analysis procedures in Chapter 5 for the bridge model for Bjornafjorden. A modal analysis, identifying modes and eigenfrequencies in addition to a response analysis has been carried out. Moreover, the bridge model is investigated for motion induced instabilities due to wind.

The modal analysis with a detailed description of the modes will be displayed and described with the corresponding eigenfrequencies. The modal analysis of the bridge takes into account damping and stiffness contributions from wind, and hydrodynamic added mass and added damping when solving the complex eigenvalue problem. The results from this analysis will be divided into a group with modes with a more significant pontoon motion and a group of modes with insignificant pontoon motion, where only the girder and cables participate.

For the response analysis, the bridge model will be tested for different stationary environmental conditions in reference points on the girder and on the pontoons. The aim of this analysis is to see the impact of wind and waves on the bridge response by connecting wind and wave spectra with the modes of the structure. Response is as described in Chapter 5 carried out in frequency domain and will be presented in terms of standard deviation and power spectral density functions of the response in chosen degrees of freedom.

The results from the motion induced instability analysis will also be presented in terms of critical velocities, frequencies and corresponding modes.

6.1 Modal Analysis

The natural frequencies and mode shapes were extracted from the structural model, the fully coupled model and the model coupling only hydrodynamic and structural terms. The eigenfrequencies are plotted in there ascending order for the three models in figure 6.1.
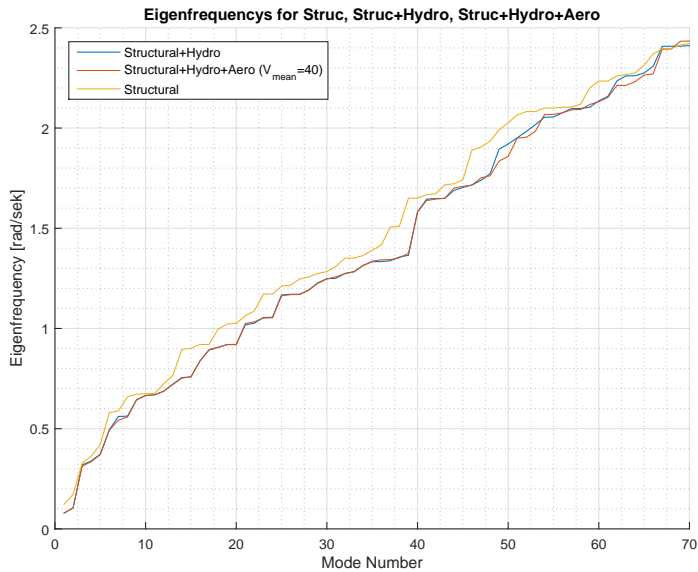

Figure 6.1: Eigenfrequencies plottet against mode number in cornological order

The modes are mainly in the same order for the three models, but some modes have changed places in regard to the other models. It can be seen when accounting for hydrodynamic and aerodynamic effects the eigenfrequencies have been shifted to lower frequencies. The difference between the eigenfrequencies of the hydrodynamic and fully coupled model is small. Thus, it is evident that the contributions from the hydrodynamic matrices have a much larger impact on the structural eigenfrequencies than the aerodynamic effects for $V_{mean} = 40$.

A closer analysis of the mode shapes are conducted below. The fully coupled model is the most realistic system and is therefore the one that will be presented in the modal analysis. The analysis of the mode shapes are divided into two groups. The modes in the first group will characterize the mode shapes with significant motion in the pontoons. The second group characterizes the modes where the pontoon motion is much less significant compared to the relative motion in the girder and cables.

The direction and rotation of motion is described in terms of the global coordinate system, for the girder in each span, main cable pair in each span and the two floating towers.

Motion in directions that are less dominating but are evident in the mode shapes are put in parenthesis. The girder motion is also classified as symmetric or anti-symmetric modes about the xz-plane in the bridge girder middle, in the middle span. Symmetric modes will be denoted S, anti-symmetric, A, or neither, (-). The number of amplitudes peaks per span in a direction is denoted e.g y2 for 2 peaks in the y direction which is a full sine curve.
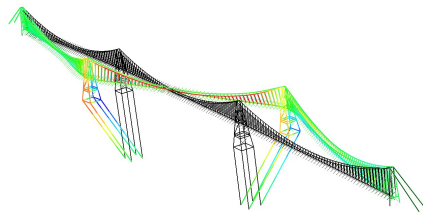
6.1.1 Pontoon modes

Table 6.1 describes each mode with significant pontoon motion. The motion for the pontoon modes are described in terms of the girder in each span and the two pontoons. Recalling that the girder and towers are kinematically coupled in all 6 degrees of freedom of translations and rotations; resulting in directly coupled motions. The cables for all the tower modes follow the motion of the girder. Figure (6.14) shows all the modes of which the pontoons have significant relative motion.

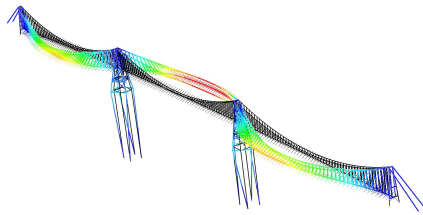Table 6.1: Modes with significant motion in the pontoons

| Mode	Frequency	Girder			Pontoon		Symmetry
	[rad/s]	1	2	3	1	2	
1	0.0785	y	y	y	y	y	S
2	0.1045	y	y	y	y	y	A
3	0.3128	y1	y1	y1	θ_z	θ_z	S
4	0.3352	y1	(y2)	y1	θ_z	θ_z	A
6	0.4919	y2	y2	y2	θ_z	θ_z	A
7	0.5425	y2	y3	y2	θ_z	θ_z	S
8	0.5581	y2, (z1)	y3, (z1)	y2, (z1)	θ_z	θ_z	S
9	0.6433	z2,	z2	z2	$x, (\theta_y)$	$x, (\theta_y)$	A
12	0.6869	z1	z2	z1	θ_y	θ_y	A
14	0.7521	y2	(y3)	y2	θ_z	θ_z	S
15	0.7589	(z1)	z2	(z1)	θ_y	θ_y	A
16	0.8367	(y2)	y2	(y2)	θ_z	θ_z	A
17	0.8948	z3	z3	z3	θ_y	θ_y	S
18	0.9065	z3	z3	z3	θ_y	θ_y	S
40	1.5805	y3, $\theta_x 1$	(y3, $\theta_x 1$)	-	θ_x	(θ_x)	A
41	1.6381	(y3, $\theta_x 1$)	(y3, $\theta_x 1$)	y3, $\theta_x 1$	-	θ_x	-
45	1.709	$\theta_x 1$	-	-	θ_x	-	-
							-
48	1.7622	$(\theta_x 1)$	$(\theta_x 1)$	$\theta_x 1$, (y4)	(θ_x)	θ_x	-
49	1.8353	$\theta_x 1$	$\theta_x 1$	$\theta_x 1$	θ_x	θ_x	S
51	1.95	$\theta_x 2$, (y4)	(y4)	$\theta_x 2$, (y4)	θ_x, θ_z	θ_x, θ_z	A
56	2.0761	$\theta_x 3$, (y4)	$\theta_x 3$, y4	$\theta_x 3$, y4	(θ_x)	θ_x	A
61	2.1529	$\theta_x 2$	-	$\theta_x 2$	θ_x	θ_x	A
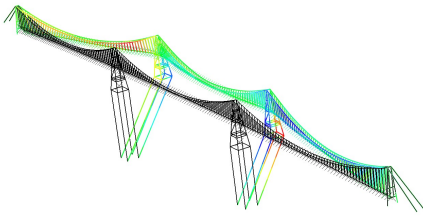
Mode 1, $\omega = 0.0785$

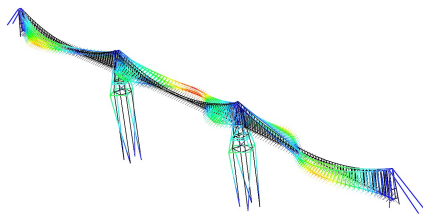

Mode 2, $\omega = 0.1045$

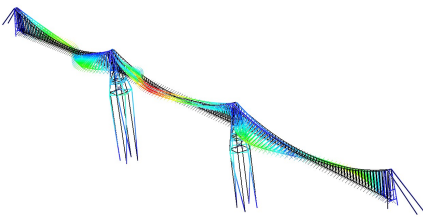
Mode 3, $\omega = 0.3128$
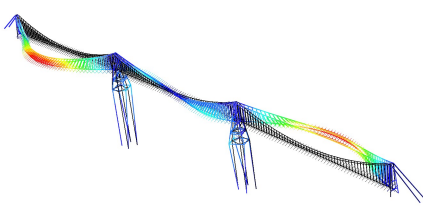
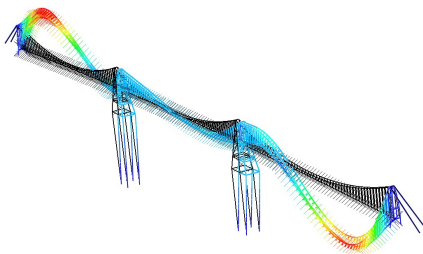Mode 4, $\omega = 0.3352$
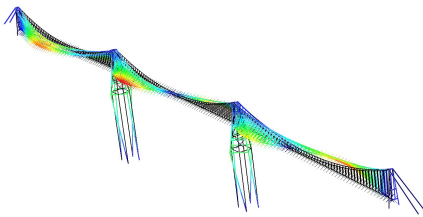
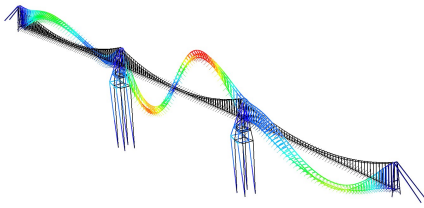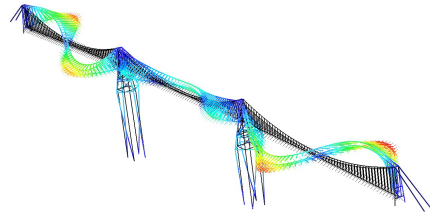Mode 6, $\omega = 0.4919$

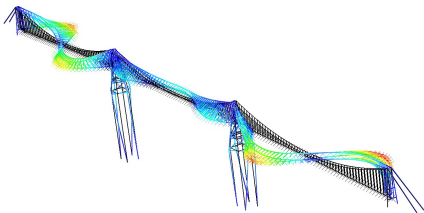Mode 7, $\omega = 0.5425$

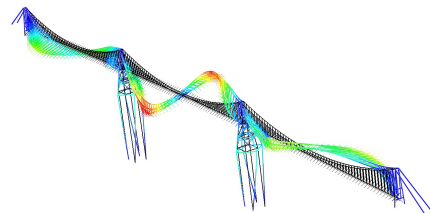Mode 8, $\omega = 0.5581$

Mode 9, $\omega = 0.6433$

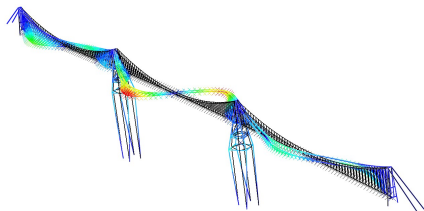Mode 12, $\omega = 0.6870$
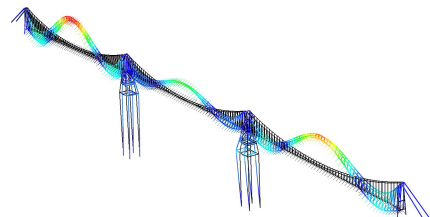

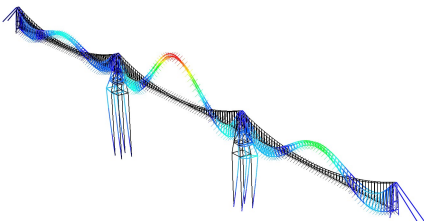Mode 13, $\omega = 0.7200$

Mode 14, $\omega = 0.7521$

Mode 15, $\omega = 0.7589$

Mode 16, $\omega = 0.8367$

Mode 17, $\omega = 0.8948$

Mode 18, $\omega = 0.9066$

Mode 19, $\omega = 0.9193$

Mode 40, $\omega = 1.5805$

Mode 41, $\omega = 1.6381$

Mode 45, $\omega = 1.7090$
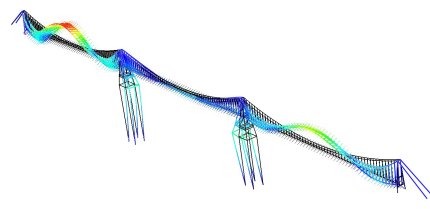
Mode 48, $\omega = 1.7622$

Mode 49, $\omega = 1.8353$

Mode 51, $\omega = 1.9500$

Mode 56, $\omega = 2.0761$
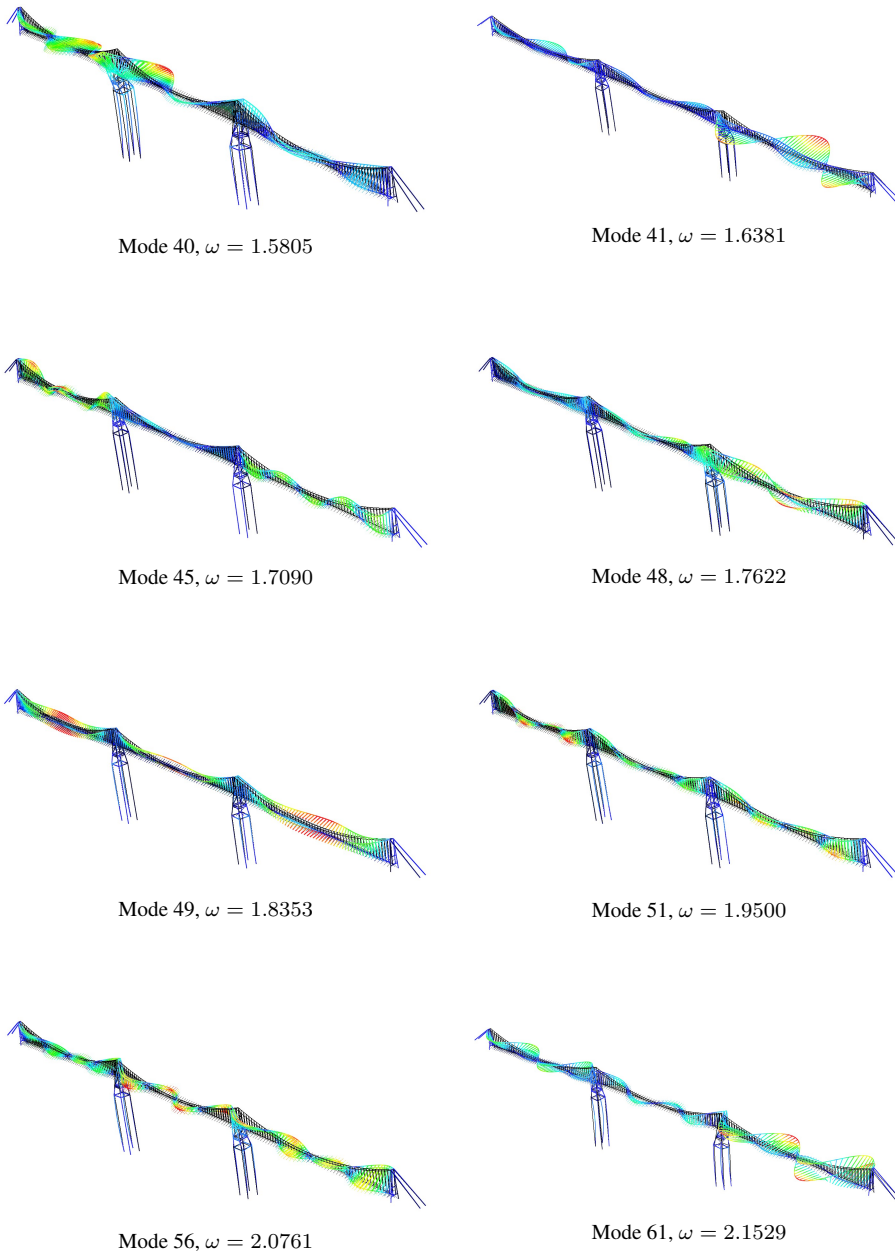
Mode 61, $\omega = 2.1529$

Figure 6.14: Mode shapes with significant motion in the pontoons

Mode 1 and 2 are pure translative in the y direction. The tethers are 100m longer for the left tower so the displacement is larger. For mode 1 the towers move in parallel making it symmetric, while for mode 2 the towers mode in opposite directions, making it anti symmetric with close to zero motion at midpoint of the girder.

Mode 3, 4, 6, 7, 8, 14 and 16 are all due to rotation about the z axis in the towers, translating into y displacements in the girder. Mode 3 is a half sine per span with opposite rotating towers. Mode 4 is like mode 3 but symmetric. Mode 6 is a full sine per span with symmetric rotating towers. Mode 7 is a full sine for span two and three, and one and a half sine for the middle span with opposite rotating towers. Mode 8 is like mode 7 but with some displacement in the z direction. Mode 14 is a symmetric mode with a full sine in span one and three and one and a half sine in the middle span and opposite rotating towers. Mode 16 is like mode 7 with a full sine in each span in the y direction but with a higher amplitude in the middle span and parallel rotating towers.

Mode 9, 12, 15, 17 and 18 are modes with rotation in the pontoon about the y axis. Mode 9 also has some translation of the towers in the x direction, with the tower moving in parallel. The girder moves asymmetrically with two amplitude peaks in all three spans. Mode 15 is similar to mode 9 but with no translation of the pontoons in the x direction. Mode 17 and 18 are similar with symmetric rotating pontoons about the y axis and three peak amplitudes in the z direction in each span. In mode 17 the amplitude is slightly higher for the side spans and in mode 18 they are slightly lower than the middle span amplitude.

Mode 40, 41, 45, 48, 49, 51, 56 and 61 have rotating motion about the x-axis. This motion usually gives the girder torsion. Mode 40 has a larger rotation in the left tower than the right, and the girder and cables are moving in opposite directions with one and a half sine curve per span. There is also some torsion in the girder due to the opposite rotation of the towers. The motions are largest in the left span, smaller in the middle and very small in the right span. Mode 41 is very similar to 40 but with less displacements all over. Mode 45 is the same as 40 but with the significant motion in the other tower. Mode 45 has rotation on the left pontoon and torsion in the girder in the first span. Mode 48 has more rotation in the right than left tower and girder torsion in all spans. Mode 49 has parallel rotation towers and significant symmetric rotation in all three spans. Mode 51, 56 and 61 has double torsion in the two side spans due to rotation of the towers about the x axis. Mode 51 also has some rotation about the z axis.

Note that vertical pontoon modes, heave, are not within the 70 first modes. The reason is assumed to be because of the tremendous tension in the tethers.

Amongst the modes with significant motion in the pontoons, there is a trend that mode with horizontal motion in the girder occur before vertical motion. The torsional modes all occur for a even higher frequency.

6.1.2 Girder and Cable Modes

The modes were the movement in the pontoons are insignificant are listed in Table 6.2. The notation is the same as in Table 6.1. The cables are given values in the table only when they don't follow the girder.

Table 6.2: Modes with insignificant pontoon movement

Mode	Frequency	Girder			Cables			Symmetry
	[rad/s]	1	2	3	1	2	3	
5	0.3707	y1	y1	y1	-	-	-	S
10	0.6662	z2	-	z2	-	-	-	S
11	0.6693	z2	-	z2	-	-	-	A
13	0.7200	y2	y2	y2	-	-	-	A
19	0.9193	-	-	-	y1	-	-	-
20	0.9194	-	-	-	-	-	y1	-
21	1.0244	z3	-	z3	-	-	-	A
22	1.0333	z3	z3	z3	-	-	-	S
23	1.0521	$\theta_x 1,(y1)$	-	$\theta_x 1,(y1)$	y1	-	y1	S
24	1.0531	$\theta_x 1,(y1)$	-	$\theta_x 1,(y1)$	y1	-	y1	S
25	1.1629	(y2)	-	-	y2	-	-	-
26	1.1687	-	-	-	-	-	y2	-
27	1.1698	(y2)	-	-	y2	-	-	-
28	1.1914	-	-	$(y2, \theta_x 1)$	-	-	y2	-
29	1.2252	y3	y3	y3	-	-	-	S
30	1.2469	y3	-	y3	-	-	-	A
31	1.2578	z3	z3	z3	-	-	-	S

32	1.2736	-	-	-	-	y1	-	S
33	1.2824	-	-	-	-	y2	-	S
34	1.3142	y3	$\theta_x 1$, y3	y3	-	-	-	S
35	1.3355	-	$\theta_x 1$, y2	-	-	y1	-	-
36	1.3427	z4	-	z4	-	-	-	A
37	1.3433	z4	-	z4	-	-	-	S
38	1.3528	-	$\theta_x 1$, y2	-	-	-	-	-
39	1.3753	-	z4	-	-	-	-	A
								-
42	1.6458	-	-	-	y3	-	(y3)	-
43	1.6497	-	-	(y3)	(y3)	-	y3	-
44	1.7000	z5	-	z5	-	-	-	A
46	1.7156	z5	(z5)	z5	-	-	-	S
47	1.7512	-	z5	-	-	-	-	S
50	1.8588	$\theta_x 1$	-	$\theta_x 1$	-	-	-	S
52	1.9540	$\theta_x 1$	$\theta_x 1$	$\theta_x 1$	-	-	-	S
53	1.9837	y4	(y4)	y4	-	-	-	S
54	2.0672	z6	-	z6	-	-	-	A
55	2.0683	z6	-	z6	-	-	-	S
57	2.0912	-	-	-	y4	-	(y4)	-
58	2.0926	-	-	-	(y4)	-	y4	-
59	2.1178	-	z6	-	-	-	-	A
60	2.1315	y4	-	y4	y	-	y	S

62	2.2126	$\theta_x 2$	-	$\theta_x 2$	z2	-	z2	S
63	2.2128	$\theta_x 2$	-	$\theta_x 2$	z2	-	z2	A
64	2.2315	-	-	-	-	y4	-	S
65	2.2645	-	$\theta_x 2$	-	-	z4	-	A
66	2.2703	-	-	-	-	y4	-	-
67	2.3935	tether	-	-	-	-	-	-
68	2.3947	tether	-	-	-	-	-	-
69	2.4331	z7	-	z7	-	-	-	A
70	2.4342	-	y4, $\theta_x 2$	-	-	y4	-	A

Vertical modes

The modes with main amplitudes in the z direction are mode 10, 11, 21, 22, 31, 36, 37, 39, 44, 46, 47, 54 and 55. They range from two peak amplitude per span (mode 10) to six peak amplitudes per span (mode 55). The single peak per span modes are amongst the pontoon modes. The first vertical mode shape

Horizontal modes

The modes with main amplitudes in the y direction are mode 5, 13, 25, 27, 29, 30, 34, 53 and 60.They range from single peak amplitude (mode 5) to four peaks (mode 60).

Torsional modes

Relative torsion occurs in modes with significant relative motion in the pontoons. It follows that the rigid connection between the girder and the towers transfers (40, 41, 45, 48, 49, 51, 56, 61) due to the kinematic coupling of the girder and tower. The torsional modes are from Table 6.2 are 23, 24, 50, 52, 62, 63 and 65. It can be seen that torsion mainly occurs for modes for the frequency range of $\omega = 1.5805$ (mode 40) to $\omega = 2.2645$ (mode 65) for the first 70 modes. Most of the modes have one twisting along the girder per span. Mode 62,63 and 65 has double torsion. The modes are often coupled with cable motion in the z direction.

Cable modes

The pure cable modes are mode 19, 20, 25, 26, 28, 32, 33, 42, 43, 57, 58, 64 and 66. All the modes are in the motion of the main cables in the y direction. The reason there are no pure z direction motion is that with vertical motion of the main cables comes girder motion in z direction or torsion. Mode 67 and 68 are motion in one of the tethers.

Coupled modes

Modes 34, 35, 38 and 70 are coupled modes i.e. girder motion in vertical, horizontal and/or torsional. All the directional coupled modes are coupled in y and x rotation.

(a) Largest y displacements

(b) Largest z displacements
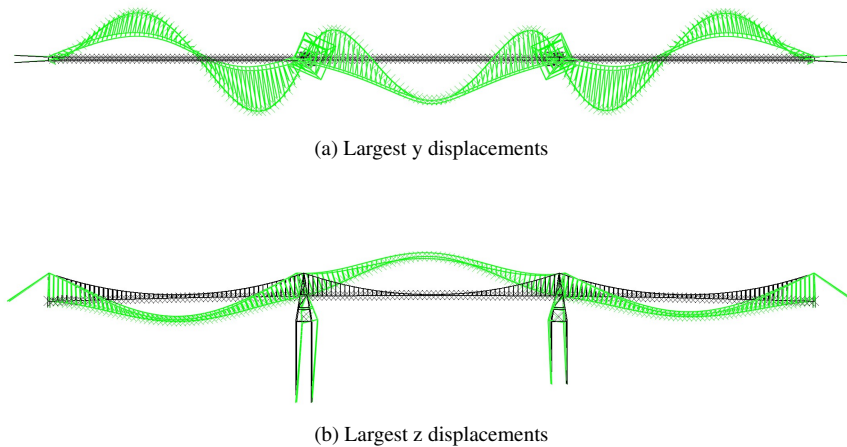
Figure 6.15: Coupled mode 8

It is the modes with the fewest amplitude peaks for the bridge that usually contribute to large response, in therms of standard deviation, also dependent on the load spectra. Theses modes for the y direction is mode 1, with parallel translation of both towers, mode 2 with opposite translation of both towers and mode 3, with opposite rotating towers and one peak amplitude per span. In the z direction it is mode 8, with one peak amplitude per span. This mode is also coupled with displacements in the y direction. Mode 11 has two peaks in the z direction. In torsion mode 23 has one twisting in the side spans and mode 40 has torsion in all spans.

6.2   Modal system vs. ABAQUS

The peaks from the sum of the modal transfer functions in figure 5.5 show some of the eigenfrequencies of the system. These modal transfer functions are based on the mode

shapes from the structural model. The mode shapes that would have been used to obtain a theoretically more correct modal form of the transfer function, would have been the complex mode shapes from the coupled system model. The eigenfrequenies obtained from the peaks and the eigenfrequencies from the complex frequency analysis in ABAQUS are plotted in figure 6.16a.
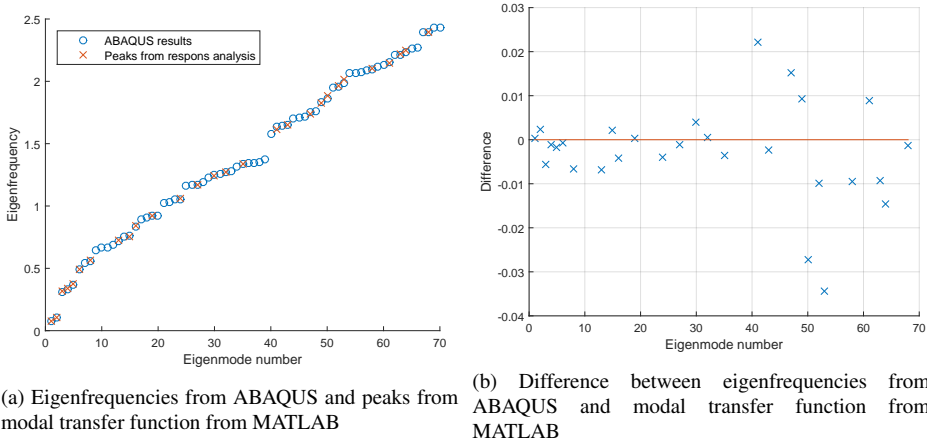

(a) Eigenfrequencies from ABAQUS and peaks from modal transfer function from MATLAB

(b) Difference between eigenfrequencies from ABAQUS and modal transfer function from MATLAB

Figure 6.16: Eigenfrequencies from peak picking of modal transfer function compared to eigenfrequencies obtained from ABAQUS

The 28 peaks shown in the modal transfer function are not necessary the 28 first eigenfrequencies. A MATLAB script compared the eigenfrequency obtained from the transfer function peaks with the eigenfrequencies from ABAQUS, and assigned the mode number for the closest value. This result in a best case scenario for obtaining a good fit of the transfer function eigenfrequencies with the ABAQUS eigenfrequencies. The discrepancies in rad/s is shown in figure 6.16b. For the first 7 modes it seems like all the eigenfrequencies are present.

It can be seen that the use of structural eigenfrequencies resulted in accurate eigenfrequencies from peak picking compared to the ABAQUS results, with the assumptions given above. The plots show that the use of a modal approach using eigenvectors from a pure structural model and then couple the system with the environmental effects, will govern the same eigenfrequencies as in the fully coupled ABAQUS model. This seems true especially for the lowest eigenfrequencies. It will accordingly be fair to refer to the modal analysis in ABAQUS when performing the response analysis in MATLAB in the following results.

6.3 Response

The bridge response was calculated using the procedures in chapter 5. A set of points on the bridge with degrees of freedom are chosen to represent the response for a chosen set of environmental conditions in terms of significant wave height H_s and mean wind velocity V_{mean}.
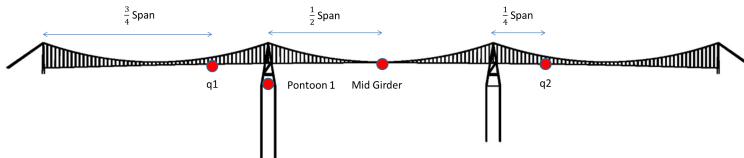

Figure 6.17: Position of the reference nodes for the response investigation

The mid-girder node and the two pontoon reference nodes are chosen as reference nodes for response representation.The largest responses can be expected to be in these nodes or in nodes close to them. To represent also the anti-symmetric modes and local girder modes in the side-spans in the response analysis, two nodes have been chosen at two symmetric points in the third quarter of the first span and first quarter of the third span. These nodes will be referred to as mid girder, pontoon 1 and q1 and q2. The node positions on the bridge are shown in Figure 6.17.

The response will be represented in the degrees of freedom for y- and z-translation and θ_x-rotation for the girder, and y, z, θ_x and θ_z-direction for the pontoon. Only the auto-spectral forces for response in a given direction will be addressed. The notation S_{r22-44} and S_{r66} will be used to refer to the four degrees of freedom for the pontoon, while S_{r11-33} will be used as notation for the first three degrees of freedom in the girder wrt. global coordinates.

The emphasis of this dynamic response analysis is to see how the modeled bridge structure responds to high wind and wave loads. From the previous chapter, the spectral wave forces have high power spectral densities for frequencies around 0.4-1.2 rad/s, while wind energy is exponentially decaying from low frequencies at zero to higher frequencies.

Coupled conservative stationary environmental conditions have been chosen to see response effects. Presumed joint environmental short term conditions of H_s and mean wind velocity are chosen in accordance with TDA engineering reports [10]. A more thorough description of this response is given in Section 4.3.1. A crest length is chosen to be s=5 for the spectral response analyses. The crest length s is typically between 4 and 9 according to the recommended practice of DNV, RP-C205 [1]. H_s will be set to 3.75 meters and V_{mean} to 29 m/s.

Moreover, the standard deviation response will be calculated for $[25 \times 29]$ environmental conditions in surface plots, with 25 different H_s and 36 V_{mean} from 0 m to 6 meters and from 0 to 29 m/s. The response will be calculated in standard deviation, integrating over the given frequency interval of 0 to 6 rad/s, for three degrees of freedom and in the

first span, the mid-girder node, and for one of the pontoon nodes. Three conditions will subsequently be picked out for a standard deviation response calculation along the girder and the two towers in the three chosen directions. These three conditions correspond to:

Table 6.3: Conditions tester for standard deviation

State	Significant wave height	[m]	Mean wind velocity	[m/s]
1	H_s	6	$Vmean$	0
2	H_s	6	$Vmean$	29
3	H_s	3.75	$Vmean$	29

The response due to changing crest length s will be also be addressed by the effects of standard deviation along the girder for conditions 2 and 3 where waves participate.

The standard deviation is the integral of the spectral response spectrum. One can not accurately state the response from the magnitude of the y axis of the spectral plot, but a high peak will usually indicate a larger value for the integral and the response. This argument will be used to indicate if the response is small or significant in the spectral analysis bellow.

6.3.1 Mid-Girder response in y, z and θ_x-direction
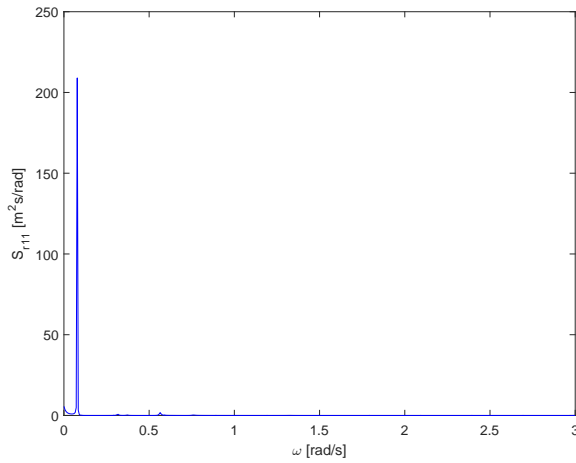
(a) $S_{r,11}$ Coupled response in y-direction
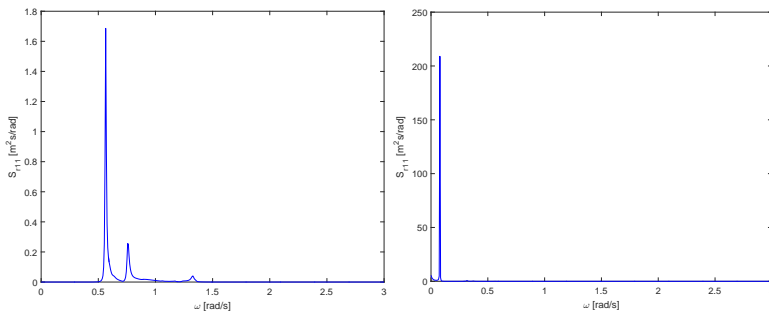
(b) $S_{r,11}$ in y-direction due to hydrodynamic load

(c) $S_{r,11}$ in y-direction due to aerodynamic load

Figure 6.18: y-DOF in mid-girder

Mid-girder node, y-direction
There is one peak of significance in the plot for the coupled response in y-direction for the mid-girder. The peak frequency is 0.0782 rad/s, corresponding to mode 1. Figure 6.18c for aerodynamic force contributions displays 100 times the highest peaks in the hydrodynamic force contributions of respectively 0.5582 and 0.75 rad/s. As the energy content of wind is high for the lowest frequencies, it seems evident that response in y-direction in the girder will be driven by the wind.

(a) $S_{r,22}$ Coupled girder response in z-direction

(b) $S_{r,22}$ in z-direction due to hydrodynamic load

(c) $S_{r,22}$ in z-direction due to aerodynamic load
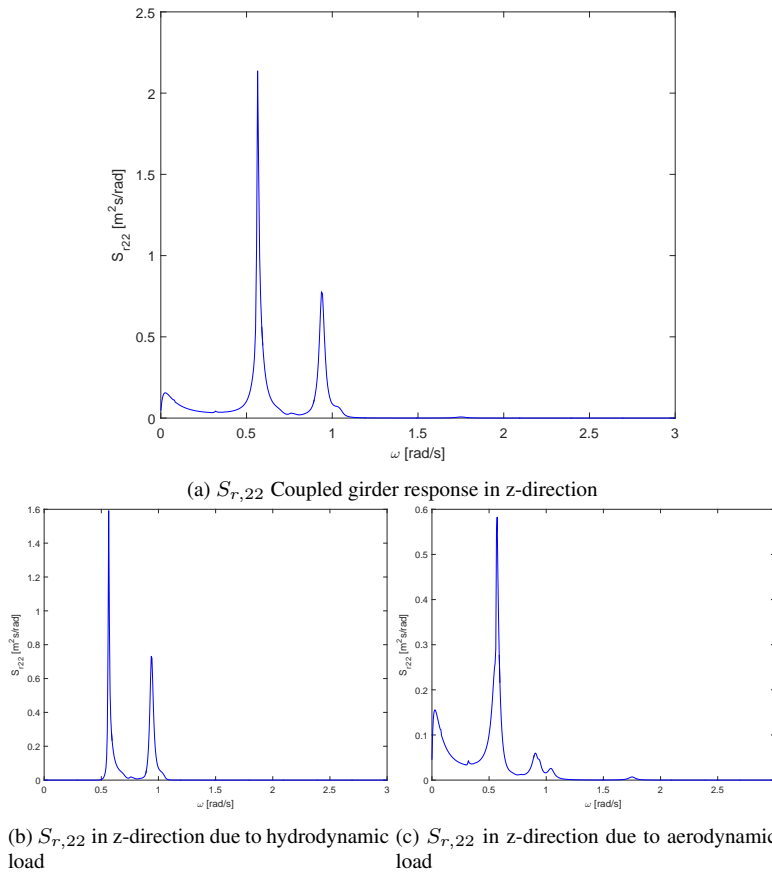
Figure 6.19: z-DOF in mid-girder

Mid-girder node, z-direction

In z-direction, the notable peaks of the coupled response is 0.582 and 0.91 rad/s. These peaks are concurrent with the two peaks shown in 6.19b, showing hydrodynamic response contributions. The wind spectrum excites also these frequencies, but with lower amplitudes. The large peak at the lowest frequencies in the coupled response is clearly excited by the wind. The two notable peak frequencies corresponds to mode 8 and 18 which have large relative amplitudes in z-direction for the mid-girder node. As the wave load frequencies for given H_s and crest length s at tower 1 have high relative amplitudes for the two given frequencies, it seems evident that the waves will govern the response in z-direction for the mid-girder node.
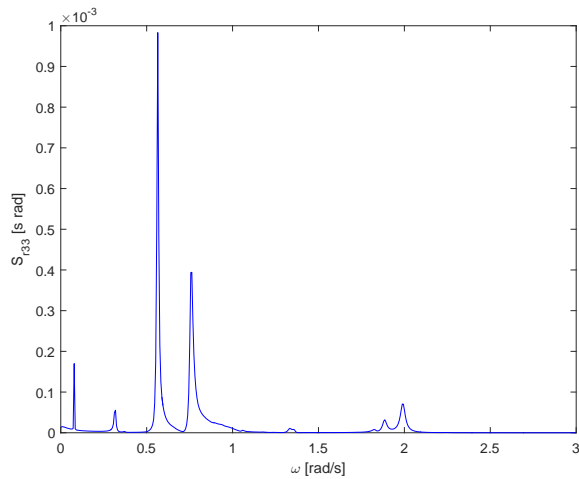
(a) $S_{r,33}$ Coupled girder response in θ_x-direction
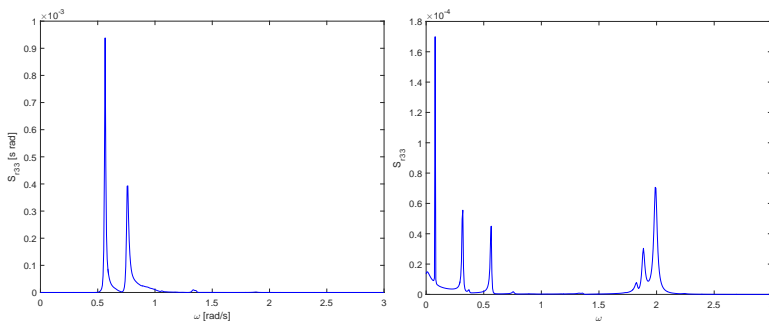
(b) $S_{r,33}$ in θ_x-direction due to hydrody-namic load

(c) $S_{r,33}$ in θ_x-direction due to aerodynamic load

Figure 6.20: θ_x-DOF in mid-girder

Mid-girder node, θ_x-direction

Notable peaks in the coupled response plot are at frequencies 0.5582 rad/s and at 0.76 rad/s; and correspond well to the notable peak frequencies in subfigure 6.20b. Mode 8 and mode 16 seem to govern this response. None of these modes were characterized as torsional modes. However, both mode 8 and 16 are combined modes in z- and y-direction which might give rise to torsion. Wave load peak frequencies are the highest in the interval of 0.5-1.2 rad/s and will excite modes to response. Peaks from the coupled response sub figure 6.20a consist of contributions from response of both wind and wave loads. From the modal analysis, the purer torsional modes occurred for much higher frequencies. The mode with the most significant torsion was at 1.9540 rad/s. This peak seems to be excited of wind, and creates a minor contribution to the total response.

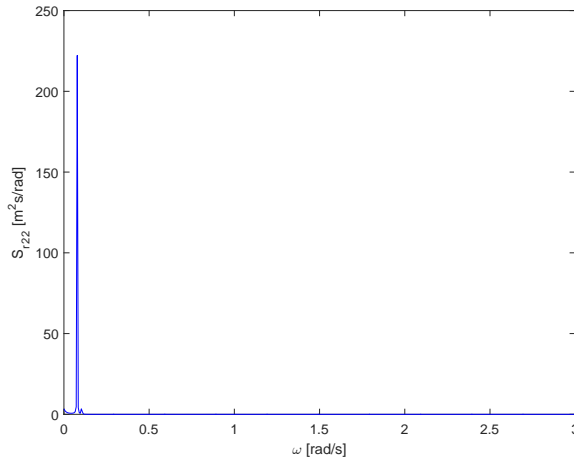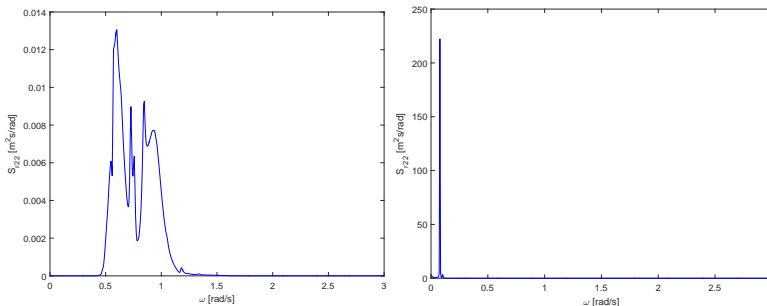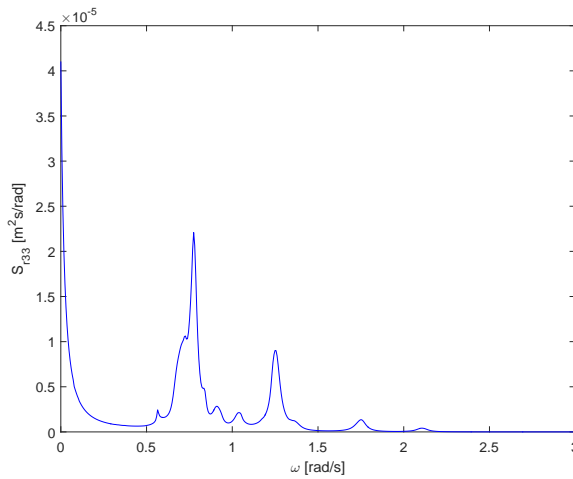# 6.4 Pontoon 1 response in y, z and θ_x-direction

(a) $S_{r,11}$ in y-direction for combined loads

(b) $S_{r,11}$ in y-direction due to hydrodynamic load

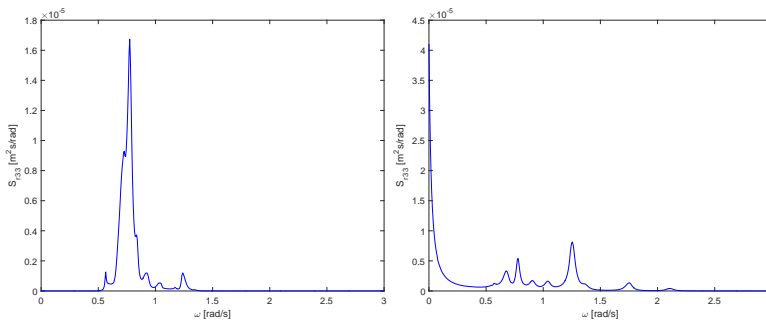(c) $S_{r,11}$ in y-direction due to aerodynamic load

Figure 6.21: y-direction in pontoon 1: Coupled response vs. response contributions from hydrodynamic and aerodynamic loads.

Pontoon, y-direction

The peaks frequencies in the figure displaying coupled response for the pontoons are 0.0782 and 1.02 rad/s, which correspond to respectively mode 1 and mode 2. The peak at 1.02 rad/s is however minor compared to the peak at 0.0782 rad/s. One could have expected a higher peak at this frequency, as mode 1 and mode 2 lie closely in terms of frequency and as mode 2 displays high relative motion in y-direction. The response contributions from waves are low, seen in the magnitudes of the y-axis in sub figure 6.21b and 6.21. Wind will accordingly govern the response in y-direction in the pontoons.

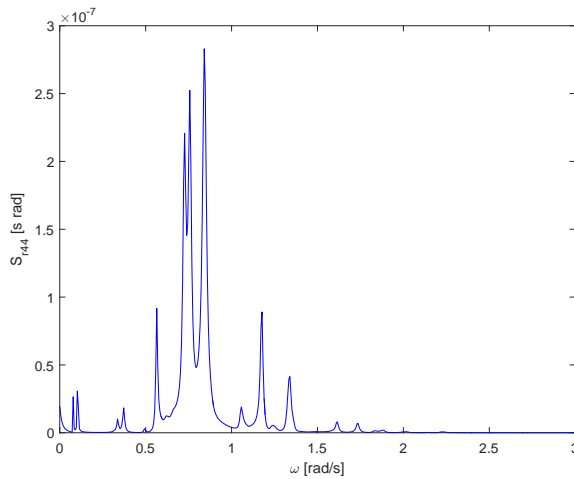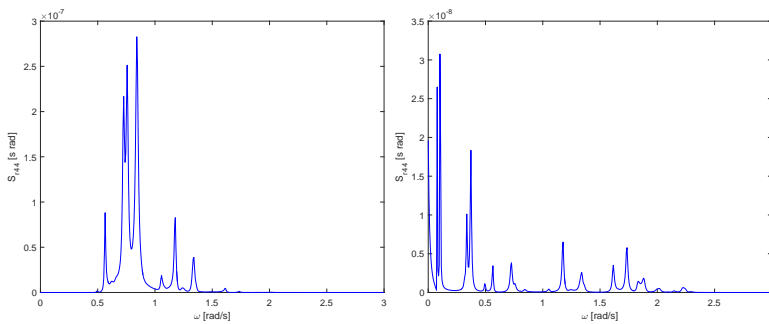(a) $S_{r,33}$ in z-direction for combined loads

(b) $S_{r,33}$ in Z-direction due to hydrodynamic load

(c) $S_{r,33}$ in Z-direction due to aerodynamic load

Figure 6.22: z-direction in pontoon 1: Coupled response vs. response contributions from hydrodynamic and aerodynamic loads.
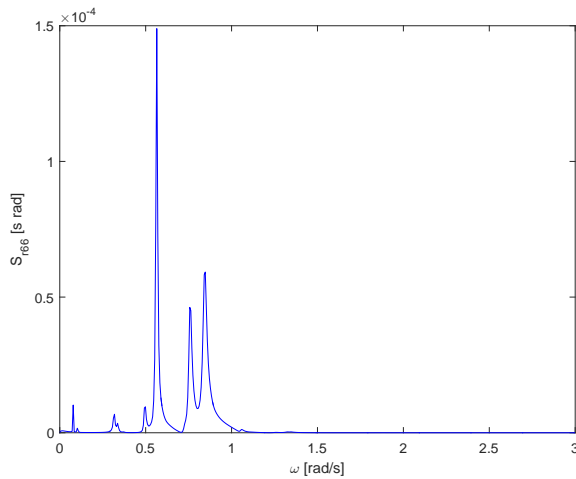
Pontoon, z-direction

There is a decaying trend for the coupled response in z-direction for the pontoons. The response is the highest for the very lowest frequencies, followed by peaks at 0.76 rad/s and at 1.3 rad/s. The notable peak from the hydrodynamic response contribution lies at 0.76 rad/s, corresponding to mode 15. Peaks at around 1.25 rad/s are from the modal analysis classified as a girder modes and do not either display significant relative motion in z-direction. From wind, a peak at 1.3 rad/s is excited in addition to a decaying wind. The magnitudes of both response contributions are at 10^{-5}, implying low response in z-direction. Recalling that the pontoons are moored to the sea bed with high tension-tethers, it was evident that the pontoon stiffness in z-direction should contribute to few significant modes in this direction for the pontoons for the lower frequencies.
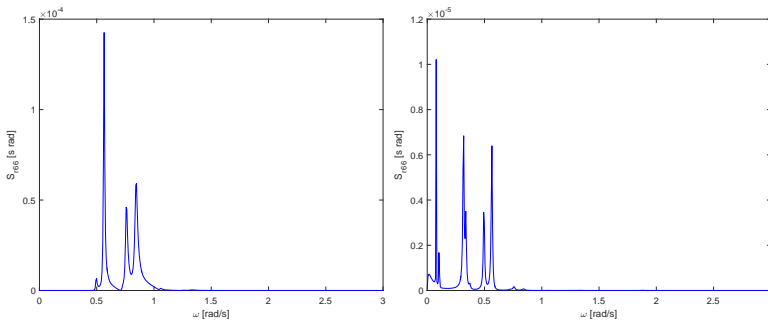
(a) $S_{r,44}$ in θ_x-direction for combined loads

(b) $S_{r,44}$ in θ_x-direction due to hydrodynamic load

(c) $S_{r,44}$ in θ_x-direction due to aerodynamic load

Figure 6.23: θ_x-direction in pontoon 1: Coupled response vs. response contributions from hydrodynamic and aerodynamic loads.

Pontoon θ_x-direction

The coupled response in torsion is distributed in the frequency range of 0.5-0.9 rad/s; these correspond mainly to the response contributions from the waves. From wind, the response contributions are lower. The magnitude is however 10^{-7}; implying that the torsional response in the tower is not significant. By looking at the peaks from sub figure 6.23b and 6.23c, the torsion might participate lowly in several modes in the whole frequency range.

(a) $S_{r,66}$ in θ_z-direction for combined loads

(b) $S_{r,66}$ in θ_z-direction due to hydrody- (c) $S_{r,66}$ in θ_z-direction due to aerodynamic
namic load   load

Figure 6.24: θ_z-direction in pontoon 1: Coupled response vs. response contributions from hydrodynamic and aerodynamic loads

Pontoon θ_z-direction
The spectral response in θ_z-direction shows a significant peak at 0.5581, 0.7521 and at 0.843 rad/s and might correspond to load resonance with mode 14 and 16 that in Table 6.1 were observed to give large relative rotation about the z-axis. Waves seem to govern the z-directional response.
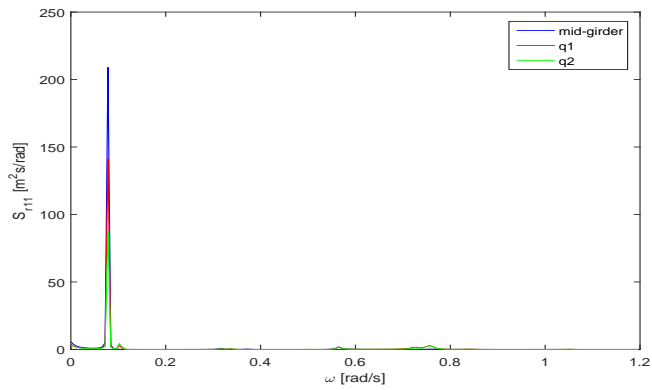
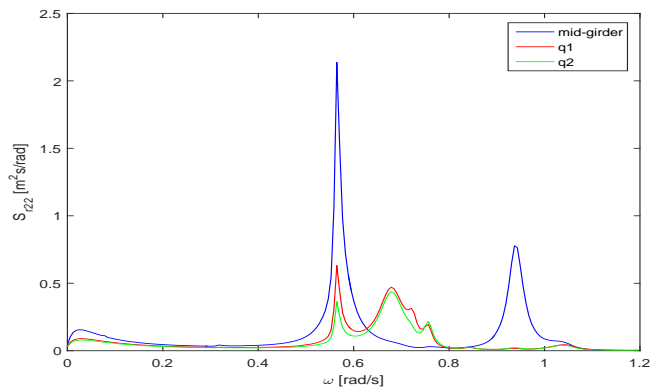Figure 6.25: Comparing spectral response in mid-girder, q1 and q2 in y-direction
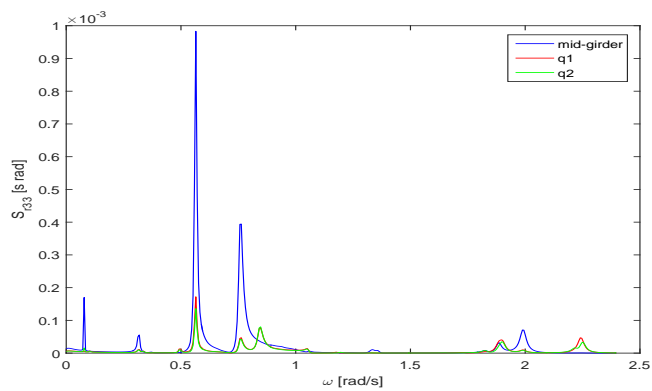

Figure 6.26: Comparing spectral response in mid-girder, q1 and q2 in z-direction

Figure 6.27: Comparing spectral response in mid-girder, q1 and q2 in θ_x-direction

Response in mid girder vs. q1 and q2

The plots in figure 6.25, 6.26 and 6.27 show the spectral response in y- z. and θ_x-direction for response in q1, the mid-girder and q2 on the girder. Mode 9, 12, 13, 14, 15, and 16 are anti-symmetric, giving relative motion in the q1 and q2 node of the first span but not in the mid-girder node. This is evident in the spectral response plot 6.25 in the frequency interval from 0.6433-0.8637 rad/s for z-direction, where spectral peaks have been excited for q1 and q2 for given frequencies but not for the mid girder.

For the two symmetric points q1 and q2, the same modes seem seem to be excited, implying a symmetric behavior in the bridge span. The spectral response in q1 is higher than for q2 for y-direction, which seems reasonable as the tethers for tower 1 are longer than the ones for tower 2. For the given plot, the response in mid-girder seems much more significant than for the response for q1 and q2.

6.4.1 STD response for varying H_s and V_{mean} in mid girder

The standard deviation for different H_s and mean wind velocities were calculated using spectral density functions for response in y, z and θ_x-direction for the mid-girder node and the pontoon node. The TDA environmental data were based on measurements and environmental contour, accounting for joint occurrence of wind and waves. The environmental conditions using 26 different H_s and 29 mean wind velocities from 0-6 m H_s and V_{mean} from 0-36 m/s. As 6 m significant wave height and 36 m/s wind can be considered conservative conditions for a fjord, one can assume that the H_s and V_{mean} gives a representation of the long term distribution of H_s and V_{mean} for wind driven waves.
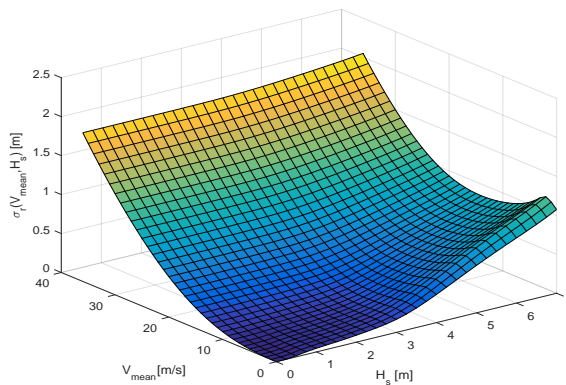

Figure 6.28: (a) Distributed response in mid-girder in y-direction

y-direction

The general trend of this surface plot is that wind creates significant response in standard deviation for high mean wind velocities. Response due to waves is also significant compared to the response due to wind. A descending curve for response of high significant wave heights but with increasing wind is assumed to be due to increasing aerodynamic damping for higher wind velocities. The motion induced wind forces are assumed to damp out the response for wind velocities below a certain high-point where perhaps the flow-induced wind forces overrides the motion induced damping contributions.

What is evident from the previously displayed wind and wave spectra is that wave loads act with higher frequencies from 0.4-1.2 rad/s while the wind is strongly decaying from lower to higher frequencies. As mode 1 governs the response in the y-direction, one can assume that the response is driven by wind for in particular the first modes, consistent with the results from the spectral density function plot in y-direction in the mid-girder in figure 6.18; for the TDA design condtions. The magnitude in the vertical axis shows STD at 2 meters, which can be considered notably high of a bridge with the given girder length.
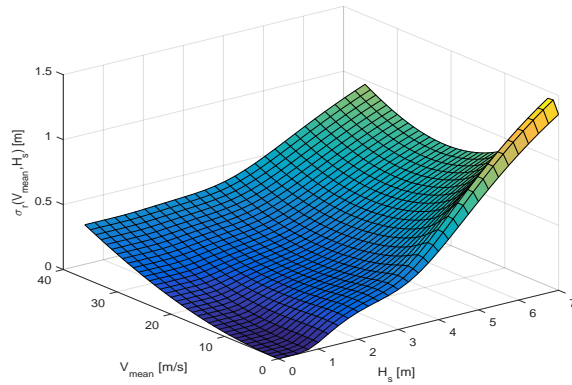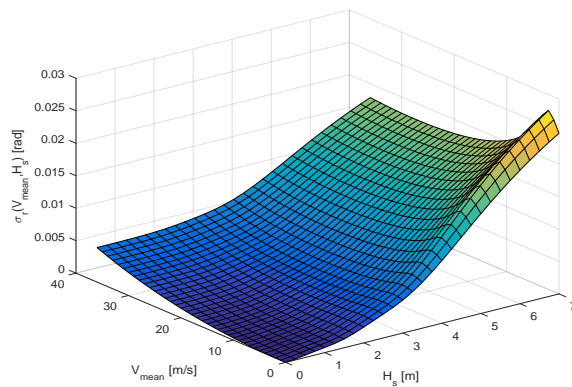
Figure 6.29: (b) Distributed response in mid-girder in z-direction
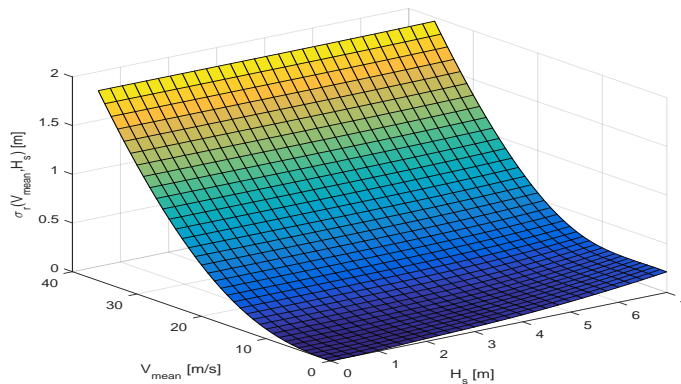
z-direction

Figure (b) shows higher response in standard deviation due to waves. The decaying trend due to higher wind is stronger. Wind are less significant for the response of the structure in this direction, and one can assume that the extremes occurring for high H_s and low wind are unrealistic as significant wave heights at this level do not occur for low wind velocities. Standard deviation responses at above 1 meters is still high, as this means that the vertical response can be more than half of the response in y-direction.

It is to be noted that peak frequencies from the load spectrum reside at frequencies around 0.4-1.2 rad/s; which might cause resonance with the e.g modes 8 and 16 that gave pure relative amplitudes in z-direction for the mid-girder. Further, one can assume that the response in z-direction is more governed by the waves than the wind for most environmental conditions seen on the surface plot.

Figure 6.30: (c) Distributed response in mid-girder in θ_x-direction
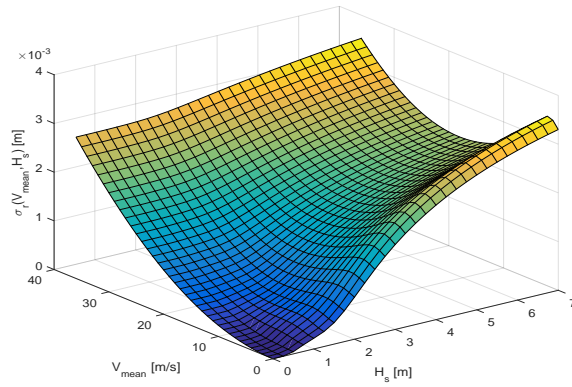
θ_x-direction

The torsional response in standard deviation is of low magnitude, but follows trends from both figure (a) and (b); a small decaying trend in response for higher mean wind velocities, and high response for high H_s. The response can accordingly be assumed to be governed by waves in larger extent than for the wind.

6.4.2   STD response for varying H_s and V_{mean} in in pontoon 1

(a) Distributed response in pontoon 1 in y-direction

A general trend for the standard deviation in y-direction in the pontoons is that waves seem to have insignificant impact on response. The fact that the modes with high relative motion in y-direction corresponds to mode 1 and 2, and the wind spectra should have high energy content for the lowest frequencies supports this argument. The y-direction displacement in the pontoons seem to be solely driven by the wind. High velocities seem to damp out the response for the lower mean wind velocities.

(b) Distributed response in pontoon 1 in z-direction

The trend of response in z-direction in the pontoons is that response wrt. H_s and V_{mean} will be driven by both wind and waves. High H_s implies high response, and so does high V_{mean}. The decaying trend is strong for the z-direction, due to the aerodynamic damping in this degree of freedom. When looking at the magnitude of these responses, it is to be noted that the response are in 10^{-3}, implying very low displacement. This seems reasonable, consistent with the modeling assumptions with high tensioned tethers. One can assume that a larger mixture of modes have been excited for these responses of H_s and V_{mean} for the tether displacement in z-direction.
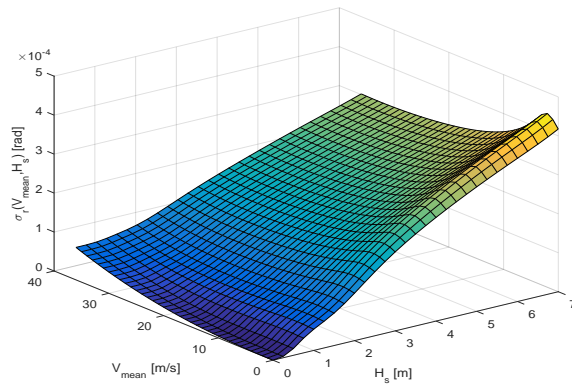

Figure 6.31: (c) Distributed response in pontoon 1 θ_x-direction

Response in θ_x- direction for the pontoon shows high response for high waves and lower response for higher wind velocities. The decaying trend is assumed to be due to the aerodynamic damping as addressed earlier. Torsional modes are distributed over the whole frequency spectra. The torsional response was governed by frequencies corresponding to the peak wave frequencies for the wave load spectrum from the plot of H_s=3.75 m. One can accordingly assume that the response in larger extent is governed by wind
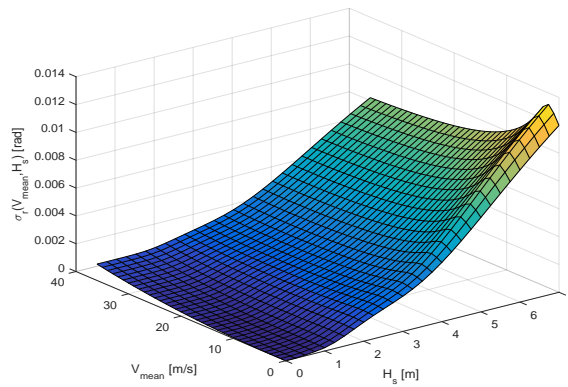
Figure 6.32: (d) Distributed response in pontoon 1 θ_z-direction

Response in θ_z-direction is significant for high waves and less significant for high mean wind velocities. The response is however much larger than for θ_x.

6.4.3 STD response along the girder

The standard deviation response is plotted for three different stationary environmental conditions. One of these is wind and wave corresponding to 100 year design load parameters of TDA, while the other is assuming conservative mean wind wind and conservative significant wave height. As standard deviation is a measure of average fluctuating response, and the plots are not direct representations of the response. Static response effects from mean wind has not been taken into account. The plots are for y, z- and θ_x direction. The three conditions will be described in the order of separate conservative mean wind wind, separate conservative wave height and the combined coupled condition.
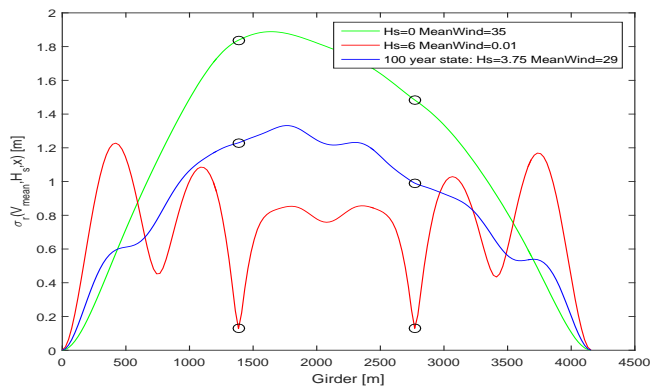

Figure 6.33: STD of response in y-direction along the girder

For y-direction in figure 6.33 the response seems directly related to mode 1. Strongly de-

caying wind spectrum from low to high frequencies supports this argument. The maximum response is to be found between tower 1 and the mid girder.

The condition with conservative wave, creates a very different behavior in the girder. As the spectral wave load spectrum in figure 5.3 gives peaks at higher frequencies than the first mode and is high in the interval of 0.5-1.2 rad/s, and has two peaks in 0.58 rad/s and 0.9 rad/s, it seems evident that the response shape of the girder is driven by wave resonance in modes between these frequencies.

For the coupled condition, the STD plot shows another combination of modes that resonate with wind and wave. The spectral distribution plot for both the mid-girder and quarter span node in figure 6.18 shows that response governed by mainly wind resonating with mode 1. Combinations of mode contributions from modes with higher frequencies could also be evident as there are mode amplitudes in y-direction for the girder for frequencies of where the wave spectral forces are high. These can be considered far less significant than the response contributions from wind.
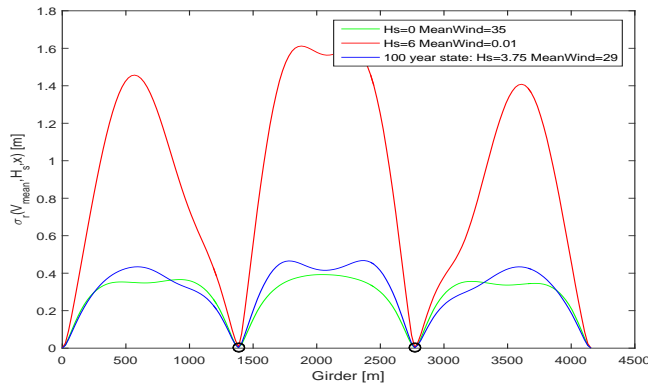

Figure 6.34: STD of response in z-direction along the girder

Standard deviation in z-direction gives low response in the girder at the towers. High wind does not imply high response in the girder. Recalling that frequencies causing high vertical response are at higher frequencies; e.g 0.558 and 0.91 rad/s for mode 8 and 16 were of significance. This might explain high STD response at the girders for high wave, as where the response is much lower for the conservative wind and coupled condition. Higher significant wave height causes a shift in the peaks, and it is possible that a higher resonance occurs due to this shift, causing a standard deviation three times higher than the other two conditions.

A low response for the conservative wind and the coupled conditions can accordingly be reasoned by two previously stated observations; that aerodynamic damping has a significant effect on the vertical response for higher wind velocities in the girder, and that response contributions to the vertical modes from wind are low.
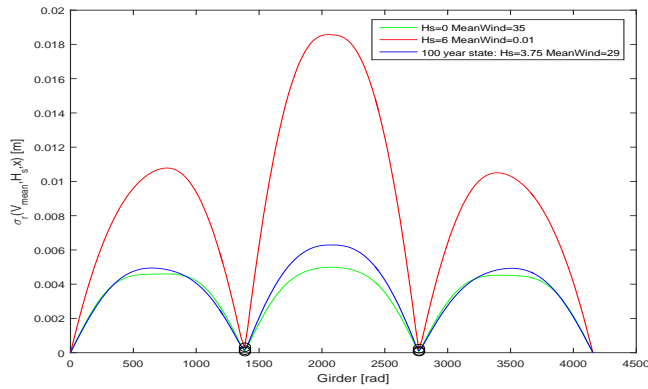
Figure 6.35: STD of response in θ_x-direction along the girder

The torsional standard deviation response plot follows the same tendencies as in figure for response in z-direction, where the case of high wave is much higher than for conservative wind and coupled conditions. Torsional modes are difficult to identify for a slender bridge structure. Spectral plots of response in mid-girder and in the node of the first span in figure 6.26 shows higher response contributions from higher frequencies.

High wind excites mode 1, where both the girder and the towers are translated in y-direction. Considering the response in the tower from conservative wave and from conservative wind, it is fair to assume that the motion of the girder drives the motion in the pontoons in y-direction. Moreover, it is to be noted that the difference in response from the two towers are due to the difference in lengths in the mooring lines.

6.4.4 Response due to different crest lengths for two environmental conditions in y-direction

STD plots for response in y-direction were made to display effects of a different crest length s. The plots in Figure 6.33 showed STD response in y-direction for s=5. New plots were made for response in y-direction for two of the above stationary conditions, $H_s = 6$ and $V_{mean} = 0$, and for the coupled condition with $H_s = 3.75$ and $V_{mean} = 29$, with effects of different crest lengths. s=1, s=10, s=1000 are investigated for in addition to s=5. s=1 represents accordingly a short crested wave while s=1000 can represent a crest length of which waves excite the two towers in phase.
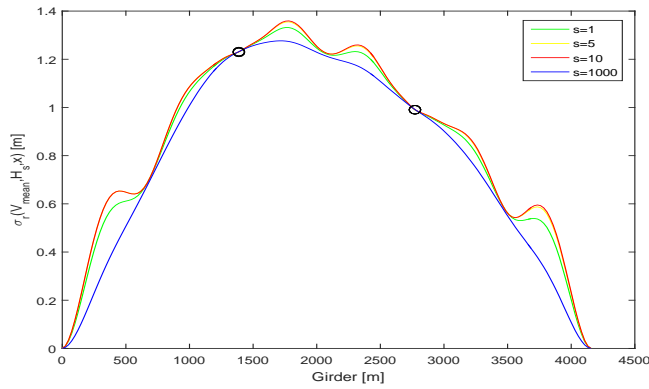
Figure 6.37: Parameters $Hs = 3.75m$, $V_{mean} = 29m/s$
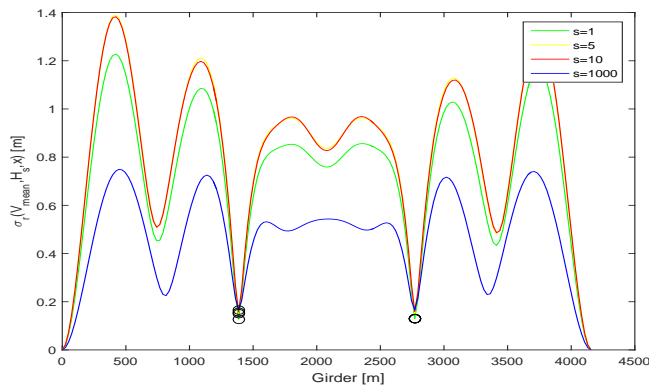
Figure 6.36: Parameters $Hs = 6m$, $V_{mean} = 0m/s$

Figure 6.36 displays higher response for lower crest lengths. The curve s=1000 has a flatter curve in the mid girder span, meaning that it might prohibit the anti-symmetric mode resonance with the loads. Crest length parameter set to s=1 gives however lower response than for the response of s=5 and s=10, where the latter two are close to equal along the girder.

For the coupled condition where the waves are set to be lower and wind velocity higher, it seems evident that a high crest length prohibits the anti-symmetric modes to participate in the response. As wind might dominate the response in y-direction for both the pontoons and the towers in coupled environmental conditions, the response effects of higher crest lengths will be relatively small but still significant for given points on the girder.

6.4.5 Response analysis discussion

A general trend from the response plots is that the wind governs the response in y-direction for the whole bridge, while the waves govern the response in z- θ_x and -direction. This is due to lateral modes in y-direction having low frequencies resonating with the wind spectrum which is high for lower frequencies. The frequencies governing high spectral densities of wave forces are between 0.5-1.2 rad/s. Several vertical modes are within this interval and waves govern therefore the response in z-direction. The response in the pontoons are minimal due to waves alone. It seems accordingly evident that motion in girder due to wind resonance with the first modes will excite the largest response in the towers.

The largest responses will be in y-direction, and the wind will accordingly govern the largest responses for the bridge structure. Seeing the distributed plots of response vs. H_s and mean wind, a general trend is that the aerodynamic damping will damp out the response for wind velocities below the higher velocities above 20 m/s. Long or short crost lengths have the effect of either prohibiting or enhancing the anti-symmetric modes and should be taken into account when designing similar bridges corresponding bridge for its environment.

6.5 Motion induced instabilities

The analysis described in section 5.3 resulted in the lowest mean wind velocity, V_{CR} that would generate motion induced instability for a specific mode, ω_{CR}. The analysis generated a plot for the real and imaginary part of the eigenvalues, i.e. 300 lines in each plot. The figure is shown in the appendix D.1. Recalling that the search for a motion induced instability would stop when the real part of the eigenvalue got larger than zero, $\mu > 0$, with increasing mean wind velocity. In figure 6.38 μ for the critical mode is presented.
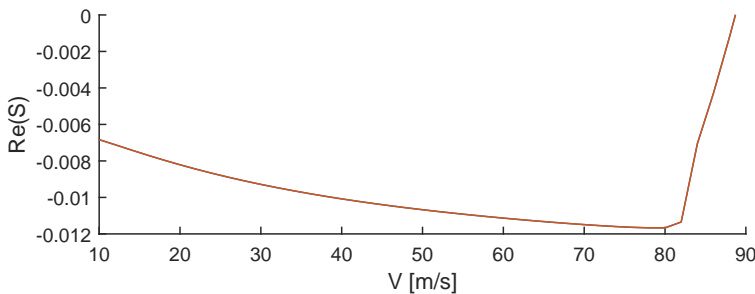

Figure 6.38: Extracted the development of the real part of the eigenvalue as function of mean wind velocity

The reason for the change is due to the mean wind dependent $K_{ae}(V, \omega)$ and $C_{ae}(V, \omega)$. At higher wind velocities it is the damping that is most effected. The critical mean wind velocity, frequency and mode is given in table (6.4)

Table 6.4: Conditions for motion induced instability

Critical condition	Value	Unit
$V_{mean}CR$	88.7188	[m/s]
ωCR	1.5217	[rad/sec]
ModeCR	40	[ ]

To verify the result the fully coupled ABAQUS model was set up to run for the first 40 modes, the initial guess for the frequency was sett to 1.5217 rad/s and the mean wind velocity was set to 88.7 m/s. The goal of the simulation was hopefully to obtain the real part of the eigenvalue equal to zero, and the critical damping ratio equal to zero. Determine how the instability mode behaves from ABAQUS Viewer, and investigate if it was flutter, galloping or a torsional instability was desired.

Unfortunately, the ABAQUS model crashed and a solution was not found within the time frame of the writing of the thesis. ABAQUS crashed at the static step of applying gravity load to the model. A possible explanation for the crash at the static step is that the aerodynamic stiffness weakens the structure in a numerical way and a to large deformations are obtained so ABAQUS cant find a solution. A solution strategy was to add the user- and wire elements for the aerodynamic damping and stiffness after the static steps of gravity loading and temperature geometry regaining, but the result was unsuccessfully. This is left for further work.

Chapter 7

Conclusion

A parametrized FE bridge model for a TLP-based multi-span suspension bridge was created from scratch and applied for the case of Bjørnafjorden. A response analysis was then developed to calculate the dynamic response and an instability analysis was conducted in an attempt of finding instability limit of critical mean wind velocity, frequency and corresponding mode.

An iterative procedures was carried out for the modal analysis accounting for the full coupling of frequency dependent environmental terms. User defined elements and wire elements were used to account for the coupled mass, damping and stiffness from the environmental contribution. Assumptions of buffeting theory and aerodynamic derivatives from the Hardanger bridge were used to obtain aerodynamic stiffness and damping. Linear wave potential theory was applied using WADAM/HydroD for the pontoons to obtain the hydrodynamic mass, damping, stiffness as well as the wave transfer functions. Wave transfer functions were subsequently used with the stochastic sea surface elevation function accounting for spatial correlation to obtain the wave exciting forces. Eigenvectors from a purely structural model were used to modalize and couple the terms from wind, waves and structure.

The iterative coupled modal analysis procedure in general lower frequencies, where e.g mode 1 was shifted from 0.1202 to 0.0782 rad/s. Plots from Figure 6.16 showed low impact from the aerodynamic motion induced terms, such that the shift in eigenfrequencies were due to the sole impact of hydrodynamic motion induced terms for $V_{mean} = 40m/s$. Modes for the coupled model in y-direction were mostly for lower frequencies 0.0782-0.5581 rad/s between mode 1 and mode 8. Modes higher than these were mostly torsional or vertical in the girder.

Response was investigated for in the first pontoon reference node, and on the girder for 25×29 combinations of H_s and V_{mean}. Response due to crest length was also investigated

for. Conclusions drawn from the response analysis was that wind governed the response for the whole bridge in y-direction due to load resonance with mode 1. For response in z,- torsional and θ_z direction along the girder, the waves were more governing. Impact of aerodynamic damping was evident for the standard deviational plots, and so was the effect of crest length, prohibiting the anti-symmetric modes to participate in the response.

A motion induced instability analysis was carried out using coupled system matrices from wind and waves in modal coordinates. Structural eigenvectors were assumed sufficient for this analysis and critical mean wind of 88 m/s and a critical frequency of 1.5217 rad/s for mode 40 was found. Seen in comparison with the estimated hundred year return period stationary mean wind of 29 m/s, 88 m/s is extremely high of which the bridge will not be subjected to.

7.1   Further work

Further work that should be conducted in the extent of this master thesis is suggested below.

1. Use the intended girder for the Bjørnafjorden bridge and corresponding aerodynamic derivatives to perform a modal and response analysis.

2. Modalizing and coupling the environmental and structural terms, using complex eigenvectors from a fully coupled modal analysis instead of the non-complex structural eigenvectors.

3. Find the corresponding mode shape for the critical mode at the instability limit, by further adjusting and improving the parametrized ABAQUS model.

4. Investigate and account for vortex induced vibrations in a dynamic response analysis of a structure

5. Develop a generalized procedure for restoring of the deformed bridge shape in ABAQUS after gravity has been put on the model to obtain the initial shape

Bibliography

[1] DNV, October 2010. Environmental conditions and environmental loads. Standard, Det Norske Veritas.

[2] Faltinsen, O. M., 1998. Sea Loads on Ships and Offshore Structures. Cambridge University Press.

[3] Gao, Z., 2016. Hydrodynamic analysis of offshore wind turbines. Lecture note, NTNU.

[4] Knut Andreas Kvåle, R. S. O. , January 2016. Modelling the stochastic dynamic behaviour of a pontoon bridge: A case study. Tech. rep., NTNU.

[5] Lee, C. H., 10 1995. Wamit theory manual.

[6] Sigbjörnsson, R., January 1979. Stochastic theory of wave loading process. Tech. rep., NTH/NTNU.

[7] Strømmen, E., 2005. Theory of Bridge Aerodynamics. Springer.

[8] Strømmen, E., 2014. Structural Dynamics. Springer.

[9] Strømmen, E., 2015. Multi-span suspension bridge on floating foundations.

[10] TDA, June 2015. Analysis report. Tech. Rep. REP-2602-003, response analysis due to environment.

[11] TDA, June 2015. Analysis report. Tech. Rep. REP-2602-003, modal Analysis.

[12] Y.J Ge, H. T., August 1999. Aerodynamic flutter analysis of cable-supported bridges by multi-mode and full-mode approaches. Tech. rep., motion induced instabilities.

[13] Øiseth. Ole, Rönquist. A, S. R., March 2010. Simplified prediction of wind-induced response and stability limit of slender long-span suspension bridges, based on modified quasi-steady theory: A case study. Tech. rep.

Appendix A

Supplementary Theory

A.1 Stochastic processes

Observed outcomes of a physical process that occur randomly can be represented as stochastic processes, meaning that it is possible to determine the numerical outcome with a certain probability. Inversely, stochastic processes can be evolved over time following predefined statistical distributions and statistical parameters. Examples of these physical processes are wind and wave fields modeled as stochastic and homogeneous processes. Homogeneous, as the stochastic process accounts for units in a defined field. Common practice is to distinguish between short term and long term processes [7]; where environmental parameters are stationary for given short time intervals; following predefined statistical behavior based on measurements. Long-term processes are often defined by a statistical representation of a larger amount of short term processes. The short termmeasurements are often represented in frequency domain as (cross) spectral dencities.

A.2 Spectral density functions

The correlation of two stochastic processes is how a statistical parameter in one spatial position of a stochastic process correlates with a statistical parameter in another spatial position. The Cross power spectral density (CPSD) gives the power of the correlation of two signals, $x(t)$ and $y(t)$, distribution over the frequency band. The cross correlation function between two signals, x and y, is defined as the expected value of the product of the signals with a time delay, τ [7]:

$$R_{xy}(\tau) = E\left[x(t)y(t+\tau)\right] \tag{A.1}$$

Using the cross-correlation theorem and the convolution relation [7], the cross-spectral density of the cross correlation function in A.1,

$$S_{xy}(\omega) = \int_{-\infty}^{\infty} R_{xy}(\tau)e^{-i\omega t}dt \tag{A.2}$$

If $x = y$, such that $R_{xx} = E[x(t)x(t+\tau)]$, the auto-spectral density function for x, S_{xx}, is obtained. The auto spectral density function defines the energy content of one independent frequency dependent process, while the cross-spectral density function defines the frequency domain process accounting for correlation of two variables; i.e a mathematical special case of A.2. If a spectral process in frequency domain already is obtained, the cross- and auto-spectral density can be denoted as follows for given spectral processes

$$S_{xy}(\omega) = \lim_{T\to\infty} \frac{1}{\pi T}[a_x(\omega)a_y(\omega)^H] \tag{A.3}$$

The spectral processes $a_x(\omega)$ and $a_y(\omega)$ are obtained by taking the Fourier transform of respectively the time-dependent x and y. Similarly to the formulation in equation A.2, the auto-spectral density can be obtained when $x = y$.

A.3   Response in frequency domain

Auto spectral density can be obtained for the response by inserting equation (2.11) into equation with equation (A.3), where a_r is the spectral process for response. The response in frequency domain can be obtained as below [7]

$$S_{rr} = \lim_{T\to\infty} \frac{1}{\pi T}\left[H(\omega)a_R(\omega) \cdot (a_R(\omega)H(\omega))^H\right] \tag{A.4}$$

The standard deviation (STD) in addition to the mean deformations gives the total linear response. The mean displacement is due to loading such as mean wind velocity. Obtaining the mean displacement is considered trivial. The variance of the spectral response is obtained by integration over the frequencies from zero to infinity as follows

$$\sigma_r^2 = \int_0^{\infty} S_{rr}d\omega \tag{A.5}$$

By taking the square root of the variance, i.e σ on obtains the STD. The STD is the statistical property of average deviation from the mean displacement. Together with an obtained mean response one can use the standard deviation to calculate linear response in physical units.

Appendix B

Modeling Details

B.1 Properties of the components of the bridge

Table B.1: Properties of the components of the bridge model

	Element	Area	Ixx	Ixy	Iyy	J	E	v	G	Temp.coeff.	Alpha	Beta	Density	Shear,yy	Shear,zz
Main Cable	B31	0.333	6.00E-05	0	6.00E-05	1.20E-04	2.00E+11	3.00E-01	7.69E+10	1.00E-05	0.0008	0.0307	8676		
Side Cable	B31	0.333	6.00E-05	0	6.00E-05	1.20E-04	2.00E+11	3.00E-01	7.69E+10	1.00E-05	0.0008	0.0307	8676		
Hangers	B31	0.032	9.00E-09	0	9.00E-09	1.80E-08	2.00E+11	3.00E-01	7.69E+10	1.00E-05	0.0008	0.0307	8351		
Girder	B32	0.5678	0.972	0	15.326	2.46	2.10E+11	3.00E-01	8.08E+10	1.00E-05	0.0008	0.0307	0.00E+00		
Tower fixed															
min	B31	5.006	14.893	0.01	14.89	22.2264	4.00E+10	3.00E-01	1.20E+10	1.00E-05	0.0008	0.0307	2.50E+03	6.48E+10	6.48E+10
max	B31	17.181	172.655	0.01	124.66	224.89674	4.00E+10	3.00E-01	1.20E+10	1.00E-05	0.0008	0.0307	2.50E+03	1.23E+11	1.01E+11
Cross beams on fixed tower															
top	B31	10.526	23.219	0.01	46.2	48.724769	4.00E+10	3.00E-01	1.20E+10	1.00E-05	0.0008	0.0307	2.50E+03	5.76E+10	8.64E+10
middel	B31	14.48	47.83	0.01	130.83	112.84464	4.00E+10	3.00E-01	1.20E+10	1.00E-05	0.0008	0.0307	2.50E+03	6.76E+10	1.24E+11
bottom	B31	15.217	90.329	0.01	116.78	160.79653	4.00E+10	3.00E-01	1.20E+10	1.00E-05	0.0008	0.0307	2.50E+03	9.23E+10	1.08E+11
Tower floating								3.00E-01							
min	B31	5.006	14.893	0.01	14.89	22.2264	4.00E+10	3.00E-01	1.20E+10	1.00E-05	0.0008	0.0307	2.50E+03	6.48E+10	6.48E+10
max	B31	17.181	172.655	0.01	124.66	224.89674	4.00E+10	3.00E-01	1.20E+10	1.00E-05	0.0008	0.0307	2.50E+03	1.23E+11	1.01E+11
Cross beams on towers floating															
top	B31	10.526	23.219	0.01	46.2	48.724769	4.00E+10	3.00E-01	1.20E+10	1.00E-05	0.0008	0.0307	2.50E+03	5.76E+10	8.64E+10
middel	B31	14.48	47.83	0.01	130.83	112.84464	4.00E+10	3.00E-01	1.20E+10	1.00E-05	0.0008	0.0307	2.50E+03	6.76E+10	1.24E+11
bottom	B31	15.217	90.329	0.01	116.78	160.79653	4.00E+10	3.00E-01	1.20E+10	1.00E-05	0.0008	0.0307	2.50E+03	9.23E+10	1.08E+11
Top beam on towers floating	B31	14.48	47.83	0.01	130.83	112.84464	4.00E+10	3.00E-01	1.20E+10	1.00E-05	0.0008	0.0307	2.50E+03	6.76E+10	1.24E+11
Diagonal beams on towers floating	B31	14.48	47.83	0.01	130.83	112.84464	4.00E+10	3.00E-01	1.20E+10	1.00E-05	0.0008	0.0307	2.50E+03	6.76E+10	1.24E+11
Pontune legs	B31	16.447	106.147	0.01	78.16	136.81643	4.00E+10	3.00E-01	1.20E+10	1.00E-05	0.0008	0.0307	2.50E+03	9.82E+10	8.76E+10
Pontune crosser beams	B31	14.48	47.83	0.01	130.83	112.84464	4.00E+10	3.00E-01	1.20E+10	1.00E-05	0.0008	0.0307	2.50E+03	6.76E+10	1.24E+11
Pontune to pylon connection	B31	16.447	106.147	0.01	78.16	136.81643	4.00E+10	3.00E-01	1.20E+10	1.00E-05	0.0008	0.0307	2.50E+03	9.82E+10	8.76E+10
Tensionlegs	B31	0.3717	9.00E-09	0	9.00E-09	1.86E-08	2.10E+11	3.00E-01	8.08E+10	1.00E-05	0.0008	0.0307	1.00E+03		

Appendix C

Analysis Details
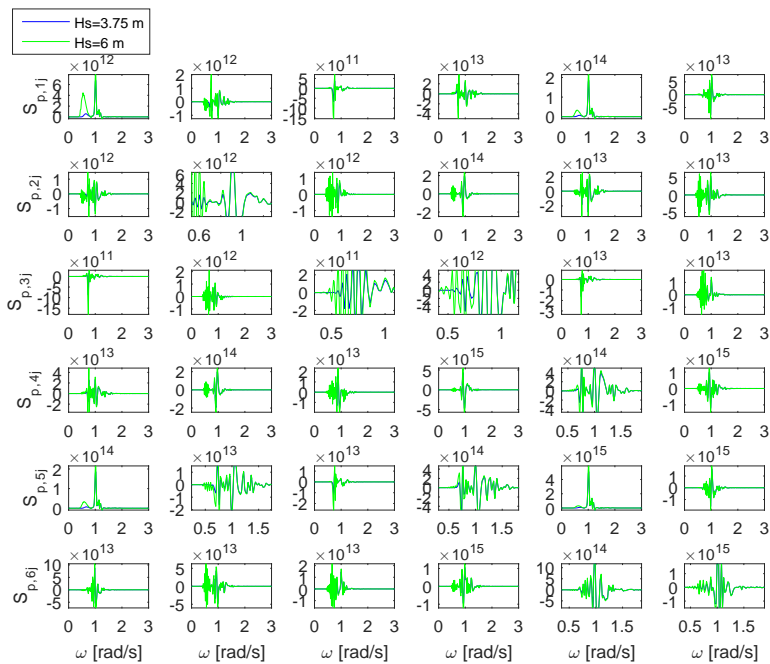
C.1 Load spectrum

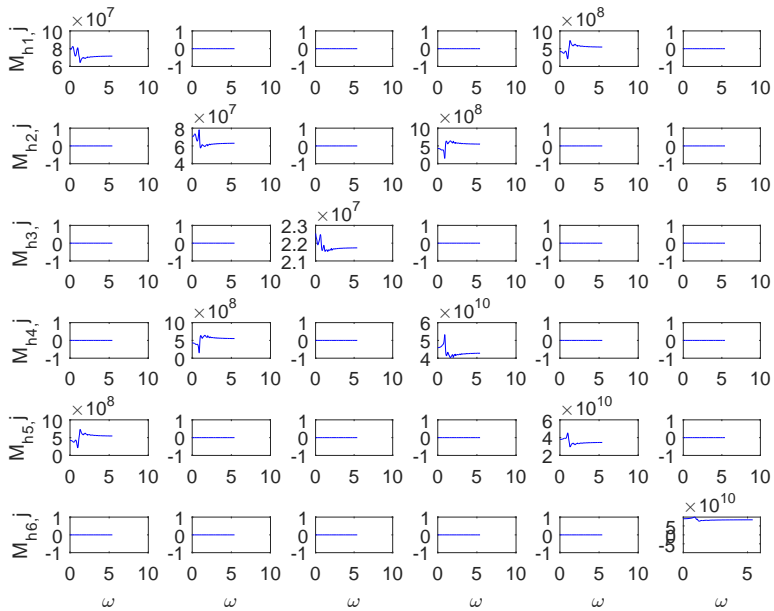Figure C.1: Cross-spectral density functions between tower 1 and tower 2
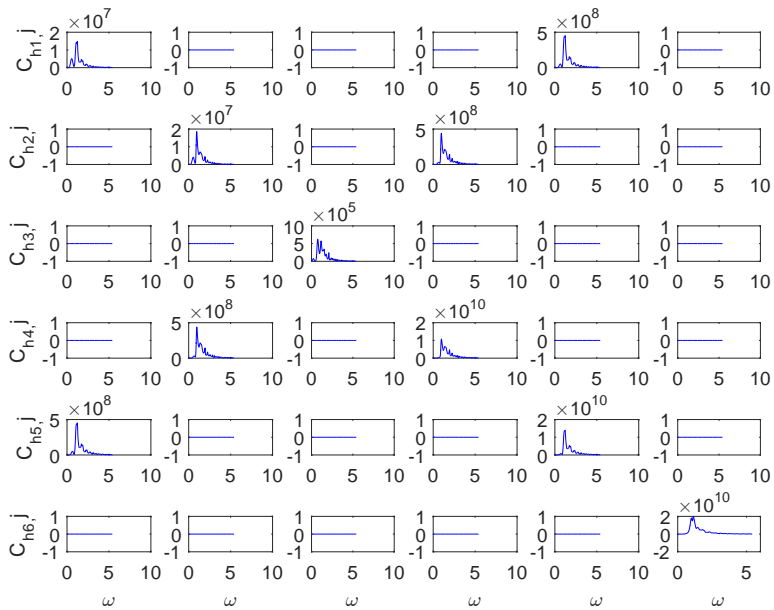
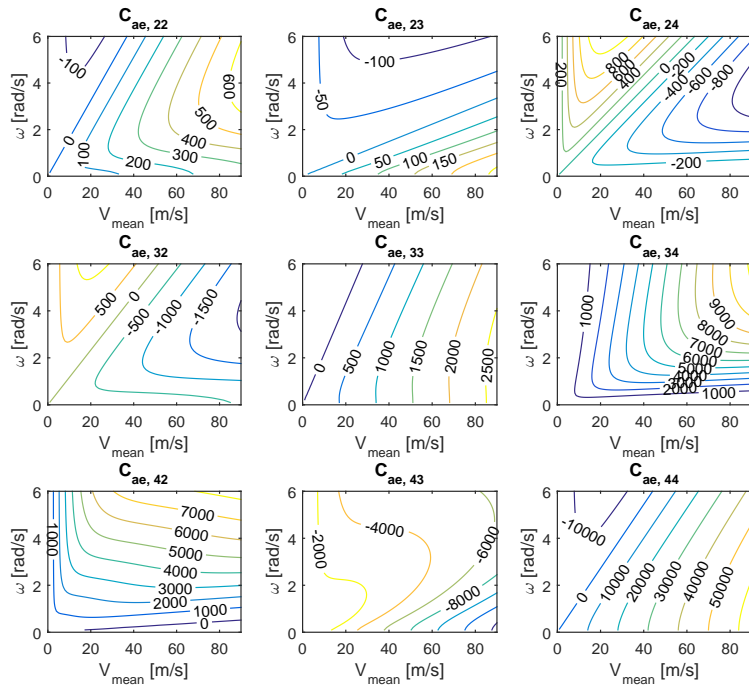Figure C.2: Hydrodynamic added mass

Figure C.3: Hydrodynamic damping

Figure C.4: Aerodynamic damping as function of frequency and mean wind velocity for y,x and θ_x direction
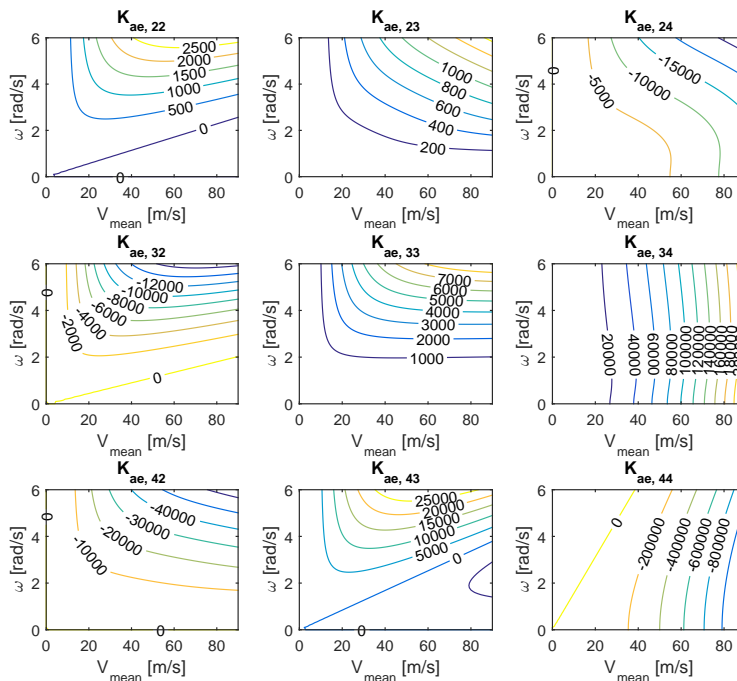
Figure C.5: Aerodynamic stiffness as function of frequency and mean wind velocity for y,x and θ_x direction

TDA: Extreme response from 100 year return period load

Wind		
	1h mean wind speed	29 m/s
	Direction	west
Wind-generated sea		
	Hs	3.75 m
	Tp	6s
	Direction	West-northwest
	Tide	- 1.3 m
	Current speed	0 m/s
Swell		
	Hs	0.39 m
	Tp	13 s

Table C.1: Environmental conditions giving extreme responses for 100 year return period environmental load from TDA [10]

Appendix D
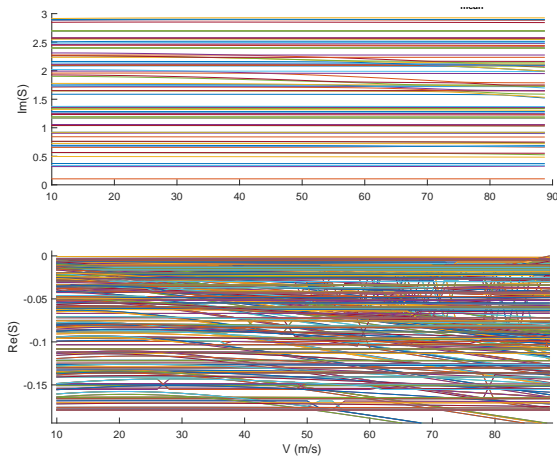
Additional Results

D.1 Motion induced instability

Figure D.1: Real and imaginary of eigenvalues as function of mean wind velocity
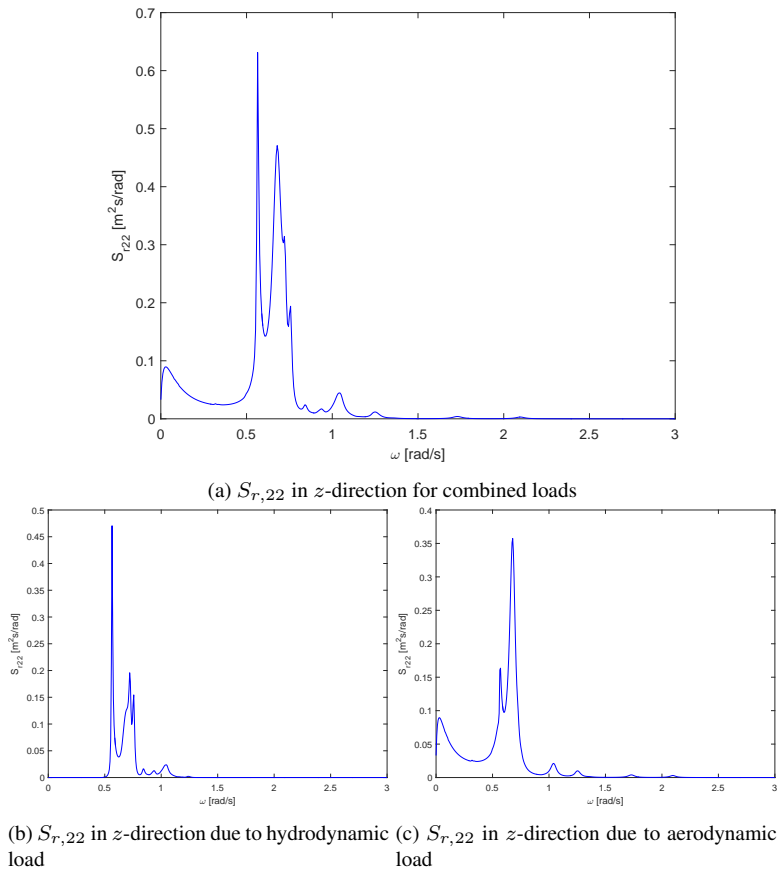
D.2 Spectral response in q1, z-direction

(a) $S_{r,22}$ in z-direction for combined loads

(b) $S_{r,22}$ in z-direction due to hydrodynamic load

(c) $S_{r,22}$ in z-direction due to aerodynamic load

Figure D.2: z-direction in q1: Coupled response vs. response contributions from hydrodynamic and aerodynamic loads

D.3 Spectral response in q2, z-direction

(a) $S_{r,22}$ in z-direction for combined loads

(b) $S_{r,22}$ in z-direction due to hydrodynamic load

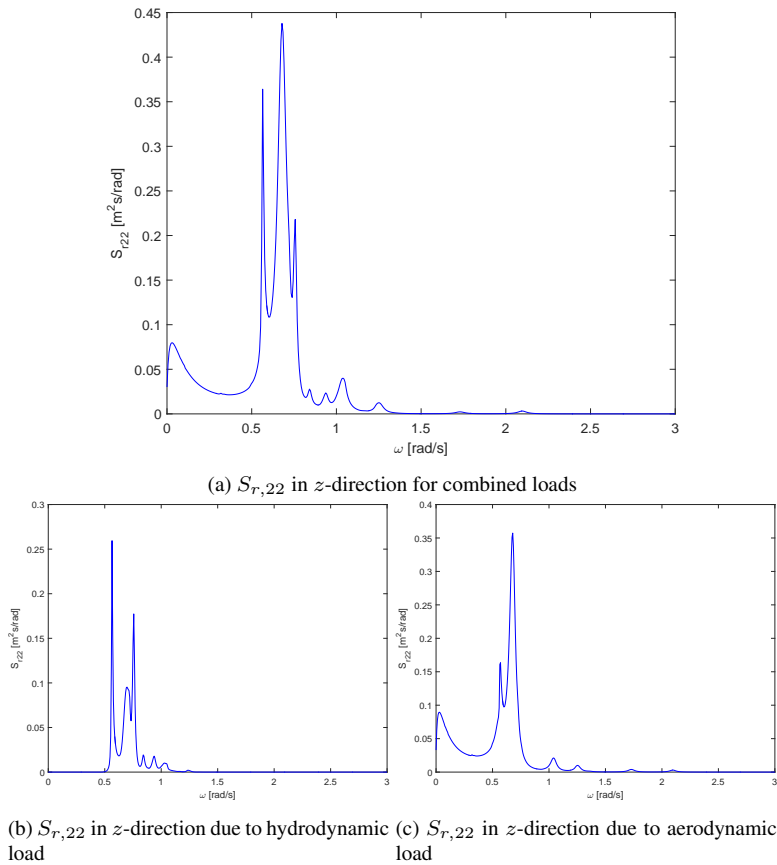(c) $S_{r,22}$ in z-direction due to aerodynamic load

Figure D.3: z-direction in q2: Coupled response vs. response contributions from hydrodynamic and aerodynamic loads